THEORETICAL STUDIES

OF NONUNIFORM ORIENTATIONAL ORDER

IN LIQUID CRYSTALS AND ACTIVE PARTICLES

A dissertation submitted to

Kent State University in partial

fulfillment of the requirements for the

degree of Doctor of Philosophy

by

Ayhan Duzgun

May 2018

Dissertation written by

Ayhan Duzgun

B.S., Middle East Technical University, 2003

M.S., University of Pittsburgh, 2005

Ph.D., Kent State University, 2018

Approved by

_____, Chair, Doctoral Dissertation Committee
Dr. Jonathan Selinger

_____, Co-Chair, Doctoral Dissertation Committee
Dr. John Portman

_____, Members, Doctoral Dissertation Committee
Dr. Hamza Balci

_____
Dr. Benjamin Fregoso

_____
Dr. Robin Selinger

_____
Dr. Antal Jakli

Accepted by

_____, Chair, Department of Physics
Dr. James T. Gleeson

_____, Dean, College of Arts and Sciences
Dr. James L. Blank

TABLE OF CONTENTS

x

ACKNOWLEDGMENTS

My experience at Kent State will be one to always remember and proudly mention. I have enjoyed the privilege of being at Kent State with wonderful people who make Kent State an excellent place.

First, I would like to thank my advisor Prof. Jonathan Selinger for his extraordinary guidance throughout my PhD studies. He has struck me as an advisor who always cares for his students' best possible experience as a graduate student and best outcome regarding life after graduation. I feel very lucky to have had him as my advisor as he always provided support, helped me gradually grow, and treated me (and other students) with respect. He has given me the option (sometimes requested) to participate in conferences and other programs which significantly helped with my education and network building.

I would also like to thank Prof. John Portman for serving as my co-advisor and for his guidance and discussions all these years.

Part of the research in this dissertation was done at Los Alamos National Lab while I was invited to CNLS by Dr. Avadh Saxena. Dr. Saxena is an exemplary scientist and has been a source of motivation for me. I am thankful for his support and important contributions.

I also would like to thank Prof. Robin Selinger. I have gained valuable computational skills by taking her class and by engaging in group discussions. She has been very supportive and has had important influence on my perspective as a physicist. I would like

to thank other members of our group as the experience and culture that formed over the years wouldn't be possible without them. To mention a few names that I interacted directly; Shamid, Son, Andrew, Vianney, Sajedeh, Mike, Xingzhou, Youssef, and Dong..

I would like to thank all of the faculty members of the Physics Department and Liquid Crystal Institute for their valuable contributions, especially Prof. Hamza Balci who served as my academic advisor and later continued to give me valuable advice when I needed. Here, I should also mention that the very warm first encounter with Prof. Declane Keane, the graduate director at the time, made me feel that Kent State was a great choice for doing PhD in physics. I thank Prof. Keane and also Prof. Khandker Quader for their continued encouragement and interest in my endeavors.

I am thankful to the administrative staff of Physics and LCI including Loretta Hauser, Cynthia Miller, Reho Constance, Kelly Conley, Mary Ann Kopcak, and Mary Lin Bergstrom. Special thanks to Jeffery McCann and Jim Francl for taking extra time to help me with financial and technical matters. I also thank other people whose names I may have forgotten to include here.

Last but perhaps most importantly, I would like to thank my wife Ayse, because not only she came to Kent with me but also she heroically took care of our daughter during her illness and helped me have peace of mind and focus on my studies. Partly due to her tremendous support I am able get to this point where I am finishing my dissertation.

To my family and my teachers,

for their support and guidance..

CHAPTER 1

Introduction

1.1   Introduction

This dissertation combines three projects with the unifying theme of orientational order and how it is controlled by means of internal and external factors.

Positional order may not always be present in soft materials but there are many situations where orientational order is an important component in the picture.

Liquid crystal systems are such examples in which generally elongated molecules form orientationally ordered phases when cooled below a critical temperature [1, 2]. This is due to the molecular interactions which favor *nematic* alignment of the molecules. Liquid crystals also respond to external electric and magnetic fields by aligning with the fields. Depending on the dielectric properties of the material, molecules can be aligned parallel or perpendicular to the field. Electro-optical properties of liquid crystals depend sensitively on molecular orientations thus by controlling the alignment, physical properties can be changed dramatically. Due to these adjustable properties liquid crystal have found place in important technological applications especially in but not limited to the display industry.

Active matter systems have also been of great interest since the 1995 Vicsek article [3] which presented a simplified model of animal flocks and shows a phase transition from disordered to ordered phases. Since then, great theoretical and experimental progress has been made and active matter research has emerged as an interdisciplinary area at the

intersection of many branches of science [4]. It also has found applications in engineering, and has even influenced fields like economics (network models) [5].

Orientational order in the above systems can be uniform all over the volume of the material due to molecular alignment but also other factors may avoid single domains or favor polydomain or modulated phases. The focus of this dissertation is to describe and quantify the nonuniform order and identify what roles the involved factors play.

In this chapter I will first introduce orientational order and how to describe it by using vector and tensor order parameters. Next I will explain the topics of each of the three projects which I briefly mention below.

In the first project (Chapter 2), I investigate polydomain formation during the manufacturing of liquid crystal elastomers. Liquid crystal elastomers (LCE) are materials where the orientation of molecules is coupled to an elastic polymer network. While regular liquid crystals can easily form nematic monodomains, liquid crystal elastomers usually have polydomains, with a different average direction in each domain, unless prepared in special ways. The coupling between strain and order and added impurities are shown to be the factors determining the features of the domains.

The second project (Chapter 3), is concerned with active matter. An active ideal gas of point particles is studied and orientational order and density distribution is calculated near flat or curved walls. Even when the particles do not interact, the confining walls can still induce (nonuniform) order. We show how behavior near walls can be used to achieve actuation and rectification.

The third project (Chapters 4 and 5) investigates skyrmions which have very interesting director configurations. A skyrmion is a type of topological soliton. Skyrmions in
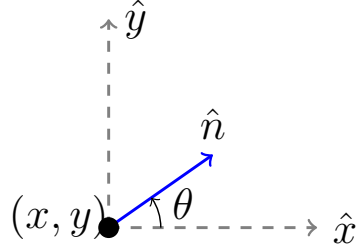
Figure 1: A particle with orientation

liquid crystals are formed by the interplay of chiral molecular interactions favoring a twist, external fields favoring easy-plane or easy-axis alignment, and surface anchoring providing preferred directions at the surface of a liquid crystal cell.

1.2 Orientational Order

For a system of particles, the probability distribution can be defined as a function of different variables. In the context of orientational order, the particles of interest have orientations defined along their bodies such as spin of an electron or the *head* of a bacterium along which it moves. In a 2D system, there are two spatial and one orientational degrees of freedom (see Fig. 1). Then the probability distribution can be defined as

$$P = P(x, y, \theta)$$

where P is the probability of finding the particle at $\vec{r} = (x, y)$ with the orientation angle θ which is conventionally measured from the positive x axis. The sum of all probabilities add up to 1, that is $\int_r \int_\theta P dr \, d\theta = 1$. We can also integrate over all possible angles to get the number of particles at a location. This integral is nothing but the number density of the particles $\rho(x, y) = \int P(x, y, \theta) \, d\theta$.

1.2.1   Vector order parameter

In order to quantify order in a system we can calculate average probability of aligning along a given axis. For instance if we want to calculate the average component of the unit vector along the x and y axes we calculate

$$\Pi_x = \langle \cos\theta \rangle = \frac{1}{\rho(x,y)} \int_0^{2\pi} P(x,y,\theta) \cos\theta \, d\theta$$

$$\Pi_y = \langle \sin\theta \rangle = \frac{1}{\rho(x,y)} \int_0^{2\pi} P(x,y,\theta) \sin\theta \, d\theta$$

Here $\vec{\Pi} = (\Pi_x, \Pi_y)$ can be defined as the polar order parameter because it is a measure of the local polarization of the system of particles. The magnitude $|\vec{\Pi}|$ is a measure of how ordered the system is, and it varies from 0 to 1.

Some types of particles have more than one special direction. For instance an elliptical particle (in 2D) has a long axis and a short axis and if we rotate the particle by 180° we get an identical state. Elongated granular particles such as rice and many types of liquid crytal molecules are just two examples from the real world. Polarization cannot be defined for these particles. In order words, the polar order parameter is not sufficient to describe the order in these systems. We need to describe a different type of order paramter for such systems. That is *nematic* order where particles have two-fold symmetry.

Figure 2 shows systems with different types of order. In part (b) a system with polar order is shown. This system has both polar and nematic order. However, in part (c), there is no polar order but only nematic order. Looking at only the polar order parameter, one might mistakenly think that the system is isotropic, however nematic order is clearly different from disorder(isotropic phase) as seen in the comparison of (a) and (c).

(a) Isotropic   (b) Polar Order   (c) Nematic Order
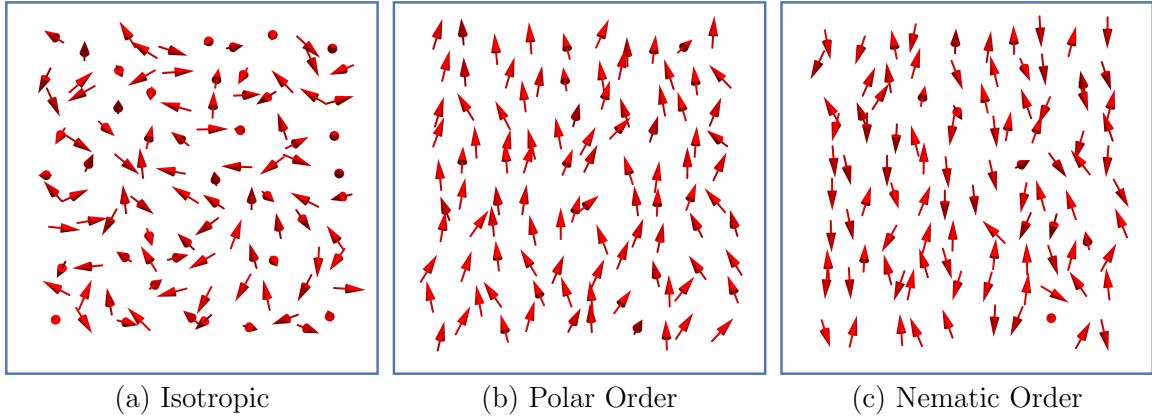
Figure 2: Isotropic, polar, and nematic phases

$\langle \cos(\theta) \rangle = 1$
$\langle \cos(2\theta) \rangle = 1$
$\langle \cos(3\theta) \rangle = 1$

$\langle \cos(\theta) \rangle = 0$
$\langle \cos(2\theta) \rangle = 1$
$\langle \cos(3\theta) \rangle = 0$

$\langle \cos(\theta) \rangle = 0$
$\langle \cos(2\theta) \rangle = 0$
$\langle \cos(3\theta) \rangle = 1$
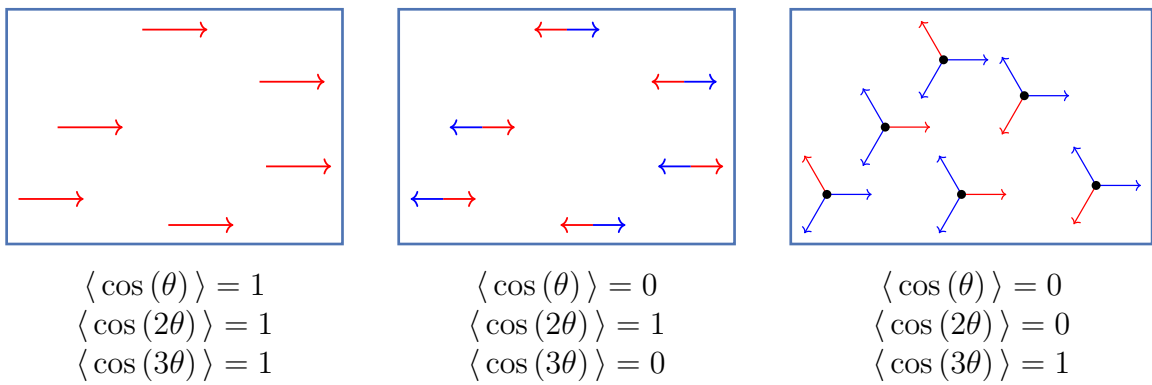
Figure 3: A particle with different symmetries

5

How could nematic order be calculated for particles with *up-down* or *left-right* symmetry? Instead of $\langle n_x \rangle = \langle \cos \theta \rangle$ we can calculate $\langle n_x^2 \rangle = \langle \cos^2 \theta \rangle$ or alternatively $\langle \cos 2\theta \rangle = \langle 2\cos^2 \theta - 1 \rangle$ where the two fold symmetry is clearer. To quantify the average alignment along $+x$ <u>or</u> $-x$ axes we can calculate

$$\langle \cos 2\theta \rangle = \frac{1}{\rho(x, y)} \int_0^{2\pi} P(x, y, \theta) \, \cos(2\theta) \, d\theta$$

Figure 3 shows the appropriate measures of order for different types of symmetries in a 2D system; higher moments of the probability distribution function can be used to describe the order in the system with higher symmetry. In general $e^{im\theta}$ can be used for m-fold symmetry. As a special case when one of the axes is along the x axis, just like the above example, $\langle \cos m\theta \rangle$ will give the average alignment along any of the $2\pi/m$ axes, that is the axes oriented at $0, \frac{2\pi}{m}, 2\frac{2\pi}{m}, 3\frac{2\pi}{m}, .., (m-1)\frac{2\pi}{m}$ radians from the x axis.

1.2.2 Tensor order parameter

Averaging $\cos(m\theta)$ gives a measure of the order when the average alignment is about the x axis ($\theta = 0$). However when the special axis has some arbitrary direction, we need to calculate other moments of the probability distribution function too. For example, in the case of polar particles, we need to calculate two components of the vector order parameter in order to describe the magnitude and direction of the polarization. Similarly, for higher symmetries, we need to calculate other components of the corresponding order parameters too. However for systems with symmetry higher than *one-fold* we cannot use vectors. We need to use tensors, a generalized form of vectors. Mathematical properties of tensors allow them to be very usefully employed to carry the information necessary in order to describe the orientational order.

Consider a 2D system of particles with nematic particles. Assume the average axis of alignment is at some angle θ_0 from the x axis. If we calculate $\langle \cos 2(\theta - \theta_0) \rangle$ we get a scalar that shows how well ordered the particles are. Also we know that $\langle \sin 2(\theta - \theta_0) \rangle = 0$. However we do not know what this special angle would be for any given system. We can perform the following calculations in order to find out this information. With the substitution $\theta' = \theta - \theta_0$

$$\langle \cos(2\theta) \rangle = \langle \cos(2\theta' + 2\theta_0) \rangle$$

$$= \langle \cos(2\theta') \rangle \cos(2\theta_0) - \langle \sin(2\theta') \rangle \sin(2\theta_0)$$

$$= \langle \cos(2\theta') \rangle \cos(2\theta_0)$$

Similarly

$$\langle \sin(2\theta) \rangle = \langle \sin(2\theta' + 2\theta_0) \rangle$$

$$= \langle \sin(2\theta') \rangle \cos(2\theta_0) + \langle \cos(2\theta') \rangle \sin(2\theta_0)$$

$$= \langle \cos(2\theta') \rangle \sin(2\theta_0)$$

which enables us to calculate the order and the special angle from

$$\langle \cos(2\theta') \rangle^2 = \langle \cos(2\theta) \rangle^2 + \langle \sin(2\theta) \rangle^2$$

$$\tan(2\theta_0) = \frac{\langle \sin(2\theta) \rangle}{\langle \cos(2\theta) \rangle}.$$

We can represent the above information also in tensor form as below.

$$\overleftrightarrow{Q} = \begin{pmatrix} \langle\cos(2\theta)\rangle & \langle\sin(2\theta)\rangle \\ \langle\sin(2\theta)\rangle & -\langle\cos(2\theta)\rangle \end{pmatrix}$$

$$= \langle\cos(2\theta')\rangle \begin{pmatrix} \langle\cos(2\theta_0)\rangle & \langle\sin(2\theta_0)\rangle \\ \langle\sin(2\theta_0)\rangle & -\langle\cos(2\theta_0)\rangle \end{pmatrix}$$

$$= S \begin{pmatrix} \langle\cos(2\theta_0)\rangle & \langle\sin(2\theta_0)\rangle \\ \langle\sin(2\theta_0)\rangle & -\langle\cos(2\theta_0)\rangle \end{pmatrix}$$

Where S is the scalar nematic order parameter independent from the coordinate system, while the rest of the tensor carries the information about the direction of the order. S can take values from 0 to 1, corresponding to complete disorder and perfect order, respectively.

Consider the case when the system has perfect order along x axis. Then $S = 1$, $\theta_0 = 0$, and $\overleftrightarrow{Q} = \begin{pmatrix} 1 & 0 \\ 0 & -1 \end{pmatrix}$. $Q_{11} = 1$ indicates that all the particles are aligned along the x axis and $Q_{22} = -1$ indicates that they are perfectly aligned perpendicular to y axis. We can understand it from the calculation of $\langle\cos(2\theta)\rangle$ around the y axis, in other words $\langle\cos(2[\pi/2 - \theta])\rangle = \langle\cos(\pi - 2\theta])\rangle = -\langle\cos(2\theta)\rangle$. Similarly, perfect alignment around y would give $\overleftrightarrow{Q} = \begin{pmatrix} -1 & 0 \\ 0 & 1 \end{pmatrix}$.

The above tensor is an expression used to describe the nematic order by a 2×2 tensor with basis vectors $\hat{x}$ and $\hat{y}$. The tensor $\hat{n} \otimes \hat{n}$ includes all the combinations of the products

of the basis vectors. We define

$$\overleftrightarrow{T} = \langle \hat{n} \otimes \hat{n} \rangle = \begin{pmatrix} \langle n_x n_x \rangle & \langle n_x n_y \rangle \\ \langle n_x n_y \rangle & \langle n_y n_y \rangle \end{pmatrix}$$

and compare it to the Q tensor described above which reads

$$\overleftrightarrow{Q} = \begin{pmatrix} \langle \cos(2\theta) \rangle & \langle \sin(2\theta) \rangle \\ \langle \sin(2\theta) \rangle & -\langle \cos(2\theta) \rangle \end{pmatrix} = \begin{pmatrix} \langle 2n_x n_x - 1 \rangle & \langle 2n_x n_y \rangle \\ \langle 2n_x n_y \rangle & \langle 2n_y n_y - 1 \rangle \end{pmatrix}.$$

Clearly $\overleftrightarrow{Q} = 2\left(\overleftrightarrow{T} - \frac{\overleftrightarrow{I}}{2}\right) = 2\left(\overleftrightarrow{T} - \overleftrightarrow{T}_{iso}\right)$ where $\overleftrightarrow{T}_{iso} = \begin{pmatrix} 1/2 & 0 \\ 0 & 1/2 \end{pmatrix} = \frac{\overleftrightarrow{I}}{2}$ is the value

of $\overleftrightarrow{T}$ for an isotropic system because in the isotropic case $\langle n_x^2 \rangle = \langle n_y^2 \rangle = \frac{1}{2}$, where $\overleftrightarrow{I}$ is

the identity matrix. Equivalently we can use the index notation $Q_{ij} = 2\langle n_i n_j \rangle - \delta_{ij}$, δ_{ij}

being the Kronecker delta.

So far we have shown the nematic Q-tensor representation of order in a system with

directors in 2D. The 3D representation can also be calculated in the same way with the

expression of the director in 3D vector components. The value of $\overleftrightarrow{T}$ in the isotropic

phase is $\overleftrightarrow{I}/3$ differently from the 2D value of $\overleftrightarrow{I}/2$. With the same procedure, we get

$Q_{ij} = \frac{3}{2}\left(\langle n_i n_j \rangle - \frac{\delta_{ij}}{3}\right)$. The factor of $\frac{3}{2}$ is included to make the value of the tensor

component equal to 1 when there is perfect order along a certain axis. For example, for

a perfect order along the x axis, $n = (1, 0, 0)$ and

$$\overleftrightarrow{Q} = \begin{pmatrix} 1 & 0 & 0 \\ 0 & -1/2 & 0 \\ 0 & 0 & -1/2 \end{pmatrix}$$

In order to benefit from the simplifications due to symmetry let's denote the director

in cartesian coordinates in terms of spherical variables

$$\hat{n} = \begin{pmatrix} n_x \\ n_y \\ n_z \end{pmatrix} = \begin{pmatrix} \sin\theta\cos\phi \\ \sin\theta\sin\phi \\ \cos\theta \end{pmatrix}.$$

Consider a system which is on the average aligned along the z axis but the alignement is not perfect. Let's calculate the Q tensor for this system

$$\overset{\leftrightarrow}{Q} = \frac{3}{2} \begin{pmatrix} \langle n_x^2 \rangle - \frac{1}{3} & \langle n_x n_y \rangle & \langle n_x n_z \rangle \\ \langle n_x n_y \rangle & \langle n_y^2 \rangle - \frac{1}{3} & \langle n_y n_z \rangle \\ \langle n_x n_z \rangle & \langle n_y n_z \rangle & \langle n_z^2 \rangle - \frac{1}{3} \end{pmatrix}.$$

The non-diagonal components of Q are zero. The diagonal components, after substituting $\langle n_z^2 \rangle = \langle \cos^2\theta \rangle$, $\langle n_x^2 \rangle = \langle \sin^2\theta\cos^2\phi \rangle = \frac{1}{2}\langle \sin^2\theta \rangle = \frac{1}{2} - \frac{1}{2}\langle \cos^2\theta \rangle$, $\langle n_x^2 \rangle = \langle n_y^2 \rangle$ follow $Q_{xx} = \frac{1}{2} - \frac{1}{2}\langle \cos^2\theta \rangle - \frac{1}{3} = \frac{1}{2}\left(\frac{1}{3} - \langle \cos^2\theta \rangle\right) = Q_{yy}$, and $Q_{zz} = \langle \cos^2\theta \rangle - \frac{1}{3}$. Thus

$$\overset{\leftrightarrow}{Q} = \frac{3}{2} \begin{pmatrix} \frac{1}{2}\left(\frac{1}{3} - \langle \cos^2\theta \rangle\right) & 0 & 0 \\ 0 & \frac{1}{2}\left(\frac{1}{3} - \langle \cos^2\theta \rangle\right) & 0 \\ 0 & 0 & \langle \cos^2\theta \rangle - \frac{1}{3} \end{pmatrix}$$

$$= \langle \frac{3}{2}\cos^2\theta - \frac{1}{2} \rangle \begin{pmatrix} -\frac{1}{2} & 0 & 0 \\ 0 & -\frac{1}{2} & 0 \\ 0 & 0 & 1 \end{pmatrix}$$

$$= S \begin{pmatrix} -\frac{1}{2} & 0 & 0 \\ 0 & -\frac{1}{2} & 0 \\ 0 & 0 & 1 \end{pmatrix}$$
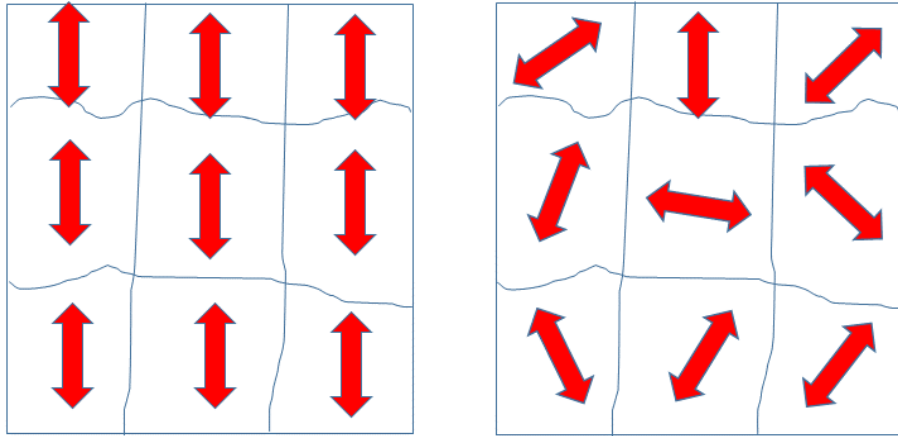
Figure 4: Monodomain and polydomain LCE's

Similarly to the 2D case, S can vary from 0 to 1. In general where the system is not aligned along any of the cartesian axes, we need to solve for the eigenvalues and eigenvectors of the 3×3 tensor. The eigenvector corresponding to the biggest eigenvalue will give the axis that the system is aligned with.

1.3 Nonuniform order in Systems Studied

1.3.1 Polydomain liquid crystal elastomers

The first system we studied is a 2D liquid crystal elastomer using continuum elasticity theory and finite element simulations.

Liquid-crystal elastomers are remarkable materials that combine the elastic properties of cross-linked polymer networks with the anisotropy of liquid crystals. Any distortion of the polymer network affects the nematic order of the liquid crystal, and, likewise, any change in the magnitude or direction of the nematic order influences the shape of the elastomer. When elastomers are prepared without any alignment, they develop disordered polydomain structures as they are cooled into the nematic phase. These polydomain structures are often attributed to quenched disorder in the cross-linked polymer network.

As an alternative explanation, we develop a theory for the dynamics of the isotropic-nematic transition in liquid crystal elastomers, and show that the dynamics can induce a polydomain structure with a characteristic length scale, through a mechanism analogous to the Cahn-Hilliard equation for phase separation. This polydomain state may eventually become uniform, or it may be locked in by quenched impurities.

In this theory, the local nematic order is coupled to the strain tensor, which satisfies the constraint of elastic compatibility. When an initially disordered system is cooled down to nematic phase a polydomain structure emerges and nematic order within each domain starts growing. This system with nonuniform orientational order has a characteristic domain size. The domain size and the growth rate of the nematic order depend on elastic constants, effective temperature and the strength of the coupling between nematic order and strain.

To determine the domain size we show that we can use the first minimum of the correlation function of the Q tensor

$$C(|r - r'|) = \langle \cos 2\left[\theta(r) - \theta(r')\right]\rangle. \tag{1}$$

During the cross linking process the elastic energy in the system favors a uniform order with a monodomain nematic order, however the interplay between elastic coupling and dynamics prevent rapid coarsening of the domains and generates nonuniform structures. This mechanism allows time for cross-links to freeze-in the polydomain structure. Alternatively polydomains can also be locked due to impurities in the system.

1.3.2 Active Ideal Gas

The second system that we study which exibits nonuniform orientational order is an ideal gas of active particles. The system consists of noninteractiong or very dilute self propelled particles hence the name active ideal gas.

Unlike equilibrium systems, active matter is not governed by the conventional laws of thermodynamics. Through a series of Langevin dynamics simulations and analytic calculations, we explore how systems cross over from equilibrium to active behavior as the activity is increased. In particular, we calculate the profiles of density and orientational order near straight or circular walls, and show the characteristic width of the boundary layers. We find a simple relationship between the enhancements of density and pressure near a wall. Based on these results, we determine how the pressure depends on wall curvature, and hence make approximate analytic predictions for the motion of curved tracers, as well as the rectification of active particles around small openings in confined geometries.

An interesting result that has been shown is that the system attains orientational and spatial order even when the particles do not interact with other particles but interact only with the walls. Our calculations provide analytical results to quantify order near or between walls. When two parallel walls are placed in an active particle bath, a Casimir-like force on the walls arises due to the activity of particles that form the bath. We derive approximate equation to describe the force in terms of the wall separation, persistance length of the particles, and other relevant parameters of the system.

Curvature has been shown to have important consequences in the order and symmetry

breaking of the system. In this work we also derive approximate analytic equations that describe the density and orientational order near curved walls. These results enable us to predict the net force on a curved tracer particle. We also introduce a mechanism to rectify the active particles by means of circular "corrals" with a small opening. Our analytical results enable us to predict how to tune the density of particles inside confinement.

1.3.3   Skyrmions in chiral magnets and cholesteric liquid crystals

The final system we study is the chiral nematic liquid crystals and chiral magnets under the influence of external fields and geometric frustration.

Most commonly known chiral phases in liquid crystals and magnetic systems are cholesteric phase and spiral phase respectively. These phases have a twist along one axis with a certain helical pitch. However they are not the only structures that can exist. For instance when chiral liquid crystals or magnets are subjected to applied fields or other anisotropic environments, the competition between favored twist and anisotropy leads to the formation of complex defect structures. In some cases, the defects are skyrmions, which have $180°$ double twist going outward from the center, and hence can pack together without singularities in the orientational order. In other cases, the defects are merons, which have $90°$ double twist going outward from the center; packing such merons requires singularities in the orientational order. In the liquid crystal context, a lattice of merons is regarded as a blue phase. Here, we perform theoretical and computational studies of skyrmions and merons in chiral liquid crystals and magnets. Through these studies, we calculate the phase diagrams for liquid crystals and magnets in terms of dimensionless ratios of energetic parameters. We also predict the range of metastability for liquid crystal

skyrmions, and show that these skyrmions can move and interact as effective particles. The results show how the properties of skyrmions and merons depend on the vector or tensor nature of the order parameter.

Furthermore we investigate possible ways of moving skyrmions. As generic solitons, skyrmions are formed in a background electric field and actuated by means of light, nonuniform electric field, and surface anchoring. Finally we also look into the behavior of skyrmions under pressure.

BIBLIOGRAPHY

[1] J. Selinger, *Introduction to the Theory of Soft Matter: From Ideal Gases to Liquid Crystals*. Springer International Publishing, 1 ed., 2016.

[2] P. G. de Gennes and J. Prost, *The Physics of Liquid Crystals*. Clarendon Press, 2 ed., 1995.

[3] T. Vicsek, A. Czirók, E. Ben-Jacob, I. Cohen, and O. Shochet, "Novel type of phase transition in a system of self-driven particles," *Phys. Rev. Lett.*, vol. 75, pp. 1226–1229, Aug 1995.

[4] S. Ramaswamy, "Active matter," *Journal of Statistical Mechanics: Theory and Experiment*, vol. 2017, no. 5, p. 054002, 2017.

[5] T. Bossomaier, L. Barnett, and M. Harré, "Information and phase transitions in socio-economic systems," *Complex Adaptive Systems Modeling*, vol. 1, p. 9, Apr 2013.

CHAPTER 2

Dynamic Theory Of Polydomain Liquid-crystal Elastomers[1]

Liquid-crystal elastomers are remarkable materials that combine the elastic properties of cross-linked polymer networks with the anisotropy of liquid crystals [1]. Any distortion of the polymer network affects the orientational order of the liquid crystal, and any change in the magnitude or direction of liquid-crystal order influences the shape of the polymer network. Hence, these elastomers are useful for applications as actuators or shape-changing materials.

For many applications, it is necessary to prepare monodomain liquid-crystal elastomers. In practice, this can be done by applying a mechanical load or other aligning field while crosslinking [2]. Surprisingly, elastomers prepared without an aligning field do not form monodomains. Rather, they form polydomain structures with nematic order in local regions, which are macroscopically disordered. These polydomain structures have been seen in many experiments, using a wide range of techniques [3–7]. Indeed, a recent polarized light scattering study shows that liquid-crystal elastomers evolve toward a state of increasing disorder as the isotropic-nematic transition proceeds, unless the disorder is suppressed by a gradually increasing load [8].

2.1 Theory

One important issue in the theory of liquid-crystal elastomers is how to understand the polydomain state. Several theoretical studies have attributed this state to quenched disorder in the polymer network, which can be understood by analogy with spin glass theory [9–17]. Effects of quenched disorder have further been modeled and visualized through numerical simulations [18–21]. More macroscopic theories have shown that the resulting polydomain structure has profound consequences for the material's effective elasticity [22, 23].

The purpose of this work is to suggest a different mechanism for the origin of the polydomain state, not related to quenched disorder. We develop a theory for the dynamics of the isotropic-nematic transition in liquid-crystal elastomers, in which growing nematic order is coupled to elastic strain. This theory is related to previous work on the dynamics of the nematic phase in these materials [1,24]. We explore the theory in two dimensions (2D), using two models for dynamic evolution of nematic order and strain. The theory shows that dynamics can itself select a characteristic length scale for a disordered polydomain structure, through a mechanism similar to the Cahn-Hilliard equation for phase separation. In particular, the theory predicts formation of structures with the form shown in Fig. 5. We suggest that this mechanism may play a role in formation of polydomain liquid-crystal elastomers, in addition to quenched disorder.

In the theory of 2D liquid-crystal elastomers, nematic order is described by the tensor order parameter $Q_{\alpha\beta}(\boldsymbol{r})$, and elastic distortion of the material by the displacement vector $\boldsymbol{u}(\boldsymbol{r})$. In terms of displacement, the strain tensor is $\epsilon_{\alpha\beta} = \frac{1}{2}[\partial_\alpha u_\beta + \partial_\beta u_\alpha + (\partial_\alpha u_\gamma)(\partial_\beta u_\gamma)]$;
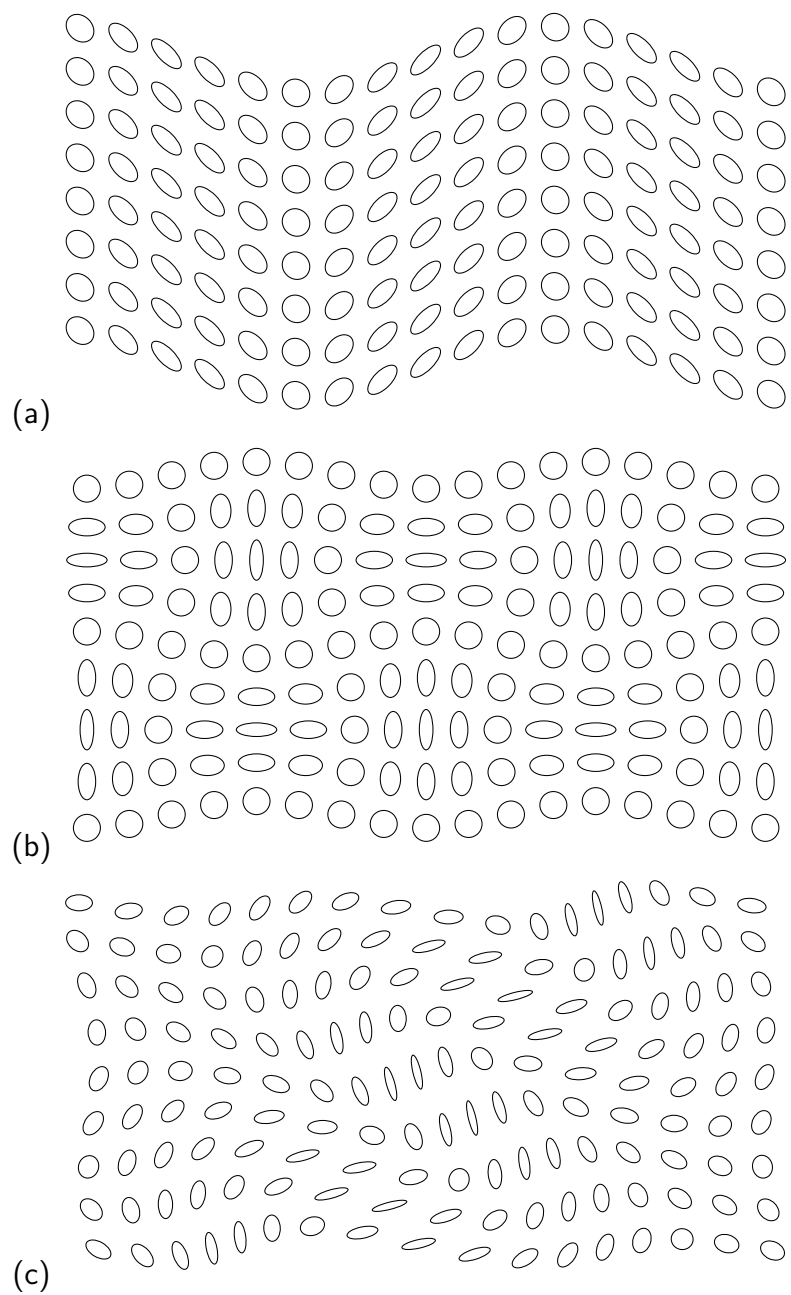
Figure 5: Visualization of liquid-crystal elastomer structures calculated here. The orientation and eccentricity of ellipses represents local nematic order (on a coarse-grained length scale much larger than individual mesogens). (a) Single wave in nematic order and displacement. (b) Superposition of two perpendicular waves, forming a square lattice. (c) Superposition of three waves with random directions, amplitudes, and phases.

we will consider only the linear terms for small $\boldsymbol{u}$. The free energy can be expressed in terms of $Q_{\alpha\beta}$ and $\epsilon_{\alpha\beta}$ as

$$F = \int d^2r \left[\frac{1}{2} a Q_{\alpha\beta} Q_{\alpha\beta} + \frac{1}{4} b (Q_{\alpha\beta} Q_{\alpha\beta})^2 \right.$$
$$+ \frac{1}{2} L (\partial_\gamma Q_{\alpha\beta})(\partial_\gamma Q_{\alpha\beta}) + \frac{1}{2} \lambda \epsilon_{\alpha\alpha} \epsilon_{\beta\beta}$$
$$\left. + \mu \epsilon_{\alpha\beta} \epsilon_{\alpha\beta} - V \epsilon_{\alpha\beta} Q_{\alpha\beta} \right]. \tag{2}$$

Here, the first two terms are the Landau-de Gennes expansion for the free energy in powers of the order tensor. The coefficient $a = a'(T - T_0)$ is assumed to vary linearly with temperature, while b is a positive constant. The third term is the Frank free energy for spatial variations in the order tensor, assuming a single Frank coefficient L. The fourth and fifth terms are the elastic free energy in terms of the strain tensor, with Lamé coefficients λ and μ. The final term is the coupling between nematic order and strain, with coefficient V.

If there were no coupling between nematic order and strain, $V = 0$, the system would have an isotropic-nematic transition at $a = 0$, corresponding to temperature T_0. With coupling $V \neq 0$, the transition is shifted upward to $a = V^2/(2\mu)$, corresponding to the higher temperature $T_{\text{IN}} = T_0 + V^2/(2\mu a')$. Above that temperature, the state of minimum free energy is uniformly isotropic, with $Q_{\alpha\beta} = 0$ and $\epsilon_{\alpha\beta} = 0$. Below that temperature, at $a = V^2/(2\mu) - \delta a$, the state of minimum free energy becomes uniformly nematic, with alignment along a randomly selected director $\hat{\boldsymbol{n}}$. In this state, the order tensor is $Q_{\alpha\beta} = S(2n_\alpha n_\beta - \delta_{\alpha\beta})$, where the magnitude of nematic order is $S = \sqrt{\delta a/(2b)}$. This state extends uniformly along the director, with strain $\epsilon_{\alpha\beta} = [V/(2\mu)] Q_{\alpha\beta}$.

Now suppose we begin in the isotropic phase, and rapidly cool to a temperature

slightly below T_{IN}. At this low temperature, nematic order and strain both begin to grow dynamically. We ask: Does the dynamic process lead to the state of minimum free energy, with uniform $Q_{\alpha\beta}$ and $\epsilon_{\alpha\beta}$? Alternatively, does it lead to a different, nonuniform state?

To answer this question, we develop a model for the dynamics of the phase transition. We actually consider two models, first simple linear drag and then more realistic viscous flow. In both models, we describe four coupled degrees of freedom: $Q_{xx}(\boldsymbol{r},t)$, $Q_{xy}(\boldsymbol{r},t)$, $u_x(\boldsymbol{r},t)$, and $u_y(\boldsymbol{r},t)$. The remaining components of $Q_{\alpha\beta}(\boldsymbol{r},t)$ are fixed because it is a symmetric, traceless tensor, and $\epsilon_{\alpha\beta}(\boldsymbol{r},t)$ can be derived from $\boldsymbol{u}(\boldsymbol{r},t)$. We cannot take the strain tensor components as our fundamental degrees of freedom because they are constrained by elastic compatibility; they must all be derivable from the same $\boldsymbol{u}(\boldsymbol{r},t)$.

In the simplest model of overdamped dynamics with linear drag, the rate of change for each degree of freedom is linearly proportional to the force acting on it. Hence, the equations of motion are

$$\frac{\partial Q_{xx}}{\partial t} = -\Gamma_Q \frac{\delta F}{\delta Q_{xx}}, \quad \frac{\partial Q_{xy}}{\partial t} = -\Gamma_Q \frac{\delta F}{\delta Q_{xy}},$$
$$\frac{\partial u_x}{\partial t} = -\Gamma_u \frac{\delta F}{\delta u_x}, \quad \frac{\partial u_y}{\partial t} = -\Gamma_u \frac{\delta F}{\delta u_y}, \tag{3}$$

where Γ_Q and Γ_u are mobility coefficients. To calculate the forces on the right side of those equations, we substitute the definition of the strain tensor into the free energy (2), and take functional derivatives with respect to $Q_{\alpha\beta}$ and u_α. We then linearize the equations, assuming that $Q_{\alpha\beta}$ and u_α are both small in early stages of nematic ordering. The

equations then become

$$\frac{\partial Q_{xx}}{\partial t} = \Gamma_Q \left[-2aQ_{xx} + 2L\nabla^2 Q_{xx} + V(\partial_x u_x - \partial_y u_y) \right],$$

$$\frac{\partial Q_{xy}}{\partial t} = \Gamma_Q \left[-2aQ_{xy} + 2L\nabla^2 Q_{xy} + V(\partial_x u_y + \partial_y u_x) \right],$$

$$\frac{\partial u_x}{\partial t} = \Gamma_u \left[(\lambda + \mu)\partial_x \boldsymbol{\nabla} \cdot \boldsymbol{u} + \mu\nabla^2 u_x - V(\boldsymbol{\nabla} \cdot \boldsymbol{Q})_x \right],$$

$$\frac{\partial u_y}{\partial t} = \Gamma_u \left[(\lambda + \mu)\partial_y \boldsymbol{\nabla} \cdot \boldsymbol{u} + \mu\nabla^2 u_y - V(\boldsymbol{\nabla} \cdot \boldsymbol{Q})_y \right]. \tag{4}$$

To simplify this system of equations, we Fourier transform from position $\boldsymbol{r}$ to wavevector $\boldsymbol{k}$, then write the equations in the matrix form

$$\frac{\partial}{\partial t} \begin{pmatrix} Q_{xx}(\boldsymbol{k},t) \\ Q_{xy}(\boldsymbol{k},t) \\ u_x(\boldsymbol{k},t) \\ u_y(\boldsymbol{k},t) \end{pmatrix} = -M(\boldsymbol{k}) \begin{pmatrix} Q_{xx}(\boldsymbol{k},t) \\ Q_{xy}(\boldsymbol{k},t) \\ u_x(\boldsymbol{k},t) \\ u_y(\boldsymbol{k},t) \end{pmatrix}, \tag{5}$$

where $M(\boldsymbol{k})$ is a 4×4 matrix. This matrix equation resembles the Cahn-Hilliard equation for phase separation of a binary fluid. At each $\boldsymbol{k}$, the matrix $M(\boldsymbol{k})$ has four eigenmodes i, which either grow or decay exponentially as $e^{-\Lambda_i(\boldsymbol{k})t}$, where $\Lambda_i(\boldsymbol{k})$ is the corresponding eigenvalue of $M(\boldsymbol{k})$. Note that $\Lambda_i(\boldsymbol{k}) < 0$ corresponds to exponential growth, while $\Lambda_i(\boldsymbol{k}) > 0$ corresponds to exponential decay. We must determine what grows most rapidly: which eigenmode at which wavevector?

To identify the fastest-growing mode, we choose coordinates such that $\boldsymbol{k}$ is along the

x-axis. The matrix then simplifies to

$$M(\boldsymbol{k}) = \tag{6}$$

$$\begin{pmatrix} 2\Gamma_Q(a + Lk^2) & 0 & -i\Gamma_Q Vk & 0 \\ 0 & 2\Gamma_Q(a + Lk^2) & 0 & -i\Gamma_Q Vk \\ i\Gamma_u Vk & 0 & \Gamma_u(\lambda + 2\mu)k^2 & 0 \\ 0 & i\Gamma_u Vk & 0 & \Gamma_u\mu k^2 \end{pmatrix}.$$

We now take the limit of an incompressible material, with $\lambda \to \infty$. In this limit, u_x has a high energy cost, so that it decays rapidly, and hence we eliminate it from consideration. In that case, Q_{xx} is not coupled to any other degrees of freedom, so it is an eigenmode by itself, with eigenvalue $2\Gamma_Q(a + Lk_x^2)$. If the system is at a temperature slightly below the isotropic-nematic transition, we must have $0 < a < V^2/(2\mu)$. In that temperature range, this eigenvalue is positive, so that Q_{xx} decays exponentially. Hence, we also eliminate it from consideration in the search for the fastest-growing mode.

The remaining two modes are linear combinations of Q_{xy} and u_y, with eigenvalues

$$\Lambda_\pm(k) = \Gamma_Q(a + Lk^2) + \tfrac{1}{2}\Gamma_u\mu k^2 \tag{7}$$
$$\pm \sqrt{\left[\Gamma_Q(a + Lk^2) - \tfrac{1}{2}\Gamma_u\mu k^2\right]^2 + \Gamma_Q\Gamma_u V^2 k^2}$$

Figure 6 shows a sample plot of these two eigenvalues as functions of k. The eigenvalue $\Lambda_+(k)$ begins at $2\Gamma_Q a$ when $k = 0$, then increases with increasing k. For temperatures just below the isotropic-nematic transition, with $0 < a < V^2/(2\mu)$, it is always positive and hence represents a decaying mode. By contrast, $\Lambda_-(k)$ begins at 0 when $k = 0$, then decreases into negative values over the range $0 < k < \sqrt{\delta a/L}$, where $\delta a = V^2/(2\mu) - a$, and eventually returns to positive values for larger k. Over the range in which it is negative,

23
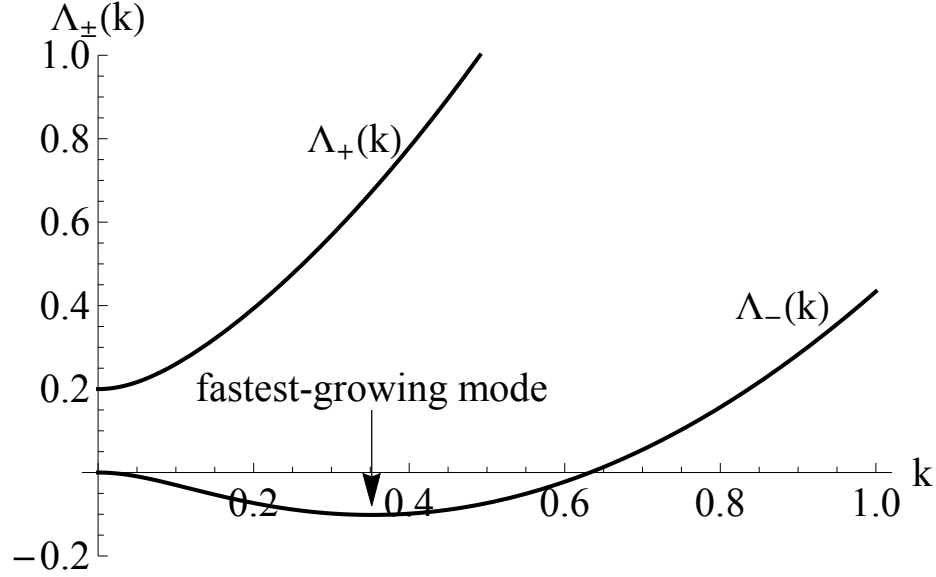
Figure 6: Sample plot of the eigenvalues $\Lambda_\pm(\boldsymbol{k})$ in the linear drag model of dynamics, with parameters $a = 0.1$ and $L = \mu = V = \Gamma_Q = \Gamma_u = 1$. The largest negative eigenvalue corresponds to the fastest-growing mode, which occurs at a dynamically selected wavevector.

it represents an exponentially growing mode. To find the fastest-growing wavevector, we minimize $\Lambda_-(k)$ over k. For temperatures just below the isotropic-nematic transition, for small δa, this wavevector is $k_{\text{fastest}} \approx \sqrt{\delta a/(2L)}$, and the corresponding growth rate is $|\Lambda_-(k_{\text{fastest}})| \approx \Gamma_u \mu^2 \delta a^2/(2LV^2)$.

We emphasize that this wavevector is selected through a dynamic mechanism. It is not the minimum of the free energy (which is a state of uniform nematic order and strain). Moreover, it only occurs because of the coupling V between nematic order and strain in a liquid-crystal elastomer. If these variables were uncoupled $(V = 0)$, the matrix M would be diagonal, the isotropic-nematic transition would occur at $a = 0$, and the fastest-growing mode below that transition would be $k = 0$.

To characterize the fastest-growing mode, we calculate the eigenvector of M corresponding to eigenvalue Λ_- at wavevector k_{fastest}. This eigenvector represents waves in both Q_{xy} and u_y (with our assumption that the wavevector is in the x-direction), and

these waves are $90°$ out of phase. Figure 5(a) shows a sample visualization of the structure with a single Fourier mode. It has alternating stripes with the director oriented at $\pm 45°$ from the wavevector, accompanied by displacement perpendicular to the wavevector.

In general, a liquid-crystal elastomer will not have only one Fourier mode. Rather, it can include modes with wavevectors of magnitude k_{fastest} in multiple directions. To find a mode in an arbitrary direction, we rotate the wavevector, and make a corresponding rotation of $Q_{\alpha\beta}$ and $\boldsymbol{u}$. We then add up the Fourier modes to find the structure. Figure 5(b) shows an example with two perpendicular waves of equal amplitude, leading to a square lattice in the nematic order and the displacement. Figure 5(c) shows a more realistic example with a superposition of three waves with random directions, amplitudes, and phases.

The structures in Fig. 5 are similar to structures commonly observed in experiments and simulations on *active* nematic liquid crystals [25]. This similarity is reasonable, because both systems are controlled by couplings between orientational order and extension of the material.

The growth of nematic order in a liquid-crystal elastomer can be described by the dynamic correlation function

$$C(|\boldsymbol{r} - \boldsymbol{r}'|, t) = \langle \cos 2[\theta(\boldsymbol{r}) - \theta(\boldsymbol{r}')] \rangle_t$$

$$= \langle Q_{xx}(\boldsymbol{r}, t) Q_{xx}(\boldsymbol{r}', t) + Q_{xy}(\boldsymbol{r}, t) Q_{xy}(\boldsymbol{r}', t) \rangle$$

$$= \sum_{\boldsymbol{k}} e^{i\boldsymbol{k} \cdot (\boldsymbol{r} - \boldsymbol{r}')} \left\langle |Q_{xx}(\boldsymbol{k}, t)|^2 + |Q_{xy}(\boldsymbol{k}, t)|^2 \right\rangle . \tag{8}$$

This sum is dominated by the fastest-growing mode at wavevectors with magnitude k_{fastest},

and hence

$$C(|\boldsymbol{r} - \boldsymbol{r}'|, t) \propto \int_0^{2\pi} \frac{d\phi}{2\pi} e^{ik_{\text{fastest}}|\boldsymbol{r}-\boldsymbol{r}'|\cos\phi} e^{2|\Lambda_-(k_{\text{fastest}})|t}$$

$$\propto J_0(k_{\text{fastest}}|\boldsymbol{r} - \boldsymbol{r}'|)e^{2|\Lambda_-(k_{\text{fastest}})|t}. \tag{9}$$

Thus, in the early stages of growth, the correlation function has the form of Bessel function $J_0(k_{\text{fastest}}|\boldsymbol{r} - \boldsymbol{r}'|)$, with an exponentially increasing magnitude. In later stages of growth, the approximation of small nematic order ceases to apply, and other types of modeling are needed. Even so, the length scale of $1/k_{\text{fastest}}$ is established from the early stages.

The dynamic model presented above has a limitation: It assumes that both $Q_{\alpha\beta}(\boldsymbol{r}, t)$ and $\boldsymbol{u}(\boldsymbol{r}, t)$ have overdamped dynamics, with drag forces linearly proportional to the rate of change of these quantities. This assumption is appropriate for dynamics on a substrate, where the dissipation is caused by drag against the substrate. However, if there is no substrate, it is reasonable to generalize the dynamics in two ways: by considering inertia for the displacement and by considering viscous dissipation rather than drag against a substrate.

For this generalization, we use the equations of motion

$$\rho\frac{\partial^2 u_\alpha}{\partial t^2} = -\frac{\delta D}{\delta \dot{u}_\alpha} - \frac{\delta F}{\delta u_\alpha},$$

$$0 = -\frac{\delta D}{\delta \dot{Q}_{\alpha\beta}} - \frac{\delta F}{\delta Q_{\alpha\beta}}. \tag{10}$$

Here ρ is the mass density, which gives inertia for $\boldsymbol{u}$; there is no inertia for $Q_{\alpha\beta}$. Also, D is the Rayleigh dissipation function, which can be written as

$$D = \int d^2r \left[\eta A_{\alpha\beta}A_{\alpha\beta} + \frac{1}{2}\gamma_1 B_{\alpha\beta}B_{\alpha\beta} + \gamma_2 A_{\alpha\beta}B_{\alpha\beta}\right] \tag{11}$$

26

in terms of the two modes that dissipate energy: $A_{\alpha\beta} = \frac{1}{2}(\partial_\alpha \dot{u}_\beta + \partial_\beta \dot{u}_\alpha)$ is the rate of shear flow, and $B_{\alpha\beta} = \dot{Q}_{\alpha\beta} - \omega_z(\epsilon_{\delta\alpha} Q_{\delta\beta} + \epsilon_{\delta\beta} Q_{\delta\alpha})$ is the rotation rate of nematic order relative to rotational flow of the material, given by $\omega_z = \frac{1}{2}\epsilon_{\mu\nu}\partial_\mu \dot{u}_\nu$. In these expressions, η is the viscosity, γ_1 is the rotational viscosity, and γ_2 is a dissipative coupling coefficient.

We combine these expressions to derive the coupled equations of motion for Q_{xx}, Q_{xy}, u_x, and u_y, and linearize the equations assuming these variables are small in the early stages of nematic ordering. We then follow the same steps as in the previous calculation: Fourier transform from $\boldsymbol{r}$ to $\boldsymbol{k}$, choose coordinates such that $\boldsymbol{k}$ is along the x-axis, eliminate u_x by the constraint of incompressibility, and eliminate Q_{xx} because it is an independent, exponentially decaying mode. We are left with a matrix equation for $Q_{xy}(\boldsymbol{k}, t)$ and $u_y(\boldsymbol{k}, t)$,

$$\begin{pmatrix} 0 & 0 \\ 0 & \rho \end{pmatrix} \begin{pmatrix} \ddot{Q}_{xy} \\ \ddot{u}_y \end{pmatrix} = -\begin{pmatrix} 4\gamma_1 & i\gamma_2 k \\ -i\gamma_2 k & \eta k^2 \end{pmatrix} \begin{pmatrix} \dot{Q}_{xy} \\ \dot{u}_y \end{pmatrix} \tag{12}$$
$$-\begin{pmatrix} 2(a + Lk^2) & -iVk \\ iVk & \mu k^2 \end{pmatrix} \begin{pmatrix} Q_{xy} \\ u_y \end{pmatrix}.$$

Next we Fourier transform from time t to frequency ω, and obtain

$$\begin{pmatrix} 2(a + Lk^2) - 4i\gamma_1\omega & -iVk + \gamma_2\omega k \\ iVk - \gamma_2\omega k & \mu k^2 - i\eta\omega k^2 - \rho\omega^2 \end{pmatrix} \begin{pmatrix} Q_{xy} \\ u_y \end{pmatrix} = 0. \tag{13}$$

In this matrix equation, there are two couplings between Q_{xy} and u_y: the elastic coupling V and the dissipative coupling γ_2. For simplicity, we set $\gamma_2 = 0$ and consider only the elastic coupling.

The matrix equation only allows nontrivial Q_{xy} and u_y if the determinant of the matrix is zero. Hence, we set the determinant to zero and solve for the allowed frequencies ω.

Because the determinant is a cubic function of ω, there are three solutions. Expanding to first order in $1/\rho$, the solutions are

$$\omega_0(k) = -\frac{i(a + Lk^2)}{2\gamma_1} + \frac{i\gamma_1 V^2 k^2}{\rho(a + Lk^2)^2}, \tag{14}$$

$$\omega_\pm(k) = \pm k\sqrt{\frac{\mu}{\rho} - \frac{V^2}{2\rho(a + Lk^2)}} - \frac{ik^2}{2\rho}\left[\eta + \frac{\gamma_1 V^2}{(a + Lk^2)^2}\right].$$

Here, a real part of ω represents oscillation, a negative imaginary part represents exponential decay, and a positive imaginary part represents exponential growth.

The solution $\omega_0(k)$ is a purely damped mode. Whether the system is in the isotropic phase, $a > V^2/(2\mu)$, or slightly in the nematic phase, $0 < a < V^2/(2\mu)$, this mode decays exponentially.

The modes $\omega_\pm(k)$ depend on whether system is in the isotropic or nematic phase. In the isotropic phase, $a > V^2/(2\mu)$, these modes are damped sound waves, with both oscillation and exponential decay. By comparison, when the system is cooled slightly into the nematic phase, $0 < a < V^2/(2\mu)$, these modes change into pure exponential growth or decay. One of the modes has a negative imaginary part for all k, corresponding to decay, but the other mode has a positive imaginary part for a range of k, corresponding to growth.

Figure 7 shows a sample plot of the mode structure in the nematic phase. We can see that the $\omega_0(k)$ and $\omega_-(k)$ modes are decaying for all k, but the $\omega_+(k)$ mode is growing for a range of k. In this respect, it resembles the growing mode in the linear drag model of dynamics, shown in Fig. 6. In the limit of high ρ, the range of exponential growth is $0 < k < \sqrt{\delta a/L}$, and the fastest-growing wavevector is $k_{\text{fastest}} \approx \sqrt{\delta a/(2L)}$, where $\delta a = V^2/(2\mu) - a$. These results are equivalent to corresponding results for the linear
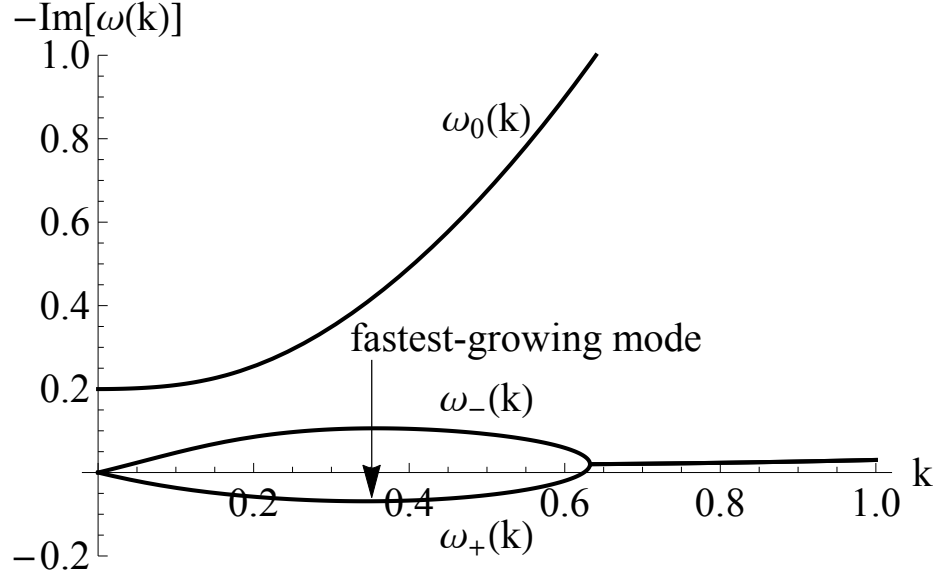
Figure 7: Sample plot of the mode structure in the generalized model of dynamics, with inertia and viscosity. Parameters are $a = 0.1$, $L = \mu = V = \eta = 1$, $\gamma_1 = 0.25$, and $\rho = 20$. The quantity $-\mathrm{Im}[\omega(k)]$ is the exponential decay rate, equivalent to $\Lambda_\pm(k)$ in Fig. 6. The largest *positive* value of $\mathrm{Im}[\omega(k)]$ corresponds to the fastest-growing mode.

drag model.

Hence, the generalized model of dynamics (with inertia and viscosity) leads to the same conclusion as the linear drag model: The dynamic mechanism of the isotropic-nematic transition selects a fastest-growing wavevector. This fastest-growing wavevector is not the minimum of the free energy, and it only occurs because of the coupling between nematic order and strain. We expect modulations with this wavevector to grow in liquid-crystal elastomers cooled below the isotropic-nematic transition, leading to structures with the form shown in Fig. 5.

To be sure, both models of dynamics presented here apply only to early stages of growth of nematic order. In later stages, as nematic order becomes more established, we cannot assume that $Q_{\alpha\beta}(\boldsymbol{r}, t)$ and $\boldsymbol{u}(\boldsymbol{r}, t)$ are small. In that case, our linearization of the equations of motion breaks down, and the dynamics must be studied through other

techniques, such as numerical simulation (see the next section for simulations). Hence, the linear model is not sufficient to tell whether the polydomain structure will persist into longer time, or will eventually coarsen into a uniform structure. In the late stages of dynamics, pre-existing quenched disorder may lock in the polydomain structure at the length scale given by dynamics, and prevent it from coarsening away. Alternatively, the dynamically induced polydomain structure may be fixed by the cross-linking process, so that it provides a source of quenched disorder for future processes in the elastomer.

2.2   Simulations

2.2.1   Free Energy

We use the free energy in equation (2) with a modification to the first term which is

$$\frac{1}{2}a\operatorname{Tr}\left[\overset{\leftrightarrow}{Q}{}^{2}\right] + \frac{1}{4}b\operatorname{Tr}\left[\overset{\leftrightarrow}{Q}{}^{2}\right]^{2} = aS^{2} + bS^{4}$$

where we used the substitution $\operatorname{Tr}\left[\overset{\leftrightarrow}{Q}{}^{2}\right] = (Q_{\mathsf{xx}}{}^{2} + Q_{\mathsf{xy}}{}^{2}) = 2S^{2}$. This expression allowed us to obtain analytical solutions, but for simulations we would like a version in which the scalar order paramter S cannot exceed 1. With that aim, we carry out a Maier-Saupe style calculation (appendix 2.C) and show that the first term can be replaced by $aS^{2} - 2b\left(S^{2} + \log\left[1 - S^{2}\right]\right)$. We also would like to keep the triangles of the mesh at constant area so that they do not collapse. The λ term preserves the volume if we do the substitution

$$\operatorname{Tr}(\overset{\leftrightarrow}{\epsilon}) \to \operatorname{Tr}(\overset{\leftrightarrow}{\epsilon}) + 2\det\overset{\leftrightarrow}{\epsilon},$$

as shown in appendix 2.B. With these, the free energy we use in the simulations takes the
form

$$
\begin{aligned}
F = & S^2 - 2b\left(S^2 + \log\left[1 - S^2\right]\right) + \frac{1}{2}L\sum_{i=1}^{2}\mathrm{Tr}\left[\frac{\partial\overleftrightarrow{Q}}{\partial r_i} \cdot \frac{\partial\overleftrightarrow{Q}}{\partial r_i}\right] \\
& + \frac{1}{2}\lambda\left(\mathrm{Tr}[\overleftrightarrow{\epsilon}] + 2\det\overleftrightarrow{\epsilon}\right)^2 + \mu\,\mathrm{Tr}[\overleftrightarrow{\epsilon} \cdot \overleftrightarrow{\epsilon}] - V\,\mathrm{Tr}[\overleftrightarrow{\epsilon} \cdot \overleftrightarrow{Q}]
\end{aligned}
\tag{15}
$$

2.2.2 Model

We carry out finite-element simulations with relaxational dynamics. In this method we
divide the area of (2D) the material into polygonal elements whose vertices are described
by a mesh. In each element we define all the variables necessary to calculate the free energy
given above (15). These variables are the two independent components for each of the
tensors $\overleftrightarrow{\epsilon}$ and $\overleftrightarrow{Q}$ namely ϵ_{xx}, ϵ_{xy}, Q_{xx}, and Q_{xy}. The calculation of strain in each polygon
is done using the coordinates of the mesh points. In order to use linear interpolation in
each element, we need to define a mesh made of triangles as linear interpolation of the
strain is not possible over a polygon with more than three vertices.

To calculate the derivatives of $\overleftrightarrow{Q}$, we use finite differences. Square lattice description
is an easy way of calculating finite differences but we need a triangular mesh for the
calculation of strain as explained above. Thus we choose for our mesh square unit cells
divided diagonally into two triangles. There are two different diagonals of the square one
can draw so there are two different possible ways of dividing the unit cell into triangles.
We chose to alternate the diagonals between neighboring squares (see Fig. 8). For each
unit square cell, using the vertex coordinates, we calculate two parts of the strain energy
coming from "upper" and "lower" triangles. There are different methods one can calculate
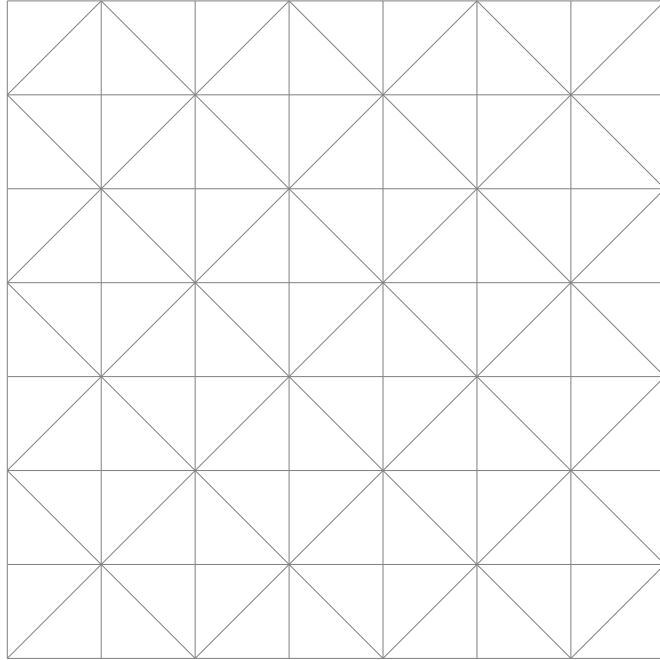
Figure 8: Mesh used in finite element simulations.

the strain from the vertex points all of which include usage of a deformation described by comparing the undeformed and deformed coordinates. Here we use a strain tensor described in the lab reference frame. See appendix 2.A for the calculation of this tensor from the vertex coordinates.

As for the LC part, we assign a nematic order parameter for each square rather than for each triangle. This is for the sake of simplicity in the data structure and in defining the nearest neighbors.

2.2.3 Dynamic equation

Adopting the model above and the viscous drag for the dissipation mechanism, we use the following algorithm to calculate time evolution of the shape and LC order. At each lattice point i, j we update the components of $\overset{\leftrightarrow}{Q}$ tensor and positions $R_{ij} = (X_{ij}, Y_{ij})$ according to the dynamic equation 10

$$\rho \frac{\partial^2 u_\alpha}{\partial t} = -\frac{\delta D}{\delta \dot{u}_\alpha} - \frac{\delta F}{\delta u_\alpha},$$

$$0 = -\frac{\delta D}{\delta \dot{Q}_{\alpha\beta}} - \frac{\delta F}{\delta Q_{\alpha\beta}}. \tag{16}$$

In the first equation above, we can calculate the accelaration of the $\vec{R}$ coordinates. However, the second equation doesn't give an explicit solution for any of the quantities so we need to check what the derivatives yield.

$$\frac{\delta D}{\delta \dot{Q}_{\alpha\beta}} = 4\Gamma_1 \dot{Q}_{\alpha\beta} = \frac{1}{\Gamma_Q} \dot{Q}_{\alpha\beta},$$

thus we rewrite the dynamic equations, v being $\frac{\partial u}{\partial t}$, as

$$\frac{\partial v_\alpha}{\partial t} = -\frac{1}{\rho} \left(\frac{\delta D}{\delta \dot{u}_\alpha} + \frac{\delta F}{\delta u_\alpha} \right),$$

$$\frac{\partial Q_{\alpha\beta}}{\partial t} = -\Gamma_Q \frac{\delta F}{\delta Q_{\alpha\beta}}. \tag{17}$$

The updates are done using

$$v_\alpha(t + \Delta t) = v_\alpha(t) + \Delta t \frac{\partial v_\alpha}{\partial t} \tag{18}$$

$$R_\alpha(t + \Delta t) = R_\alpha(t) + \Delta t \, v_\alpha \tag{19}$$

$$Q_{\alpha\beta}(t + \Delta t) = Q_{\alpha\beta}(t) + \Delta t \frac{\partial Q_{\alpha\beta}}{\partial t}. \tag{20}$$

At each time step, the dissipation function and the free energy are calculated for each cell and its neighbors. The derivatives are calculated from these variables by the method of finite differences.

2.2.4   Results

For a regular liquid crystal with no coupling to a polymer network, Landau style free energy we have used indicates an isotropic-nematic (IN) phase transition at $a = 0$ where

a can be thought of a temperature-like variable given by $a = a'(T - T_0)$. In the presence of the coupling represented by the coupling coefficient V, we deduce from the free energy expression that the same phase transition occurs at $a = \frac{V^2}{2\mu}$. When below the critical temperature corresponding to $a = \frac{V^2}{2\mu} - \delta a$ the analytical calculations above predict that the fastest growing mode yields a domain size *proportional to* $1/k_{\text{fastest}} = \sqrt{2L/\delta a}$. Thus we are interested in how the the dynamics of domain size depends on the temperature and the coupling strength namely δa and V. We would like to compare analytical predictions with simulations.

Our simulations agree with the predicted analytical calculations. First we check the phase behavior; we start with a very disordered initial state corresponding to a high temperature. Then the system is quickly cooled down to a temperature set by δa. As indicated by the theory, if $a < \frac{V^2}{2\mu}$ the final state is nematic, otherwise isotropic.

In the following pictures we show snapshots from a sample simulation which includes *crossed-polarizer* view, *light scattering* view, and correlation function of $\overset{\leftrightarrow}{Q}$.

Snapshots from a sample simulation.

Time=10.24
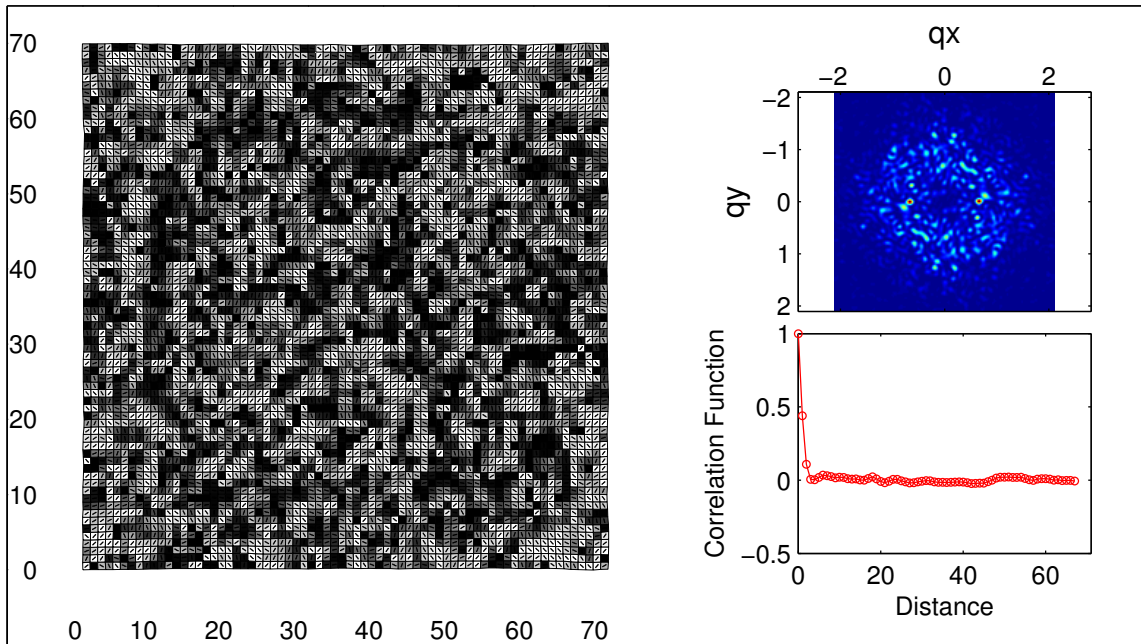
(a)

Time=20.48
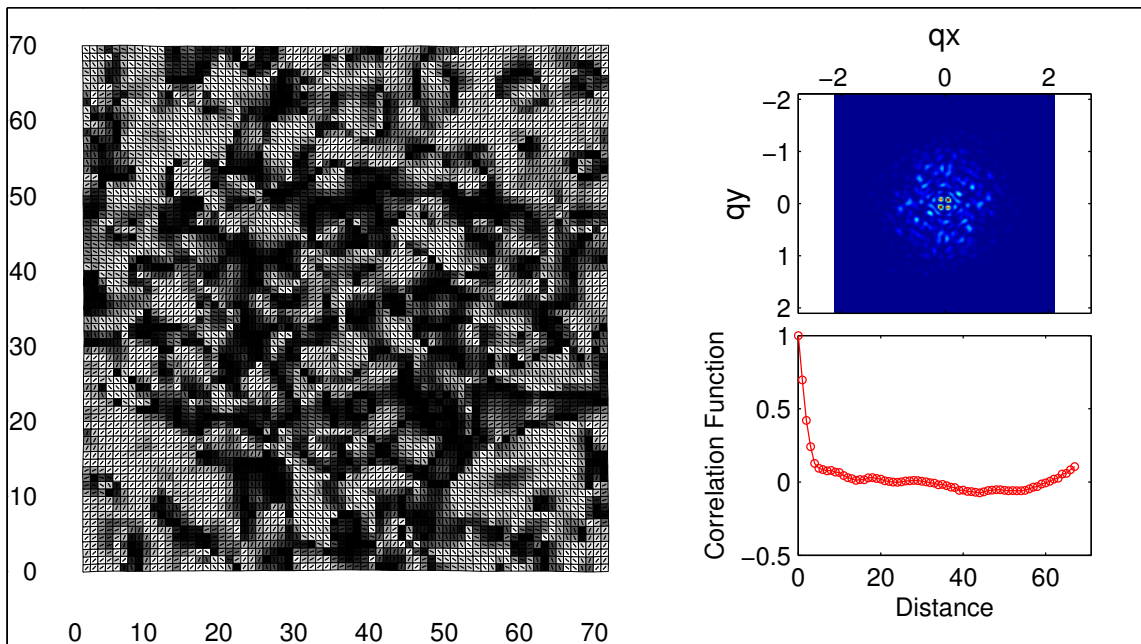
(b)

Time=40.96
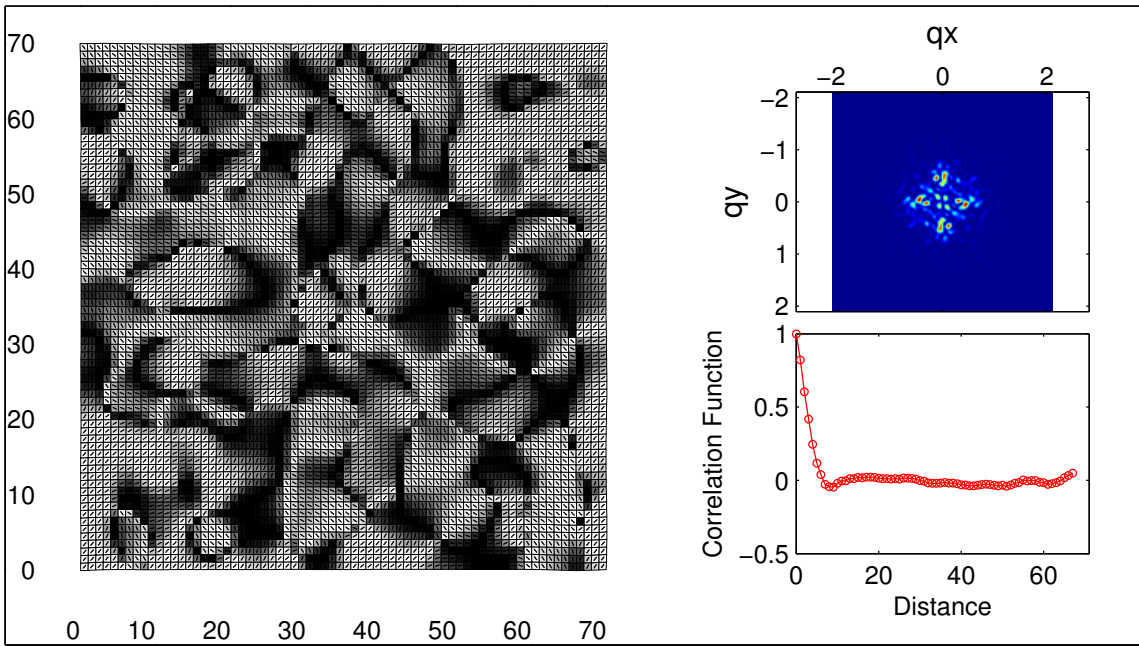
(c)

Time=81.92
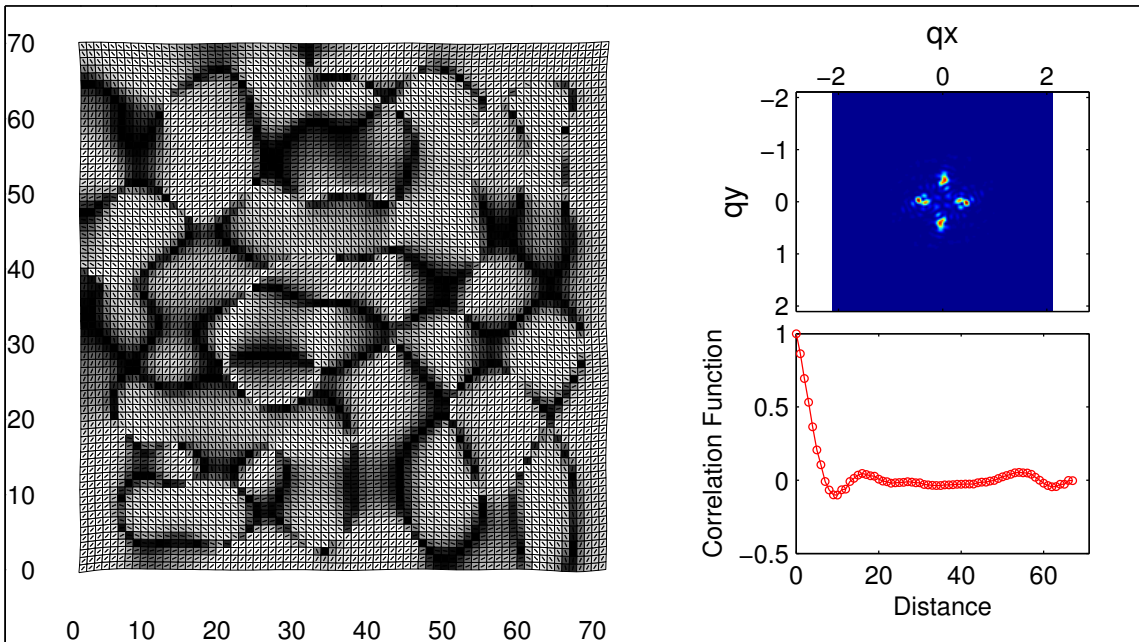
(d)

Time=163.84

(e)

Time=327.68

(f)

Time=655.36

qx

qy

Correlation Function

Distance

(g)

Time=1310.72

qx

qy

Correlation Function

Distance
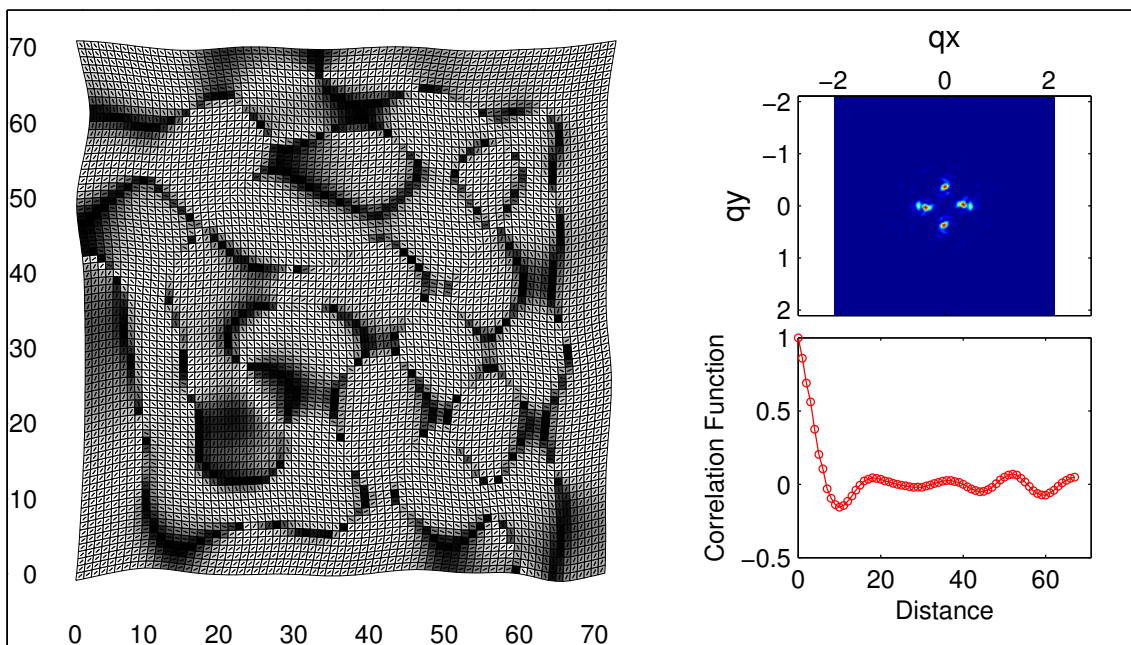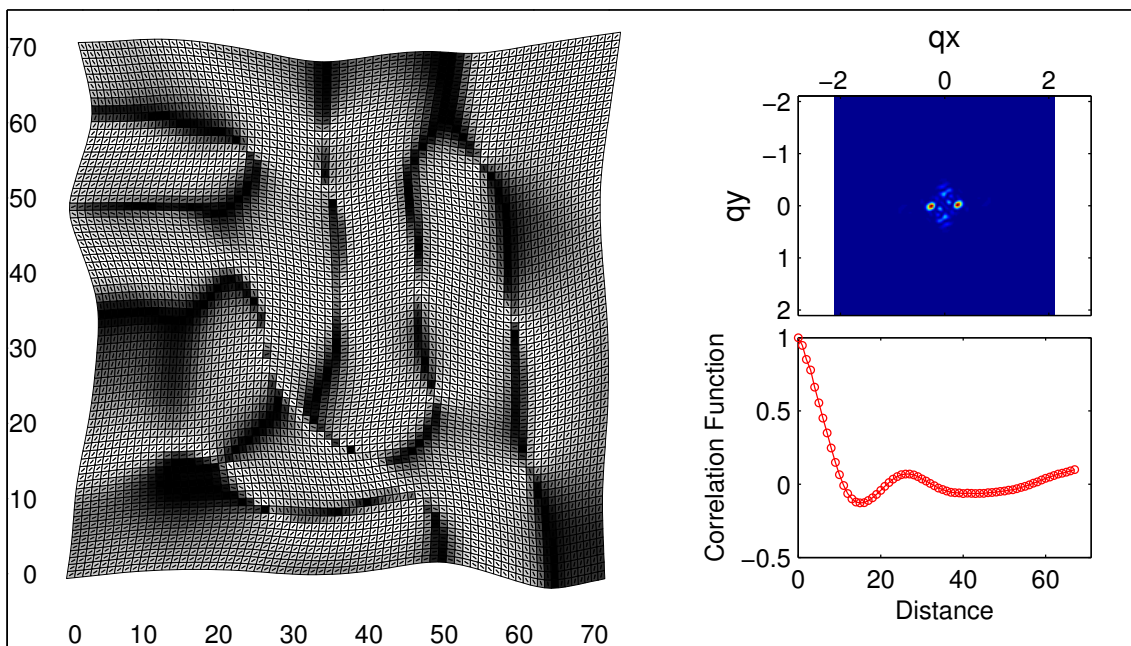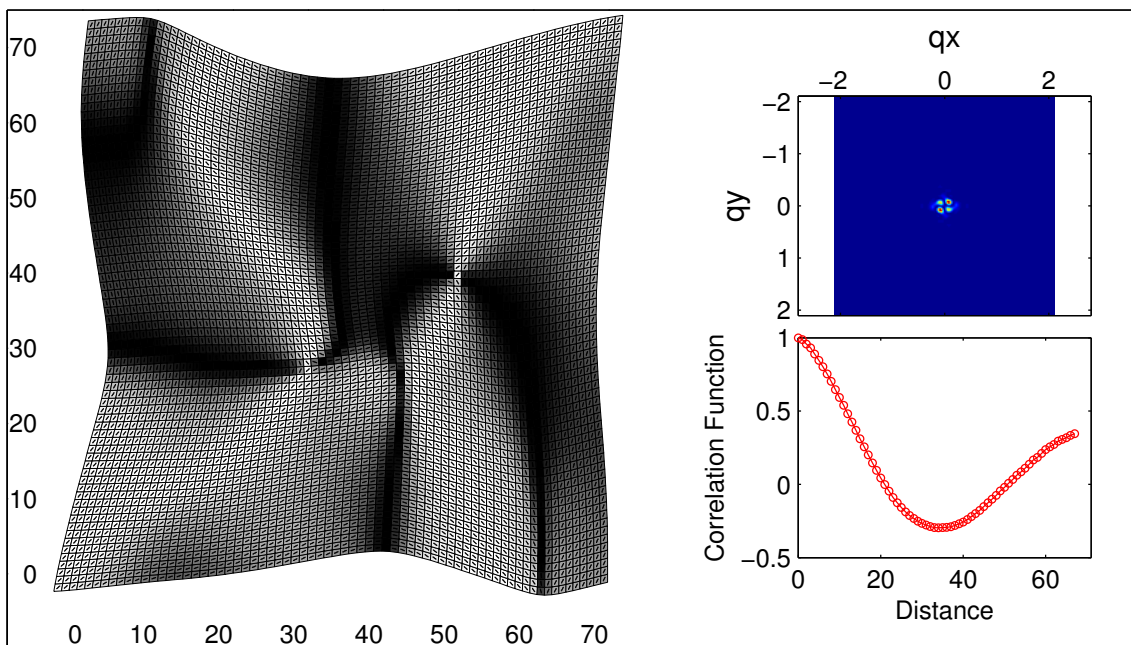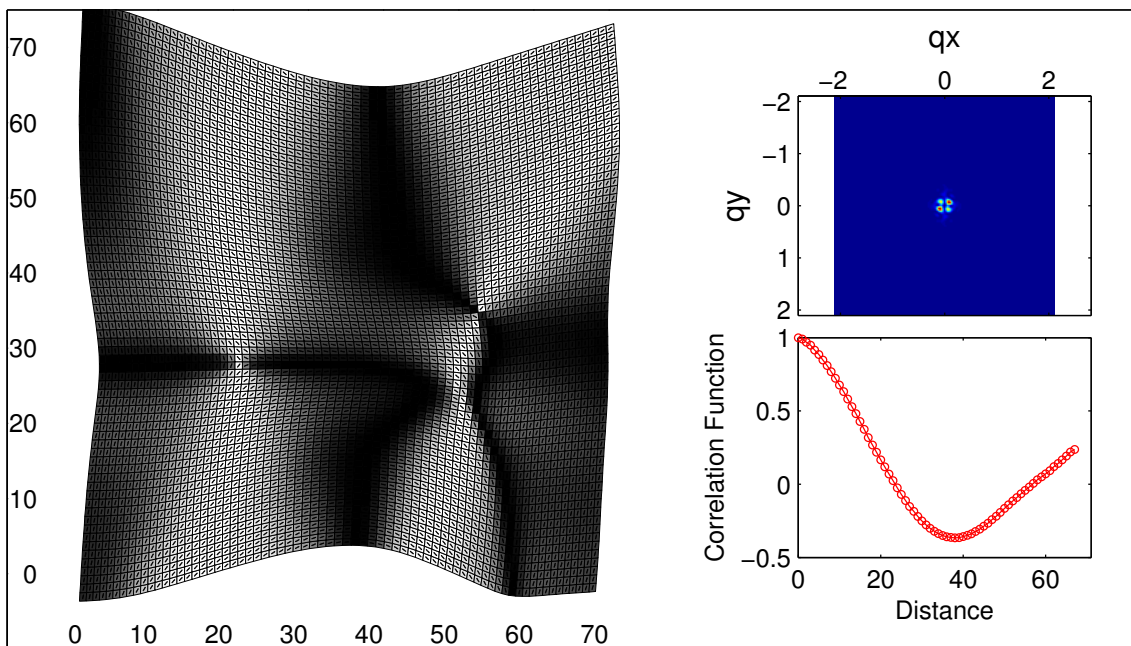
(h)

Time=2621.44

(i)

Time=5242.88

(j)
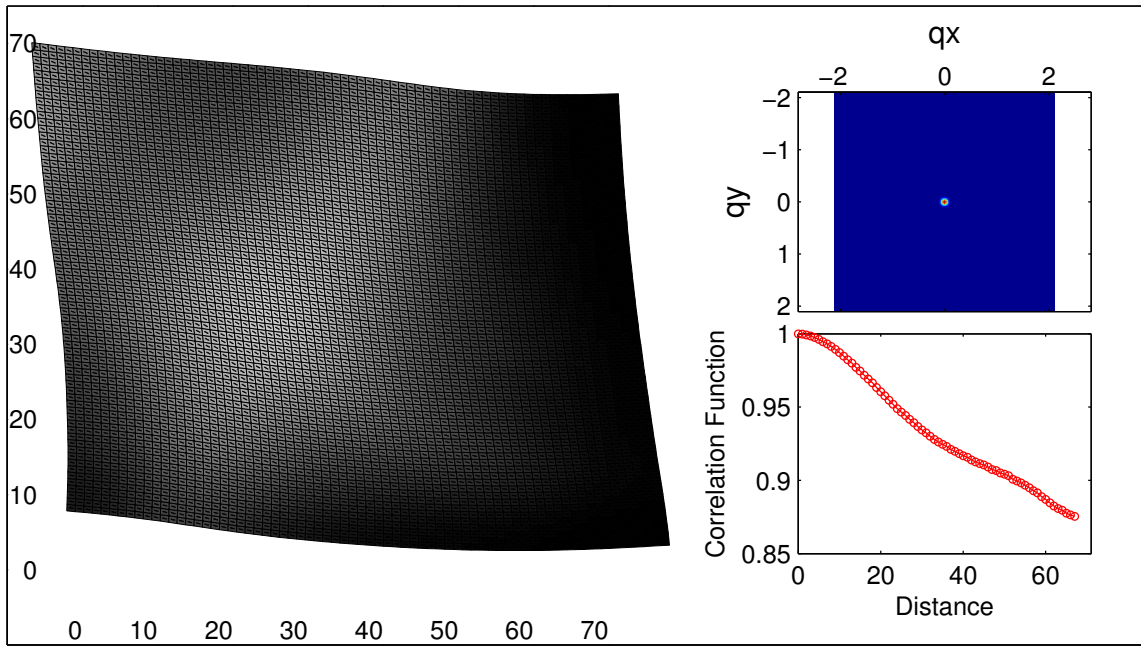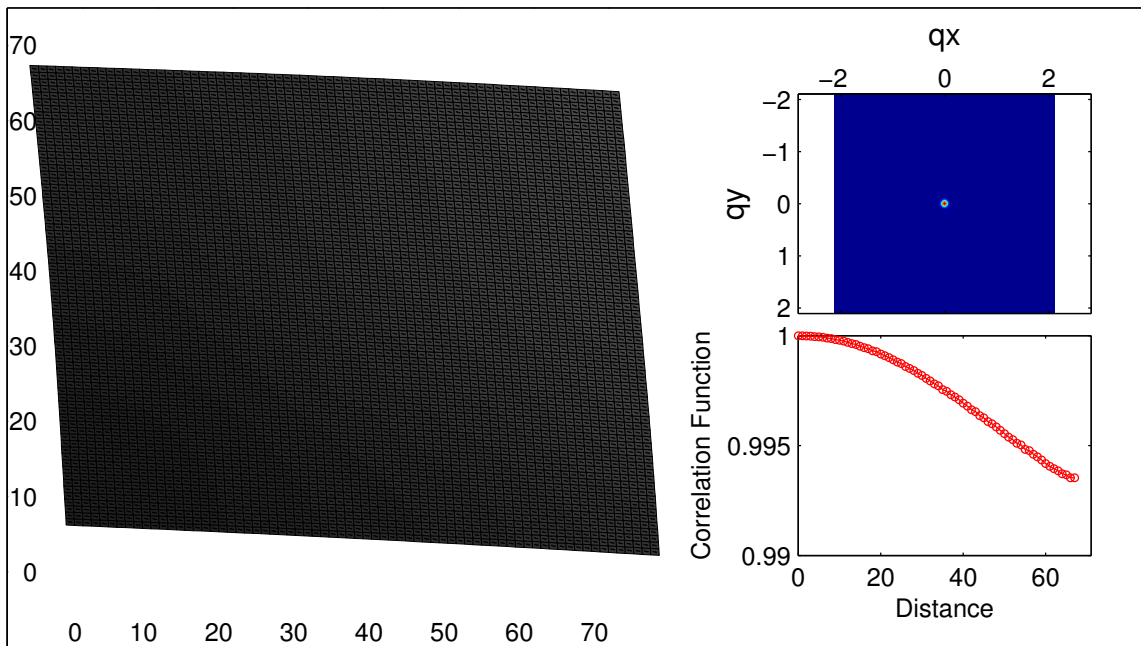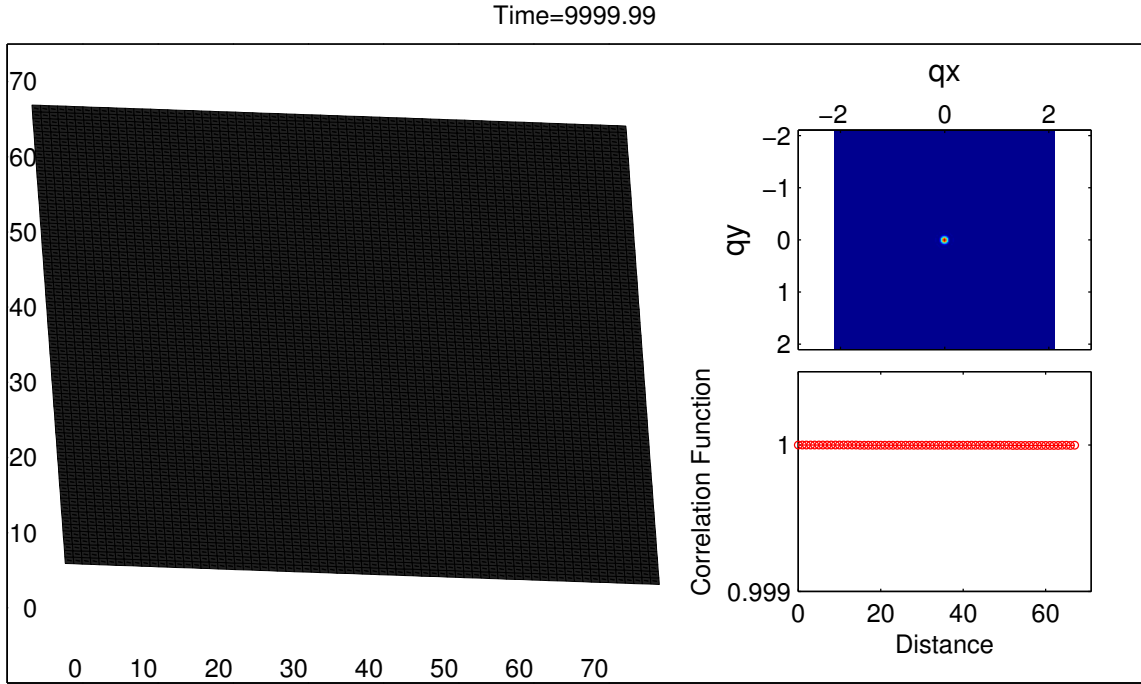
Figure 9: Simulation of a 71×71 lattice with parameters $\mu = 2$, $V = 4$. Main figure: crossed polarizer view of the LCE, obtanied by grey scale coloring according to $\sin^2(2\theta)$. Top right: light scattering view obtained by Fourier transform. Bottom right: correlation function of Q.

Nematic order starts growing in the initially disordered system and domains start nucleating. After the initial nucleation, we see a characteristic domain size that depends on δa which is proportional to the temperature drop below the equilibrium isotropic-nematic transition. This size remains approximately constant for some amount of time (Fig. 9 a-e), and then starts to grow, eventually reaching the size of the simulated system (Fig. 9 e-k). To quantify the domain size we numerically calculate the correlation function $C(|r - r'|) = \langle \cos 2[\theta(r) - \theta(r')] \rangle$ and find the distance $|r - r'|$ at which first minimum occurs. The analytical counterpart for the comparison comes from the first minimum of
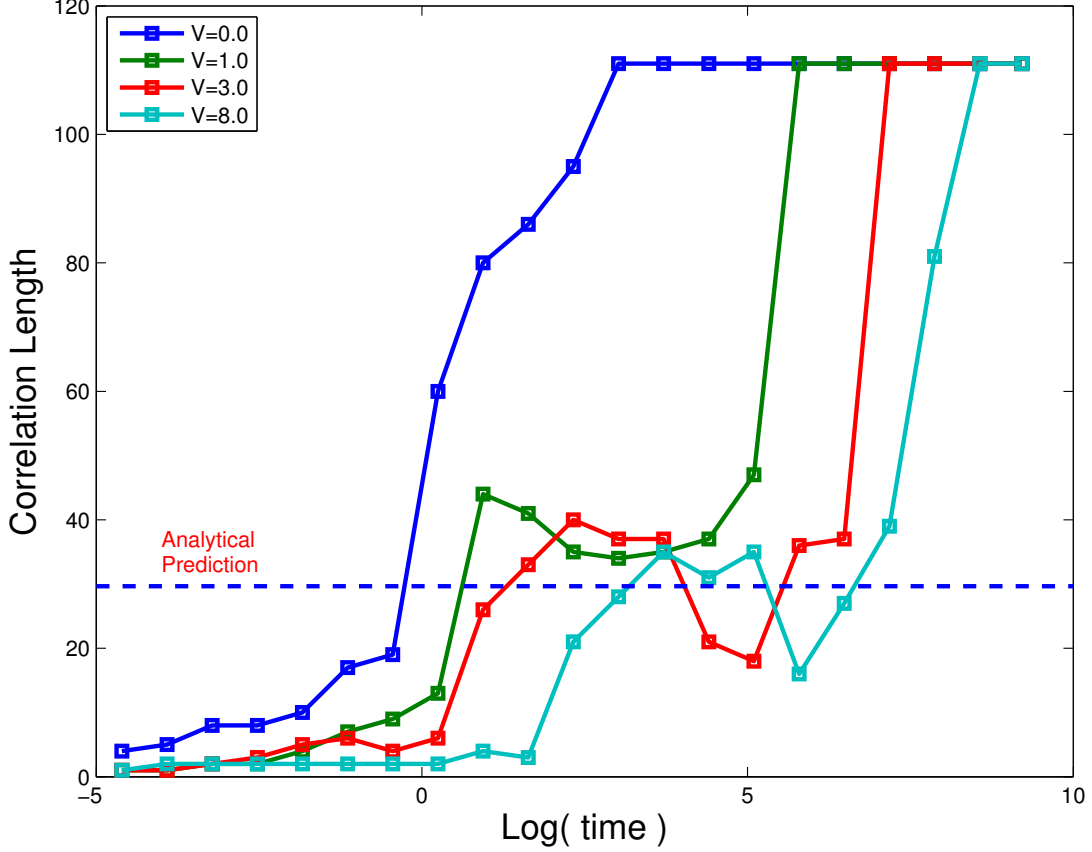
Figure 10: Domain size vs time for 111×111 lattice. Temperature below transition $\delta a = 0.1$ is fixed. $L=3$, legend: LC-elastic coupling coeficient V

the Bessel function $J_0\left(k_{\text{fastest}}r\right)$ which is at 3.83. We solve for r to get the domain size

to get

$$r = 5.4\sqrt{\frac{L}{\delta a}}.$$
(21)

Dependence of coarsening dynamics on temperature

We have tested the domain size given by equation 21 by simulations with different parameters and seen that there is good agreement between theory and simulations. As an example we show the comparison between the predicted analytical value and simulation results in Fig. 10. For $L = 3$ and $\delta a = 0.1$ the analytical prediction for the domain size is approximately 30 which is shown with the horizontal dashed line.

41

Dependence of coarsening dynamics on coupling strength

We pick a fixed $\delta a = 0.1$ and vary the coupling strength V. In this case the growth of domains exhibit different characteristics for different values of the coupling strength V. For $V = 0$, which is pure LC, we see coarsening of domains with no specific domain size, both for short times and long times, while for $V > 0$ the system first evolves towards a characteristic size of periodic domains, the domain boundaries grow sharper and then they grow bigger and combine with neighboring domains to relax to mono-domain. Thus we conclude that pure LCs have continuously growing domains while domains in LCE remains at a characteristic size until S starts saturating and the free energy gets out of the harmonic range. Theory and simulations regarding domain size selection are again in good agreement for all V values. Another point to note is that LC elastomers also eventually reach mono-domain but the process of coarsening happens much faster for pure LCs than for LC elastomers. The bigger the coupling constant the slower the coarsening in the harmonic range. The coupling constants for typical LCEs can be quite large thus it may allow enough time for the material to freeze in the domains while the order parameter is still in the harmonic range.

Non uniformity in material as impurities

In the long time limit, behavior for all of the V values in the above cases is similar. The correlation length grows and reaches the system size. In order to lock in a finite domain size we would like to see the effect of introducing impurities to the LCE. These impurities consist of 2×2 regions in which the elastic coupling is set to a small value, $V = 0.1$, and the L value is kept the same. We repeat simulations with different numbers
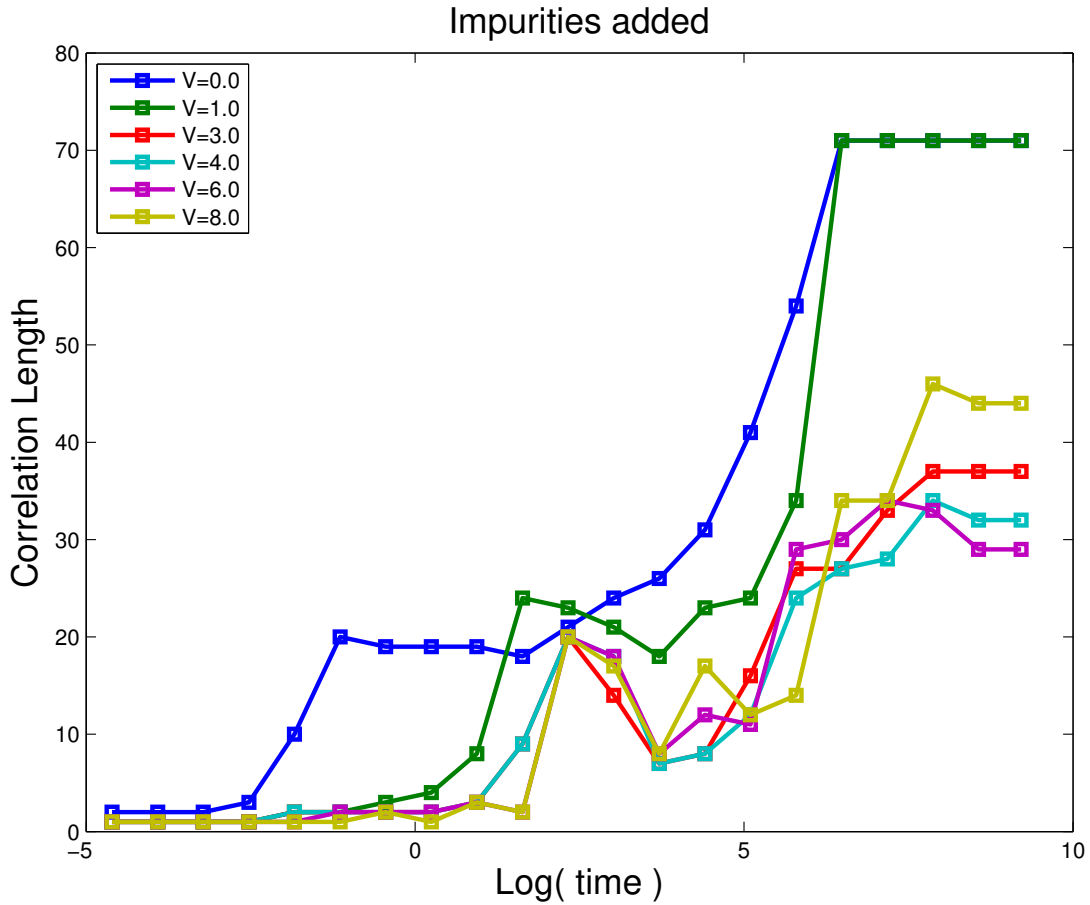
Figure 11: Domain size vs time with impurities for a 71×71 lattice. Temperature below transition $\delta a = 0.1$ is fixed. L=0.3, legend: LC-elastic coupling coefficient V

of impurities. As we add more impurities, we end up with smaller stable domains. This indicates that average distance between impurities act as a limiting size for the domains.

For smaller V values, impurities do not make any difference. This size limiting effect becomes more apparent (see Fig. 11) for bigger V values which also demonstrates the important effect of elastic coupling on the formation of polydomain structures; elastic coupling slows down the growth of domains and they also help lock in the finite size domains in the presence of nonuniformities in V.

As a test we also add impurities in L, the Frank constant, however we do not see any similar effect of impurities.

2.3   Discussion

We have performed analytical calculations using a linear model for energy with two different types of dissipation (linear viscous drags). Both models show that the dynamic mechanism of the isotropic-nematic transition selects a fastest-growing wavevector. This fastest-growing wavevector is not the minimum of the free energy, and it only occurs because of the coupling between nematic order and strain.

We have also run numerical simulations with higher order terms in the free energy. The simulations indicate that the initial selection of a characteristic domain size ceases as the nematic order matures and the free energy escapes the harmonic regime in the order parameter. However inclusion of impurities as variations in the LC-elastic coupling strength can easily lock in the polydomain structure. We should assume that impurities exist in real materials especially while the cross-linking is still in process.

Furthermore the elastic coupling can contribute to the formation of polydomains. Our simulations show that presence of elastic coupling slows down the growth of domains which will allow longer times for the system to freeze-in a permanent preferred direction in each domain. All of these factors make it very hard for the system to reach a monodomain state.

Our theory can be tested experimentally by investigating how the polydomain structure depends on cooling rate. The theory predicts that coarsening farther below the equilibrium isotropic-nematic transition temperature gives a higher wavevector k_{fastest}. Hence, a higher cooling rate should lead to a smaller polydomain length scale. The theory might also be tested by imaging the polydomain structure; we expect a structure characterized by bend

stripes as in Fig. 5.

In conclusion, we have shown that dynamic evolution of nematic order can induce a polydomain state with a characteristic length scale, in the early stages of the isotropic-nematic transition. This mechanism should be considered, along with quenched disorder, in studies of polydomain liquid-crystal elastomers.

BIBLIOGRAPHY

[1] M. Warner and E. M. Terentjev, *Liquid Crystal Elastomers*. Oxford, 2003.

[2] J. Küpfer and H. Finkelmann, "Nematic liquid single crystal elastomers," *Die Makromolekulare Chemie, Rapid Communications*, vol. 12, no. 12, pp. 717–726, 1991.

[3] S. M. Clarke, E. M. Terentjev, I. Kundler, and H. Finkelmann, "Texture evolution during the polydomain-monodomain transition in nematic elastomers," *Macromolecules*, vol. 31, no. 15, pp. 4862–4872, 1998.

[4] F. Elias, S. M. Clarke, R. Peck, and E. M. Terentjev, "Equilibrium textures in main-chain liquid crystalline polymers," *Europhysics Letters*, vol. 47, no. 4, p. 442, 1999.

[5] K. Urayama, "Selected issues in liquid crystal elastomers and gels," *Macromolecules*, vol. 40, no. 7, pp. 2277–2288, 2007.

[6] G. Feio, J. L. Figueirinhas, A. R. Tajbakhsh, and E. M. Terentjev, "Critical fluctuations and random-anisotropy glass transition in nematic elastomers," *Phys. Rev. B*, vol. 78, p. 020201, Jul 2008.

[7] K. Urayama, E. Kohmon, M. Kojima, and T. Takigawa, "Polydomainmonodomain transition of randomly disordered nematic elastomers with different cross-linking histories," *Macromolecules*, vol. 42, no. 12, pp. 4084–4089, 2009.

[8] C. A. Grabowski, P. A. Luchette, and P. Palffy-Muhoray. http://e-lc.org/presentations/tmp/Christopher_A_Grabowski_2011_09_14_20_01_24.pdf, 2011.

[9] S. V. Fridrikh and E. M. Terentjev, "Order-disorder transition in an external field in random ferromagnets and nematic elastomers," *Phys. Rev. Lett.*, vol. 79, pp. 4661–4664, Dec 1997.

[10] S. V. Fridrikh and E. M. Terentjev, "Polydomain-monodomain transition in nematic elastomers," *Phys. Rev. E*, vol. 60, pp. 1847–1857, Aug 1999.

[11] Y.-K. Yu, "Self-consistent approach to a strongly disordered planar model with application to 2d nematic elastomers," *Phys. Rev. Lett.*, vol. 83, pp. 5515–5518, Dec 1999.

[12] X. Xing and L. Radzihovsky, "Universal elasticity and fluctuations of nematic gels," *Phys. Rev. Lett.*, vol. 90, p. 168301, Apr 2003.

[13] L. Petridis and E. M. Terentjev, "Nematic-isotropic transition with quenched disorder," *Phys. Rev. E*, vol. 74, p. 051707, Nov 2006.

[14] X. Xing, S. Pfahl, S. Mukhopadhyay, P. M. Goldbart, and A. Zippelius, "Nematic elastomers: From a microscopic model to macroscopic elasticity theory," *Phys. Rev. E*, vol. 77, p. 051802, May 2008.

[15] B.-S. Lu, F. Ye, X. Xing, and P. M. Goldbart, "Phenomenological theory of isotropic-genesis nematic elastomers," *Phys. Rev. Lett.*, vol. 108, p. 257803, Jun 2012.

[16] X. Xing, B.-S. Lu, F. Ye, and P. M. Goldbart, "Generalized deam-edwards approach to the statistical mechanics of randomly crosslinked systems," *New Journal of Physics*, vol. 15, no. 8, p. 085017, 2013.

[17] B.-S. Lu, F. Ye, X. Xing, and P. M. Goldbart, "Statistical physics of isotropic-genesis nematic elastomers: I. structure and correlations at high temperatures," *International Journal of Modern Physics B*, vol. 27, no. 17, p. 1330012, 2013.

[18] Y.-K. Yu, P. L. Taylor, and E. M. Terentjev, "Exponential decay of correlations in a model for strongly disordered 2d nematic elastomers," *Phys. Rev. Lett.*, vol. 81, pp. 128–131, Jul 1998.

[19] N. Uchida, "Elastic effects in disordered nematic networks," *Phys. Rev. E*, vol. 60, pp. R13–R16, Jul 1999.

[20] N. Uchida, "Soft and nonsoft structural transitions in disordered nematic networks," *Phys. Rev. E*, vol. 62, pp. 5119–5136, Oct 2000.

[21] J. V. Selinger and B. R. Ratna, "Isotropic-nematic transition in liquid-crystalline elastomers: Lattice model with quenched disorder," *Phys. Rev. E*, vol. 70, p. 041707, Oct 2004.

[22] J. S. Biggins, M. Warner, and K. Bhattacharya, "Supersoft elasticity in polydomain nematic elastomers," *Phys. Rev. Lett.*, vol. 103, p. 037802, Jul 2009.

[23] J. Biggins, M. Warner, and K. Bhattacharya, "Elasticity of polydomain liquid crystal elastomers," *Journal of the Mechanics and Physics of Solids*, vol. 60, no. 4, pp. 573 – 590, 2012.

[24] O. Stenull and T. C. Lubensky, "Dynamics of nematic elastomers," *Phys. Rev. E*, vol. 69, p. 051801, May 2004.

[25] M. C. Marchetti, J. F. Joanny, S. Ramaswamy, T. B. Liverpool, J. Prost, M. Rao, and R. A. Simha, "Hydrodynamics of soft active matter," *Rev. Mod. Phys.*, vol. 85, pp. 1143–1189, Jul 2013.

APPENDICES

2.A   Strain tensor calculation from coordinates

We calculate the strain tensor in the lab frame using undeformed and deformed coordinates of a triangle. For a point on the triangle consider a linear deformation that maps the undeformed coordinates (x_0, y_0) to deformed coordinates (x, y). The deformation tensor is given by

$$\Lambda = \begin{pmatrix} \frac{\partial x}{\partial x_0} & \frac{\partial x}{\partial y_0} \\ \frac{\partial y}{\partial x_0} & \frac{\partial y}{\partial y_0} \end{pmatrix}.$$

In order to calculate the above derivatives using the old and new coordinates, we need to determine the $a, b, c,$ coefficients in the equation

$$\begin{pmatrix} x \\ y \end{pmatrix} = \begin{pmatrix} a_1 & b_1 & c_1 \\ a_2 & b_2 & c_2 \end{pmatrix} \begin{pmatrix} 1 \\ x_0 \\ y_0 \end{pmatrix}$$

as the deformation tensor will be

$$\Lambda = \begin{pmatrix} b_1 & c_1 \\ b_2 & c_2 \end{pmatrix}.$$

To solve for these coefficients, we need to include the linear mapping for all three vertices which can be rewritten as a matrix equation as follows.

$$
\begin{pmatrix} x_1 \\ x_2 \\ x_3 \end{pmatrix} = \begin{pmatrix} 1 & x_1^{old} & y_1^{old} \\ 1 & x_2^{old} & y_2^{old} \\ 1 & x_3^{old} & y_3^{old} \end{pmatrix} \begin{pmatrix} a_1 \\ b_1 \\ c_1 \end{pmatrix}
$$

$$
\begin{pmatrix} y_1 \\ y_2 \\ y_3 \end{pmatrix} = \begin{pmatrix} 1 & x_1^{old} & y_1^{old} \\ 1 & x_2^{old} & y_2^{old} \\ 1 & x_3^{old} & y_3^{old} \end{pmatrix} \begin{pmatrix} a_2 \\ b_2 \\ c_2 \end{pmatrix}
$$

The old coordinates come from the vetices of 4 right triangles formed by drawing alternating diagonals in a square lattice. These triangles are 4 rotated versions of the right triangle whose vertices are (0,0), (1,0), and (0,1). A general description for all 4 triangles are these coordinates can be obtained using a rotation angle κ. Now the mapping from undeformed to deformed coordinates is

$$
\begin{pmatrix} 0 & \cos(\kappa) & -\sin(\kappa) \\ 0 & \sin(\kappa) & \cos(\kappa) \end{pmatrix} \Rightarrow \begin{pmatrix} x_1 & x_2 & x_3 \\ y_1 & y_2 & y_3 \end{pmatrix}.
$$

After performing the steps mentioned we solve for the coefficients and get the deformation tensor. The strain tensor can then be obtanined from the deformation tensor Λ using the definition

$$
\epsilon = \frac{1}{2} \left(\Lambda \cdot \Lambda^{\mathsf{T}} - \mathbf{I} \right)
$$

$$
= \begin{pmatrix} \epsilon_{xx} & \epsilon_{xy} \\ \epsilon_{xy} & \epsilon_{yy} \end{pmatrix}
$$

where

$$\epsilon_{xx} = -1 + x_1^2 + x_2^2 + x_3^2 - 2x_1\left(x_2 + x_3 - x_1\right)$$

$$\epsilon_{xy} = x_2\left(y_2 - y_1\right) + x_3\left(y_3 - y_1\right) + x_1\left(2y_1 - y_2 - y_3\right)$$

$$\epsilon_{yy} = -1 + y_1^2 + y_2^2 + y_3^2 - 2y_1\left(y_2 + y_3 - y_1\right)$$

The result is independent from the rotation angle κ thus we can use the above equation to describe the strain tensor for any of the 4 types of triangles. This feature simplifies the calculations in the simulation.

2.B Incompressibility

Consider the deformation of a small rectangular element of width Δx_0 and height Δy_0 along x and y axes only. The deformation relation can be written as

$$
\begin{pmatrix} \Delta x \\ \Delta y \end{pmatrix} = \begin{pmatrix} \Lambda_{11} & 0 \\ 0 & \Lambda_{22} \end{pmatrix} \begin{pmatrix} \Delta x_0 \\ \Delta y_0 \end{pmatrix}
$$

The deformed volume (area) is $\Delta x \Delta y = \Lambda_{11} \Delta x_0 \Lambda_{22} \Delta y_0 = (\Delta x_0 \Delta y_0) \det \overset{\leftrightarrow}{\Lambda}$. The determinant of the deformation tensor relates the volumes of infinitesimal elements in undeformed and deformed states;

$$
\det \overset{\leftrightarrow}{\Lambda} = \frac{V}{V_0}, \tag{22}
$$

which is true in any coordinate system because the determinant is invariant. In order to penalize change of volume, a term such as

$$
\begin{aligned}
\Delta F &= \frac{1}{2}\lambda \left(\frac{\Delta V}{V_0}\right)^2 \\
&= \frac{1}{2}\lambda \left(\det \overset{\leftrightarrow}{\Lambda} - 1\right)^2
\end{aligned} \tag{23}
$$

can be added to the free energy. $\det \overset{\leftrightarrow}{\Lambda} = \sqrt{\det\left(\overset{\leftrightarrow}{\Lambda}\overset{\leftrightarrow}{\Lambda}{}^T\right)}$ and $\overset{\leftrightarrow}{\Lambda}\overset{\leftrightarrow}{\Lambda}{}^T = \overset{\leftrightarrow}{I} + 2\overset{\leftrightarrow}{\epsilon}$, thus this term can be written as

$$
\begin{aligned}
\Delta F &= \frac{1}{2}\lambda \left(\sqrt{\det\left(\overset{\leftrightarrow}{I} + 2\overset{\leftrightarrow}{\epsilon}\right)} - 1\right)^2 \\
&= \frac{1}{2}\lambda \left(\sqrt{(1 + 2\epsilon_{11})(1 + 2\epsilon_{22}) - 4\epsilon_{12}^2} - 1\right)^2 \\
&= \frac{1}{2}\lambda \left(\sqrt{1 + 2\operatorname{Tr}\overset{\leftrightarrow}{\epsilon} + 4\det\overset{\leftrightarrow}{\epsilon}} - 1\right)^2
\end{aligned} \tag{24}
$$

In the limit of small deformation the first order approximation yields

$$
\Delta F \approx \frac{1}{2}\lambda \left(\operatorname{Tr}\overset{\leftrightarrow}{\epsilon} + 2\det\overset{\leftrightarrow}{\epsilon}\right)^2 \tag{25}
$$

51

The first part of Eqn. 25 was used in the analytical calculations. In order to improve the incompressibility of the material in the simulations, we substitute

$$\mathrm{Tr}\,\overset{\leftrightarrow}{\epsilon} \to \mathrm{Tr}\,\overset{\leftrightarrow}{\epsilon} + 2\det\overset{\leftrightarrow}{\epsilon}.$$

2.C Maier-Saupe type calculation of free energy

We would like to calculate the free energy of a liquid crystal system in 2D. The generic expression

$$F = aS^2 + bS^4$$

is a good approximation for values of S that are not too big. However in simulations a better expression is needed in order to keep the value of S below 1.

In the Maier-Saupe model the molecules have nematic interactions with each other and a mean-field approximation is used. Thus we assign an alignment potential of the form $-u \cos 2\theta$ where u is a mean-field average energy and θ is measured from the average director. Let's also define $U = u/k_B T$ to simplify the expressions. With these definitons the probability of having an orientation θ around the average director is given by

$$\rho = \frac{\exp(U \cos 2\theta)}{\int_0^{2\pi} \exp(U \cos 2\theta) d\theta} \tag{26}$$

$$= \frac{\exp(U \cos 2\theta)}{2\pi I_0(U)} \tag{27}$$

where I_0 is the Bessel function of order zero. The nematic order parameter is

$$S = \int_0^{2\pi} \rho \, \exp(U \cos 2\theta) \, d\theta$$

$$= \frac{I_1(U)}{I_0(U)} \tag{28}$$

Since S is used for the order parameter we will use E to denote entropy which can be calculated as

$$\frac{E}{k} = \int_0^{2\pi} \rho \log(\rho) \, d\theta$$

$$= U \frac{I_1(U)}{I_0(U)} - \log\left(2\pi I_0(U)\right)$$
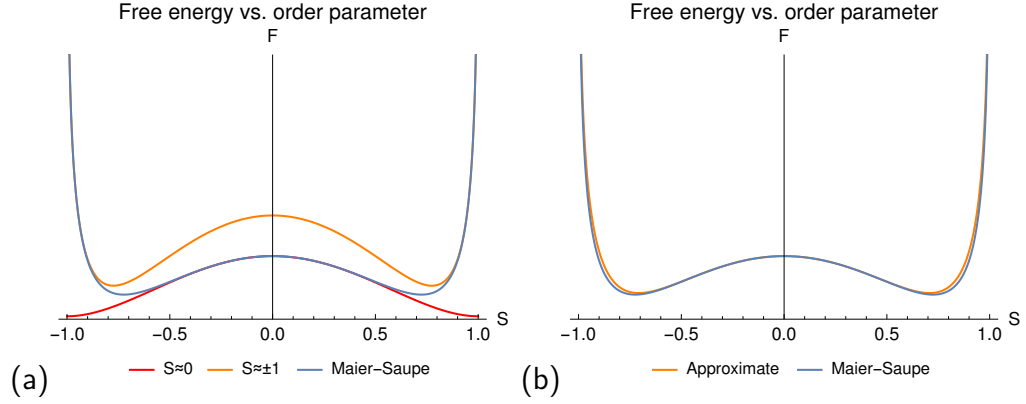
Figure 12: Approximate free energy expressions derived from a Maier-Saupe style calculation. The blue curve shows the parametric plot of the actual calculation in terms of U. (a) Expansions of the parametric equation in terms of order parameter S near $S = 0$ and $S = \pm 1$. (b) Unified equation which agrees perfectly with the parametric equation for both $S = 0$ and $S = \pm 1$ limits but slightly off for intermediate values of S.

The free energy is then

$$
\begin{aligned}
F &= -\frac{1}{2}JS^2 - TE \\
&= -\frac{1}{2}J\left(\frac{I_1(U)}{I_0(U)}\right)^2 - kT\left[U\frac{I_1(U)}{I_0(U)} - \log\left(2\pi I_0(U)\right)\right]
\end{aligned}
$$

Next we would like to express the latter in terms of the order parameter S. We cannot

solve for U in equation 28 but we can substitute a Taylor series to get an approximate

solution in two separate limits where $S \approx 0$ and $S \approx \pm 1$.

$$
U \approx
\begin{cases}
2S + S^3 & if \quad S \approx 0 \\[2ex]
\frac{1}{1-S^2} + \frac{1-S^2}{8} & if \quad S \approx \pm 1
\end{cases}
$$

We substitute U in the free energy equation and get

$$
\frac{F}{kT} \approx
\begin{cases}
(1 - \frac{J}{2kT})S^2 + \frac{S^4}{4} - \log[2\pi] & if \quad S \approx 0 \\[2ex]
-\frac{3}{4} + \left(\frac{1}{4} - \frac{J}{2kT}\right)S^2 - \frac{1}{2}\log(2\pi) - \frac{1}{2}\log(1 - S^2) & if \quad S \approx \pm 1
\end{cases}
$$

The two parts of the piecewise free energy function are very good approximations to the free energy at low and high order limits but each one is good at only one of the limits (see Fig. 12-a). However it's possible to get a unified function which agrees with the parametric equation at both limits, i.e. around $S = 0$ and $S = \pm 1$. This unified function which reads

$$\frac{F}{kT} = -\log(2\pi) + \left(\frac{1}{2} - \frac{J}{2kT}\right) S^2 - \frac{1}{2}\log\left(1 - S^2\right)$$

and the parametric functions are plotted in Fig. 12-b. Our goal here is to improve the approximate free energy expression $F \approx aS^2 + bS^4$ so that, $\lim_{S \to \pm 1} F = \infty$ to keep S from growing too much and exceeding 1. We can rewrite the free energy above as

$$\frac{F}{kT} + \log(2\pi) = \left(1 - \frac{J}{2kT}\right) S^2 - \frac{1}{2}\left(S^2 + \log\left[1 - S^2\right]\right).$$

The small S limit of this expression is to be $aS^2 + bS^4$ so the final form of the free energy can be written as

$$\mathcal{F} = aS^2 - 2b\left(S^2 + \log\left[1 - S^2\right]\right). \tag{29}$$

CHAPTER 3

Active Brownian particles near straight or curved walls: Pressure and boundary

layers

3.1 Introduction

The statistical properties of active particles are quite different from the analogous properties of passive particles [1, 2]. For example, by the conventional laws of thermodynamics, equilibrium Brownian motion cannot perform any useful work. By contrast, active Brownian motion has been shown to power microscopic gears, thus performing mechanical work [3–5]. This behavior can be attributed to a distinctive feature seen in experiments that self propelled particles accumulate at the walls [6]. Similarly, active Brownian particles drive the motion of curved tracers [7], and induce flexible membranes to fold [8]. Parallel plates immersed in a bath of active Brownian particles experience an attractive depletion force, analogous to the Casimir effect, unlike plates in a bath of equilibrium Brownian particles [9]. A bath of active particles exerts an active pressure on the walls, which is not a state function of the fluid but rather depends on properties of the walls [10], particularly on the wall curvature [11–13].

The purpose of this chapter is to explore how systems cross over from equilibrium to active behavior, as a function of particle activity, through several example calculations. First, in Secs. 3.2 and 3.3, we review the derivation of equations of motion for order parameter fields in a system of active particles, and use these equations to calculate the

steady-state solutions in several specific geometries: near a straight wall, between two straight walls, inside and outside a circular wall. These calculations show the formation of boundary layers near the walls, which are characterized by enhancements in the density and polar order. (Most of these calculations are done by truncating a series of equations for moments of the density distribution, but Appendix 3.A shows that some results apply even without this truncation.) We note that Ref. [14, 15] also use moment equations to derive density profiles near boundaries. Here we first derive similar results and run simulations for comparison. Next, we make appropriate approximations and further apply these results to calculate forces and densities in various systems(Sec. 3.5).

In Sec. 3.4, we find a simple relationship between the density enhancement in the boundary layer and the active pressure on a wall. Through this relationship, we determine the pressure on a straight wall, as well as inside and outside a circular wall. We combine these calculations into a single curvature-dependent active pressure. This result is consistent with previous results by other investigators, but obtained through a different method.

In Sec. 3.5, we apply these findings to specific geometries that demonstrate important differences between equilibrium and active systems. For a pair of parallel plates in a bath of active Brownian particles, we use boundary-layer considerations to estimate the Casimir-like depletion force between the plates. For a curved tracer in an active bath, we find the net force resulting from the different pressures on the inner and outer surfaces. Finally, for a circular particle corral with just a small opening, we show that particle activity leads to a difference in densities between inside and outside.

3.2 Theoretical formalism

We begin by reviewing the derivation of equations of motion for a system of active Brownian particles, beginning with Langevin dynamics for individual particles and leading up to equations for order parameter fields that can be solved in arbitrary geometries.

We consider a system of active, non-interacting Brownian particles in two dimensions (2D). We suppose that each particle has a position $\boldsymbol{r} = (x, y)$ and an orientation $\hat{\boldsymbol{n}} = (\cos\theta, \sin\theta)$ for its self-propulsive force. Apart from this self-propulsive force, the particles are isotropic. To describe the time evolution of the position and orientation, we use Langevin stochastic dynamics in the overdamped limit, which gives

$$\frac{d\boldsymbol{r}}{dt} = \beta D_t \left[F\hat{\boldsymbol{n}} - \boldsymbol{\nabla}U(\boldsymbol{r}) + \boldsymbol{f}(t) \right], \tag{30a}$$

$$\frac{d\theta}{dt} = \beta D_r \left[g(t) \right]. \tag{30b}$$

Here, D_t and D_r are the translational and rotational diffusion constants, respectively, and $\beta = 1/(k_B T)$ is the inverse temperature. The coefficient F is the self-propulsive force of each particle, and the product $v_0 = \beta D_t F$ is the self-propulsive velocity. The function $U(\boldsymbol{r})$ is the potential energy, so that $-\boldsymbol{\nabla}U(\boldsymbol{r})$ is the force derived from the potential. The final terms $\boldsymbol{f}(t)$ and $g(t)$ are the random force and torque acting on each particle. These stochastic contributions satisfy Gaussian white noise statistics, such that

$$\langle f_i(t) \rangle = 0, \quad \langle g(t) \rangle = 0,$$

$$\langle f_i(t)f_j(t') \rangle = \frac{2\delta_{ij}\delta(t-t')}{\beta^2 D_t}, \quad \langle g(t)g(t') \rangle = \frac{2\delta(t-t')}{\beta^2 D_r},$$

$$\langle f_i(t)g(t') \rangle = 0. \tag{31}$$

To characterize a large ensemble of active Brownian particles, we use the probability

distribution function $P(\boldsymbol{r}, \theta, t)$, which gives the probability of finding a particle at position $\boldsymbol{r}$ with orientation θ at time t. This distribution function evolves in time following the Smoluchowski equation

$$
\begin{aligned}
\frac{\partial P}{\partial t} = & - \frac{\partial}{\partial r_i}\left[\frac{\langle \Delta r_i \rangle}{\Delta t}P\right] - \frac{\partial}{\partial \theta}\left[\frac{\langle \Delta \theta \rangle}{\Delta t}P\right] \\
& + \frac{1}{2}\frac{\partial^2}{\partial r_i \partial r_j}\left[\frac{\langle \Delta r_i \Delta r_j \rangle}{\Delta t}P\right] + \frac{1}{2}\frac{\partial^2}{\partial \theta^2}\left[\frac{\langle \Delta \theta^2 \rangle}{\Delta t}P\right] \\
& + \frac{\partial^2}{\partial r_i \partial \theta}\left[\frac{\langle \Delta r_i \Delta \theta \rangle}{\Delta t}P\right].
\end{aligned}
\tag{32}
$$

Here, the quantities in angle brackets are averages calculated over all particles at position $\boldsymbol{r}$ with orientation θ during a small time interval from t to $t + \Delta t$. In our system, direct integration of the Langevin equations gives

$$
\langle \Delta r_i \rangle = (v_0 n_i - \beta D_t \partial_i U)\Delta t, \quad \langle \Delta \theta \rangle = 0,
$$

$$
\langle \Delta r_i \Delta r_j \rangle = 2D_t \delta_{ij}\Delta t, \quad \langle \Delta \theta^2 \rangle = 2D_r \Delta t,
$$

$$
\langle \Delta r_i \Delta \theta \rangle = 0.
\tag{33}
$$

With those expectation values, the Smoluchowski equation becomes

$$
\begin{aligned}
\frac{\partial P}{\partial t} = & - \boldsymbol{\nabla} \cdot [(v_0 \hat{\boldsymbol{n}} - \beta D_t \boldsymbol{\nabla} U)P + D_t \boldsymbol{\nabla} P] + D_r \frac{\partial^2 P}{\partial \theta^2} \\
= & - \boldsymbol{\nabla} \cdot \boldsymbol{J} + D_r \frac{\partial^2 P}{\partial \theta^2},
\end{aligned}
\tag{34}
$$

where $\boldsymbol{J}(\boldsymbol{r}, \theta, t) = (v_0 \hat{\boldsymbol{n}} - \beta D_t \boldsymbol{\nabla} U)P + D_t \boldsymbol{\nabla} P$ is the current density of particles at position $\boldsymbol{r}$ with orientation θ at time t.

As a simplification, instead of considering the full distribution $P(\boldsymbol{r}, \theta, t)$ as a function

of θ, we calculate orientational moments of the distribution

$$\rho(\boldsymbol{r}, t) = \int_0^{2\pi} P(\boldsymbol{r}, \theta, t) d\theta, \tag{35a}$$

$$M_i(\boldsymbol{r}, t) = \int_0^{2\pi} P(\boldsymbol{r}, \theta, t) n_i d\theta, \tag{35b}$$

$$Q_{ij}(\boldsymbol{r}, t) = \int_0^{2\pi} P(\boldsymbol{r}, \theta, t) \left(2 n_i n_j - \delta_{ij} \right) d\theta, \tag{35c}$$

with $n_1 = \cos\theta$ and $n_2 = \sin\theta$. The zero-th moment $\rho(\boldsymbol{r}, t)$ is the total density of particles, integrated over all orientations, as a function of positition and time. The higher moments (normalized by ρ) give the orientational order parameters as functions of position and time. In particular, the vector $\boldsymbol{M}(\boldsymbol{r}, t)/\rho(\boldsymbol{r}, t)$ is the polar order parameter, and the tensor $\boldsymbol{Q}(\boldsymbol{r}, t)/\rho(\boldsymbol{r}, t)$ is the nematic order parameter. By integrating over the Smoluchowski equation (34), we obtain equations of motion for the moments

$$\begin{aligned}
\frac{\partial \rho}{\partial t} &= - \partial_i \left[v_0 M_i - \beta D_t (\partial_i U) \rho - D_t \partial_i \rho \right] \\
&= - \partial_i J_i^{(0)}, \tag{36a}
\end{aligned}$$

$$\begin{aligned}
\frac{\partial M_j}{\partial t} &= - \partial_i \left[\tfrac{1}{2} v_0 (\rho \delta_{ij} + Q_{ij}) - \beta D_t (\partial_i U) M_j - D_t \partial_i M_j \right] \\
&\quad - D_r M_j \\
&= - \partial_i J_{ij}^{(1)} - D_r M_j. \tag{36b}
\end{aligned}$$

Here, the moments of current density are defined as $J_i^{(0)}(\boldsymbol{r}, t) = \int_0^{2\pi} J_i(\boldsymbol{r}, \theta, t) d\theta$ and $J_{ij}^{(1)}(\boldsymbol{r}, t) = \int_0^{2\pi} J_i(\boldsymbol{r}, \theta, t) n_j d\theta$.

In principle, there is an infinite series of equations of motion for the moments, with the equation for the dipole moment M_i depending on the quadrupole moment Q_{ij}, the equation for the quadrupole moment depending on the octupole moment, and so forth. As an approximation, we truncate the series by assuming that the quadrupole moment

$Q_{ij} = 0$. With that approximation, Eqs. (36) provide a closed set of equations for $\rho(\boldsymbol{r}, t)$ and $M_i(\boldsymbol{r}, t)$, which can be solved to find the distribution of active Brownian particles in any geometry.

3.3 Solution in simple geometries

In this section, we find steady-state solutions of the Smoluchowski moment equations (36) in several specific geometries with straight or curved walls. We consider hard walls, so that the potential energy can be written as

$$U(\boldsymbol{r}) = \begin{cases} 0, & \text{outside wall}, \\ \\ \infty, & \text{inside wall}. \end{cases} \tag{37}$$

In the free space outside the wall where $U(\boldsymbol{r}) = 0$, in the steady state, the Smoluchowski moment equations simplify to

$$0 = -v_0 \boldsymbol{\nabla} \cdot \boldsymbol{M} + D_t \nabla^2 \rho, \tag{38a}$$

$$0 = -\tfrac{1}{2} v_0 \boldsymbol{\nabla} \rho + \nabla^2 \boldsymbol{M} - D_r \boldsymbol{M}. \tag{38b}$$

These equations can be combined to give

$$\nabla^4 \rho = \left(\frac{D_r}{D_t} + \frac{v_0^2}{2D_t^2} \right) \nabla^2 \rho = \xi^{-2} \nabla^2 \rho. \tag{39}$$

Hence, we see that the equation has a natural length scale ξ, which can be written as

$$\xi = \frac{\sqrt{D_t/D_r}}{\sqrt{1 + v_0^2/(2D_r D_t)}} = \frac{a}{\sqrt{1 + \tfrac{1}{2}\text{Pe}^2}}. \tag{40}$$

In the numerator, the ratio of translational and rotational diffusion constants gives the length scale $a = \sqrt{D_t/D_r}$, which is typically of the same order as the particle diameter.

The denominator is expressed in terms of the Peclet number $\text{Pe} = v_0/\sqrt{D_t D_r}$, which is a dimensionless ratio that characterizes the particle activity.

The differential equations must be solved with boundary conditions expressing the constraint that particles cannot enter the hard wall. These boundary conditions can be written in terms of the moments of current density as

$$0 = \hat{\boldsymbol{N}} \cdot \boldsymbol{J}^{(0)} = \hat{\boldsymbol{N}} \cdot (v_0 \boldsymbol{M} - D_t \boldsymbol{\nabla} \rho), \tag{41a}$$

$$0 = \hat{\boldsymbol{N}} \cdot \boldsymbol{J}^{(1)} = \hat{\boldsymbol{N}} \cdot (\tfrac{1}{2} v_0 \rho \boldsymbol{I} - D_t \boldsymbol{\nabla} \boldsymbol{M}), \tag{41b}$$

where $\hat{\boldsymbol{N}}$ is the local normal to the wall. This system of equations can be solved exactly in several cases.

3.3.1 Particles near an infinite straight wall

Consider an infinite, straight wall along the y-axis, so that the region $x < 0$ is free space, and $x > 0$ is excluded. By the symmetry of this problem, we assume that ρ and M_x are functions of x only, and $M_y = 0$. Using these assumptions, we solve the differential equations (38) with the boundary conditions (41), and the additional boundary condition that $\rho(x) \to \rho_{\text{bulk}}$ as $x \to -\infty$. The solution is

$$\rho(x) = \rho_{\text{bulk}} \left(1 + \frac{v_0^2}{2 D_r D_t} e^{x/\xi} \right), \tag{42a}$$

$$M(x) = \frac{\rho_{\text{bulk}} v_0}{2 D_r \xi} e^{x/\xi}. \tag{42b}$$

This solution is plotted in Fig. 13 for three sample sets of parameters. The density $\rho(x)$ is enhanced in a boundary layer of thickness ξ near the wall, and decays exponentially to ρ_{bulk}. The maximum density occurs right at the wall, where

$$\rho_{\text{wall}} = \rho_{\text{bulk}} \left(1 + \frac{v_0^2}{2 D_r D_t} \right). \tag{43}$$

62

In the Appendix (3.A), we will show that this result is exact, and does not depend on the truncation of moments.

The first moment $M_x(x)$ is nonzero in the same boundary layer, and decays exponentially to zero. Because $M_x(x)$ is positive, we can see that particles accumulate at the wall with their orientations pointing into the wall, but are unable to enter the wall. The orientational order parameter

$$M_x(x)/\rho(x) = \frac{v_0}{2D_r\xi} \frac{1}{\left(e^{-x/\xi} + \frac{v_0^2}{2D_r D_t}\right)},$$

is greatest at the wall, and decays exponentially into the bulk, which is isotropic.

As a numerical check on the calculation, we perform simulations of the Langevin equations (30) with a boundary at $x = 0$, and histograms of the density $\rho(x)$ and first moment $M_x(x)$ are plotted in Fig. 13. The numerical results agree very well with the analytic predictions.

3.3.2 Particles between two walls

Now consider a system with two infinite, parallel walls at $x = \pm L$. We solve the differential equations (38) with the boundary conditions (41) on both walls. The solution is

$$\rho(x) = \rho_1 \left[1 + \frac{v_0^2}{2D_r D_t} \frac{\cosh(x/\xi)}{\cosh(L/\xi)}\right], \tag{44a}$$

$$M_x(x) = \frac{\rho_1 v_0}{2D_r\xi} \frac{\sinh(x/\xi)}{\cosh(L/\xi)}, \tag{44b}$$

with an overall coefficient ρ_1. This solution is plotted in Fig. 14. Here, the density $\rho(x)$ has boundary layers of thickness ξ near both walls, and the first moment $M_x(x)$ points into each of the walls.

63
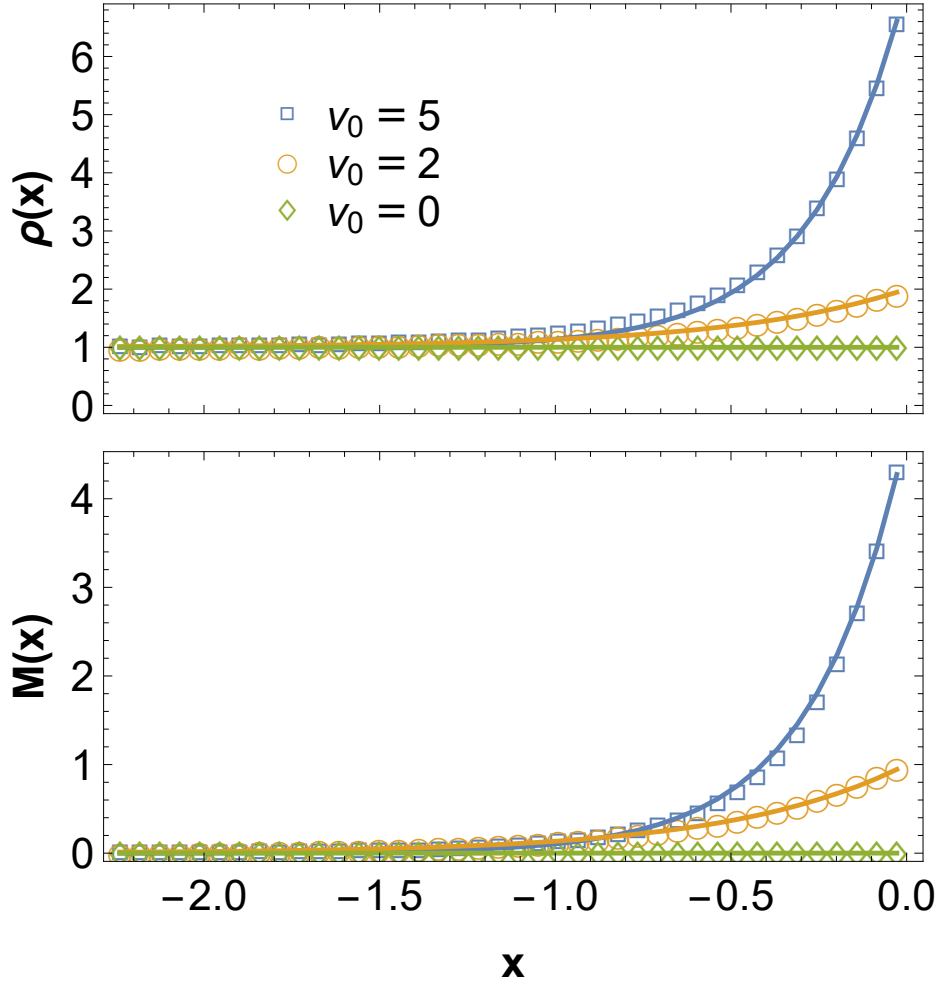
Figure 13: Plots of the density $\rho(x)$ and first moment $M_x(x)$ as functions of position x near a hard wall for $\rho_{\mathsf{bulk}} = 1$. Lines are the analytic predictions of Eqs. (42), and symbols are numerical results from simulations of Langevin dynamics. Activity is $v_0 = 0$ (green diamonds), $v_0 = 2$ (orange circles), and $v_0 = 5$ (blue squares), and other parameters are $D_r = 2$, $D_t = 1$, and $\beta = 1$. All quantities are in arbitrary units.
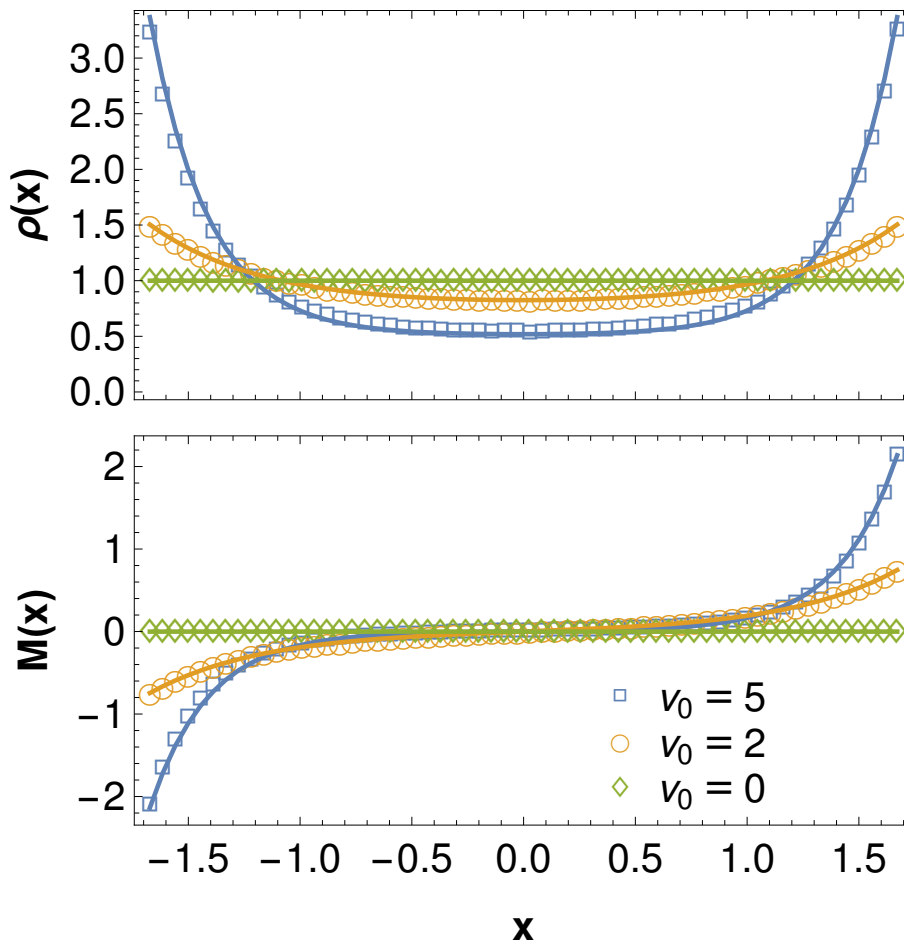
Figure 14: Plots of the density $\rho(x)$ and first moment $M_x(x)$ as functions of position x between two hard walls for $\bar{\rho} = 1$. Lines are the analytic predictions of Eqs. (44–45), and symbols are numerical simulation results. Parameters are the same as in Fig. 13, and all quantities are in arbitrary units.

Instead of a constraint on the density far from the wall, we now have a constraint on the integrated number of particles in the system, which can be written as $\int_{-L}^{L} \rho(x)dx = 2L\bar{\rho}$, where $\bar{\rho}$ is the average density. Hence, the overall coefficient is

$$\rho_1 = \bar{\rho}\left[1 + \frac{v_0^2\xi}{2D_rD_tL}\tanh\left(\frac{L}{\xi}\right)\right]^{-1}. \tag{45}$$

For large wall separation, with $L \gg \xi[1 + v_0^2/(2D_rD_t)]$, the density in the center is approximately independent of the walls, and we can just write the overall coefficient as $\rho_1 = \rho_{\text{bulk}}$. However, for smaller wall separation, the density in the center is depleted because the density on the walls is enhanced, as shown in the figure.

We perform numerical simulations of the Langevin equations with boundaries on both side of the domain. The numerical results, plotted in Fig. 14, agree very well with the analytic predictions.

3.3.3 Particles inside circle

Suppose that active particles are confined inside a hard, circular wall of radius R (Fig. 15-a). In this case, it is most convenient to work in terms of polar coordinates (r, θ). By rotational symmetry, we expect that ρ and M_r are functions of r only, and $M_\theta = 0$. We then express the differential equations (38) in terms of polar coordinates. A general solution for $\rho(r)$ is a linear combination of the modified Bessel functions $I_0(r/\xi)$ and $K_0(r/\xi)$, and the corresponding solution for $M_r(r)$ is a linear combination of $I_1(r/\xi)$ and $K_1(r/\xi)$. Because the density must be finite at $r = 0$, $\rho(r)$ can have only the $I_0(r/\xi)$ function, and hence $M_r(r)$ can have only $I_1(r/\xi)$. By putting these functions into the

boundary conditions (41), expressed in polar coordinates, we obtain

$$\rho(r) = \rho_2 \left[1 + \frac{v_0^2}{D_r D_t} \frac{I_0(r/\xi)}{A_2} \right], \tag{46a}$$

$$M_r(r) = \frac{\rho_2 v_0}{D_r \xi} \frac{I_1(r/\xi)}{A_2}, \tag{46b}$$

with the denominator

$$A_2 = \left(1 + \frac{v_0^2}{2D_r D_t} \right) I_2 \left(\frac{R}{\xi} \right) + \left(1 - \frac{v_0^2}{2D_r D_t} \right) I_0 \left(\frac{R}{\xi} \right), \tag{46c}$$

and with an overall coefficient ρ_2. This solution for density $\rho(r)$ shows a boundary layer

of thickness ξ inside the circular wall. The first moment $M_x(x)$ points outward from the

center, into the circular wall.

As in the previous case, the overall coefficient ρ_2 is fixed by the constraint on the

integrated number of particles in the system, $\int_0^R 2\pi r \rho(r) dr = \pi R^2 \bar{\rho}$, which gives

$$\rho_2 = \bar{\rho} \left[1 + \frac{2v_0^2 \xi I_1(R/\xi)}{D_r D_t R A_2} \right]^{-1}. \tag{47}$$

For a large circle, with $R \gg \xi[1 + v_0^2/(2D_r D_t)]$, the density in the center is approximately

independent of the wall, and we can write the overall coefficient as $\rho_2 = \rho_{\text{bulk}}$. However,

for smaller radius, the density in the center is depleted because the density at the wall is

enhanced.

3.3.4   Particles outside circle

As a modification of the previous case, consider active particles that are confined

outside a hard, circular wall of radius R (Fig. 15-b). Again, we work in polar coordinates

and express the solution in terms of modified Bessel functions. Now the density must be

finite, with $\rho(r) \to \rho_{\text{bulk}}$, as $r \to \infty$. Hence, $\rho(r)$ can include only the $K_0(r/\xi)$ function,
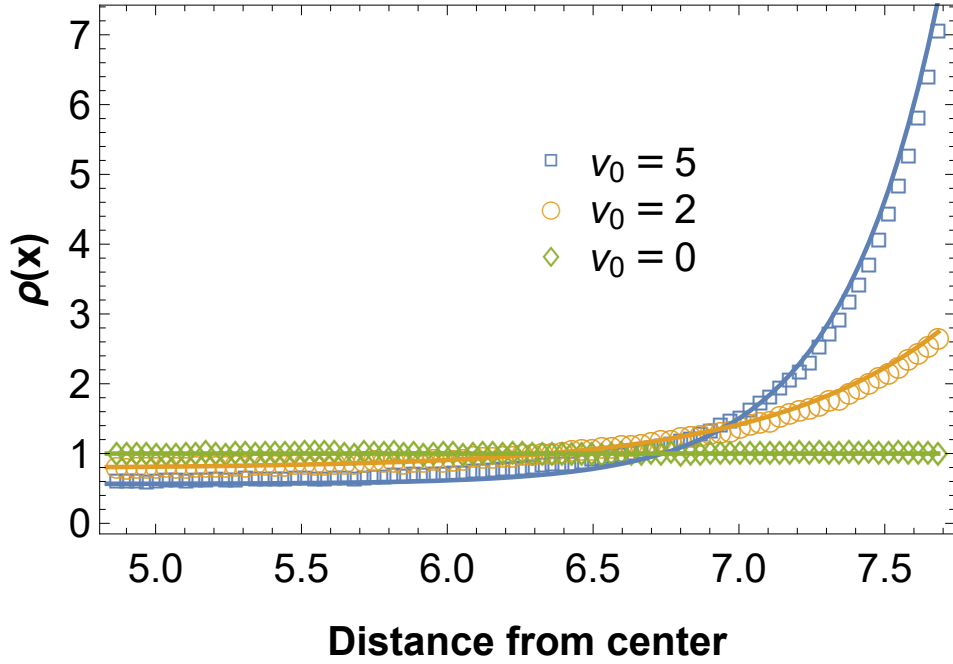
(a) Particles inside a circular wall at $R = 7.7$ for average density $\bar{\rho} = 1$
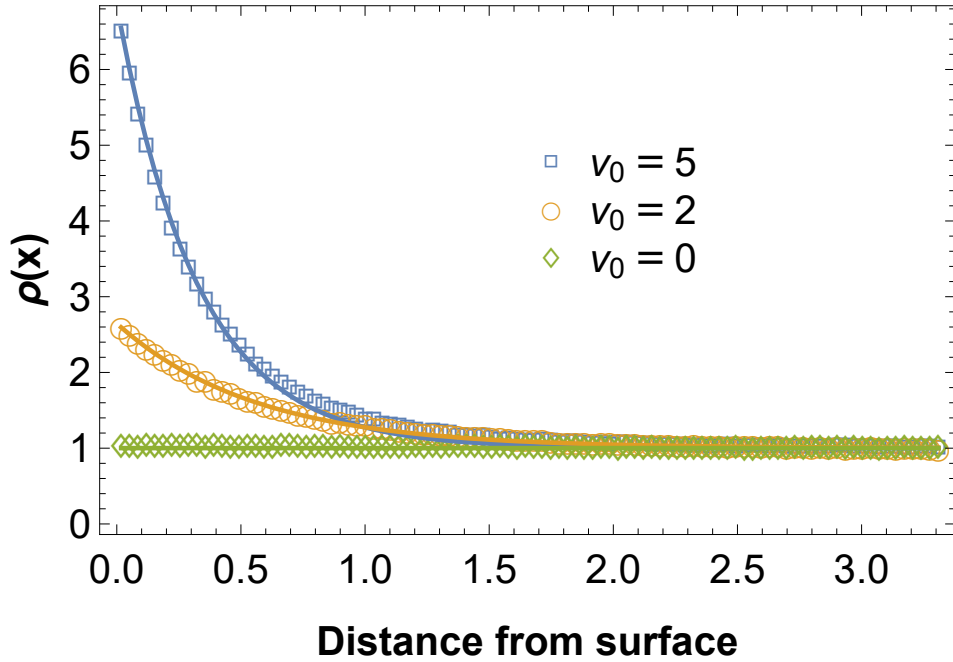
(b) Particles outside a circular wall with $R = 8.3$ for $\rho_{\text{bulk}} = 1$

Figure 15: Plots of the density $\rho(x)$ inside and outside a hard circular wall as functions of position. Lines are the analytic predictions of Eqs. (46-a,48-b), and symbols are numerical results from simulations of Langevin dynamics. Activity is $v_0 = 0$ (green diamonds), $v_0 = 2$ (orange circles), and $v_0 = 5$ (blue squares), and other parameters are $D_r = 1$, $D_t = 1$, and $\beta = 1$. All quantities are in arbitrary units.

and $M_r(r)$ can include only $K_1(r/\xi)$. From the boundary conditions on the circular wall, the solution becomes

$$\rho(r) = \rho_{\text{bulk}} \left[1 + \frac{v_0^2}{D_r D_t} \frac{K_0(r/\xi)}{A_3} \right], \tag{48a}$$

$$M_r(r) = -\frac{\rho_{\text{bulk}} v_0}{D_r \xi} \frac{K_1(r/\xi)}{A_3}, \tag{48b}$$

with the denominator

$$A_3 = \left(1 + \frac{v_0^2}{2D_r D_t} \right) K_2 \left(\frac{R}{\xi} \right) + \left(1 - \frac{v_0^2}{2D_r D_t} \right) K_0 \left(\frac{R}{\xi} \right). \tag{48c}$$

In this solution, the density $\rho(r)$ has a boundary layer of thickness ξ outside the circular wall. The first moment $M_x(x)$ points in toward the center, into the circular wall.

3.4 Pressure on straight or curved walls

In the previous section, we calculated the enhancement of density in boundary layers along hard walls of different shapes: straight, inside a circle, and outside a circle. In addition to the density enhancement, we would also like to calculate the pressure of active particles against each of these walls. To calculate the pressure, we use a method based on the theory of Solon *et al.* [10], and consider a hard wall to be the limiting case of a soft wall.

As a first step, consider an infinite straight wall along the y-axis. Instead of the hard wall potential energy of Eq. (37), we use the soft potential

$$U(x) = \begin{cases} 0, & \text{for } x < 0, \\ U'x, & \text{for } x > 0, \end{cases} \tag{49}$$

where U' is a finite positive constant. The limit of $U' \to \infty$ will then represent a hard

wall. This assumption is similar to Ref. [10], except that we use a linear potential while they used a quadratic potential.

We now solve the steady-state differential equations (36) separately in the regions $x < 0$ and $x > 0$. In each region, we look for solutions where the density $\rho(x)$ and the first moment $M_x(x)$ vary as $e^{\alpha x}$. The differential equations then give a characteristic equation for α. In the region $x < 0$, the characteristic equation is

$$\alpha^3 - \left(\frac{D_r}{D_t} + \frac{v_0^2}{2D_t^2} \right) \alpha = 0, \tag{50}$$

and the solutions are $\alpha = 0$ or $\pm 1/\xi$. In the region $x > 0$, the characteristic equation is

$$\alpha^3 + 2\beta U' \alpha^2 - \left(\frac{D_r}{D_t} + \frac{v_0^2}{2D_t^2} - \beta^2 U'^2 \right) \alpha - \frac{D_r \beta U'}{D_t} = 0. \tag{51}$$

For large U', the solutions are

$$\alpha = \frac{D_r}{\beta U' D_t} + O\left(U'^{-2}\right) \text{ or } -\beta U' \pm \frac{v_0}{\sqrt{2D_t}} + O\left(U'^{-1}\right). \tag{52}$$

Because ρ cannot diverge as $x \to \pm\infty$, we must eliminate the negative value of α for $x < 0$, and the positive value of α for $x > 0$. We then have four exponential modes with coefficients to be determined from the boundary conditions. At the boundary $x = 0$, we require that the density $\rho(x)$, the first moment $M_x(x)$, and the current moments $J_x^{(0)}(x)$ and $J_{xx}^{(1)}(x)$ must all be continuous (keeping in mind that the definition of current moments in Eqs. (36) includes U' terms in the region $x > 0$). We also require that $\rho(x) \to \rho_{\text{bulk}}$ as $x \to -\infty$, far from the wall. Applying these boundary conditions, and assuming that $\beta U' D_t / v_0 \gg 1$, we obtain

$$\rho(x) = \begin{cases} \rho_{\text{bulk}} \left(1 + \frac{v_0^2}{2D_r D_t} e^{x/\xi} \right), & \text{for } x < 0, \\[2ex] \rho_{\text{bulk}} \left(1 + \frac{v_0^2}{2D_r D_t} \right) e^{-\beta U' x}, & \text{for } x > 0. \end{cases} \tag{53}$$

The result for $x < 0$ is exactly the same as previously calculated for a hard wall in Eq. (42a). The result for $x > 0$ shows how the density decreases inside the wall, dominated by the Boltzmann distribution for large U'.

From these results, we can calculate the pressure of the particles on the wall. As noted in Ref. [10], the force of the particles on the wall is equal and opposite to the force of the wall on the particles. Hence, the pressure can be calculated as

$$p = \int_0^\infty \rho(x) \frac{\partial U(x)}{\partial x} dx = U' \int_0^\infty \rho(x) dx \tag{54}$$
$$= \frac{\rho_{\text{bulk}}}{\beta} \left(1 + \frac{v_0^2}{2 D_r D_t}\right) = \rho_{\text{bulk}} k_B T \left(1 + \frac{v_0^2}{2 D_r D_t}\right).$$

This result is consistent with Ref. [10]. In Eq. (54), the first term is the pressure of an ideal gas without activity, $p_{\text{ideal}} = \rho_{\text{bulk}} k_B T$. The second term is an enhancement due to the active velocity v_0. Hence, the active pressure is enhanced over the ideal gas pressure by a factor of $(1 + v_0^2/(2 D_r D_t))$. By comparison, Eq. (53) shows that the density at the wall is enhanced over the bulk density by the same factor $\rho_{\text{wall}} = \rho(0) = \rho_{\text{bulk}}(1 + v_0^2/(2 D_r D_t))$. Hence, the active pressure is simply related to the enhanced density at the wall by $p = \rho_{\text{wall}} k_B T$.

This relationship between pressure and enhanced density at the wall is quite general: If we only assume that the wall potential $U(x)$ is large, diverging as $x \to \infty$, so that the density inside the wall is dominated by the Boltzmann distribution $\rho(x) = \rho_{\text{wall}} e^{-\beta U(x)}$, then the pressure becomes

$$p = \int_0^\infty \rho(x) \frac{\partial U(x)}{\partial x} dx = \rho_{\text{wall}} \int_0^\infty e^{-\beta U(x)} \frac{\partial U(x)}{\partial x} dx$$
$$= \rho_{\text{wall}} \int_0^{U(\infty)} e^{-\beta U} dU = \frac{\rho_{\text{wall}}}{\beta} = \rho_{\text{wall}} k_B T. \tag{55}$$

Now we apply the same considerations to active particles inside or outside a circular wall. For particles inside a circle, the density profile $\rho(r)$ is given by Eq. (46a), with the denominator A_2 defined in Eq. (46c). Suppose the radius R is large enough that the coefficient ρ_2 can be approximated by ρ_{bulk}. The density ρ_{wall} is just the value of $\rho(r)$ at $r = R$, and hence the pressure on the wall is

$$p = \rho_{\text{bulk}} k_B T \left[1 + \frac{\frac{v_0^2}{D_r D_t}}{1 - \frac{v_0^2}{2 D_r D_t} + \left(1 + \frac{v_0^2}{2 D_r D_t} \right) \frac{I_2(R/\xi)}{I_0(R/\xi)}} \right]. \tag{56}$$

For $R \gg \xi$, we can use the asymptotic expansion $I_2(x)/I_0(x) \approx 1 - 2x^{-1} + x^{-2}$ to obtain

$$p = \rho_{\text{bulk}} k_B T \left[1 + \frac{v_0^2}{2 D_r D_t} + \frac{v_0^2}{2 D_r^2 \xi R} + \frac{v_0^4 + D_r D_t v_0^2}{4 D_r^3 D_t R^2} \right]. \tag{57}$$

Hence, the pressure of active particles *inside* a circular wall is *increased*, compared with the active pressure on a straight wall, by an amount proportional to $1/R$.

For particles outside a circular wall, the density profile $\rho(r)$ is given by Eq. (48a), with the denominator A_3 defined in Eq. (48c). The density ρ_{wall} is just the value of $\rho(r)$ at $r = R$, and hence the pressure on the wall is

$$p = \rho_{\text{bulk}} k_B T \left[1 + \frac{\frac{v_0^2}{D_r D_t}}{1 - \frac{v_0^2}{2 D_r D_t} + \left(1 + \frac{v_0^2}{2 D_r D_t} \right) \frac{K_2(R/\xi)}{K_0(R/\xi)}} \right]. \tag{58}$$

For $R \gg \xi$, we can use the asymptotic expansion $K_2(x)/K_0(x) \approx 1 + 2x^{-1} + x^{-2}$ to obtain

$$p = \rho_{\text{bulk}} k_B T \left[1 + \frac{v_0^2}{2 D_r D_t} - \frac{v_0^2}{2 D_r^2 \xi R} + \frac{v_0^4 + D_r D_t v_0^2}{4 D_r^3 D_t R^2} \right]. \tag{59}$$

Hence, the pressure of active particles *outside* a circular wall is *reduced*, compared with the active pressure on a straight wall, by an amount proportional to $1/R$.

The three cases of straight wall, inside circle, and outside circle can all be combined into the single concept of a curvature-dependent active pressure. Let us define the curvature

κ as $\kappa = 0$ for a straight wall, $\kappa = +1/R$ inside a circle, and $\kappa = -1/R$ outside a circle. The three equations (54), (57), and (59) can then be combined into the equation

$$p(\kappa) = \rho_{\text{bulk}} k_B T \left[\left(1 + \frac{v_0^2}{2 D_r D_t} \right) + \left(\frac{v_0^2}{2 D_r^2 \xi} \right) \kappa \right.$$
$$\left. + \left(\frac{v_0^4 + D_r D_t v_0^2}{4 D_r^3 D_t} \right) \kappa^2 \right]. \tag{60}$$

This expression can be written more compactly in terms of the Peclet number $\text{Pe} = v_0/\sqrt{D_t D_r}$ and the particle length scale $a = \sqrt{D_t/D_r}$ as

$$p(\kappa) = \rho_{\text{bulk}} k_B T \left[\left(1 + \tfrac{1}{2}\text{Pe}^2 \right) + \tfrac{1}{2}\text{Pe}^2 \sqrt{1 + \tfrac{1}{2}\text{Pe}^2} a\kappa \right.$$
$$\left. + \tfrac{1}{4}\text{Pe}^2 (1 + \text{Pe}^2) a^2 \kappa^2 \right]. \tag{61}$$

From this result, we can see that the pressure of an active fluid on a wall depends on the shape of the wall through the curvature κ. Of course, this is not the case for an equilibrium fluid; the pressure of an equilibrium fluid depends only on fluid properties, not on the shape of the wall.

This result for the curvature-dependent active pressure is similar to a previous theoretical result of Fily *et al.* [11, 12]. They investigated the active pressure inside a convex box with variable positive curvature, and found that the local pressure is proportional to the local curvature of the boundary. Here we see that the result also applies in a region of negative curvature, such as the outside of a circular wall.

3.5 Applications

In this section we discuss three examples, where we can make predictions for the behavior of active systems based on the concepts of pressure and boundary layers.

3.5.1 Depletion force between two plates

Consider two parallel plates inside a bath of active particles, separated by a distance of $2L$, as shown in Fig. 16. This problem has been investigated through simulations in Ref. [9]. Outside the plates, far from the ends, this problem is equivalent to the infinite straight wall discussed in Sec. 3.3.1, and the density profile is given by Eq. (42a). Between the plates, far from the ends, this problem is equivalent to the infinite parallel walls discussed in Sec. 3.3.2, and the density profile is given by Eq. (44a). Hence, there is a boundary layer with enhanced density on each side of each plate, and thus there is active pressure on each side of each plate. The question is: Do all the boundary layers have the same density enhancement? If the inner boundary layers have a different density enhancement than the outer boundary layers, then the active pressure will either push the plates together or push them apart.

To answer that question, we note that the density profiles (42a) and (44a) have two different overall coefficients. For the density profile outside the plates, the coefficient is ρ_{bulk}, which is the density far from the plates. For the density profile between the plates, the coefficient is ρ_1. To determine ρ_1, we assume that the region midway between the plates is in contact with the bulk region through the openings at the ends, so that the density midway between the plates is equal to ρ_{bulk}. This assumption implies that the density profile between the walls is

$$\rho_{\text{in}}(x) = \frac{\rho_{\text{bulk}}}{1 + \frac{v_0^2}{2D_r D_t}\text{sech}(L/\xi)}\left[1 + \frac{v_0^2}{2D_r D_t}\frac{\cosh(x/\xi)}{\cosh(L/\xi)}\right]. \tag{62}$$

Hence, the active pressure on the inside surface of each wall is

$$p_{\text{in}} = \rho_{\text{in}}^{\text{wall}}k_B T = \frac{\rho_{\text{bulk}}k_B T}{1 + \frac{v_0^2}{2D_r D_t}\text{sech}(L/\xi)}\left(1 + \frac{v_0^2}{2D_r D_t}\right). \tag{63}$$

74
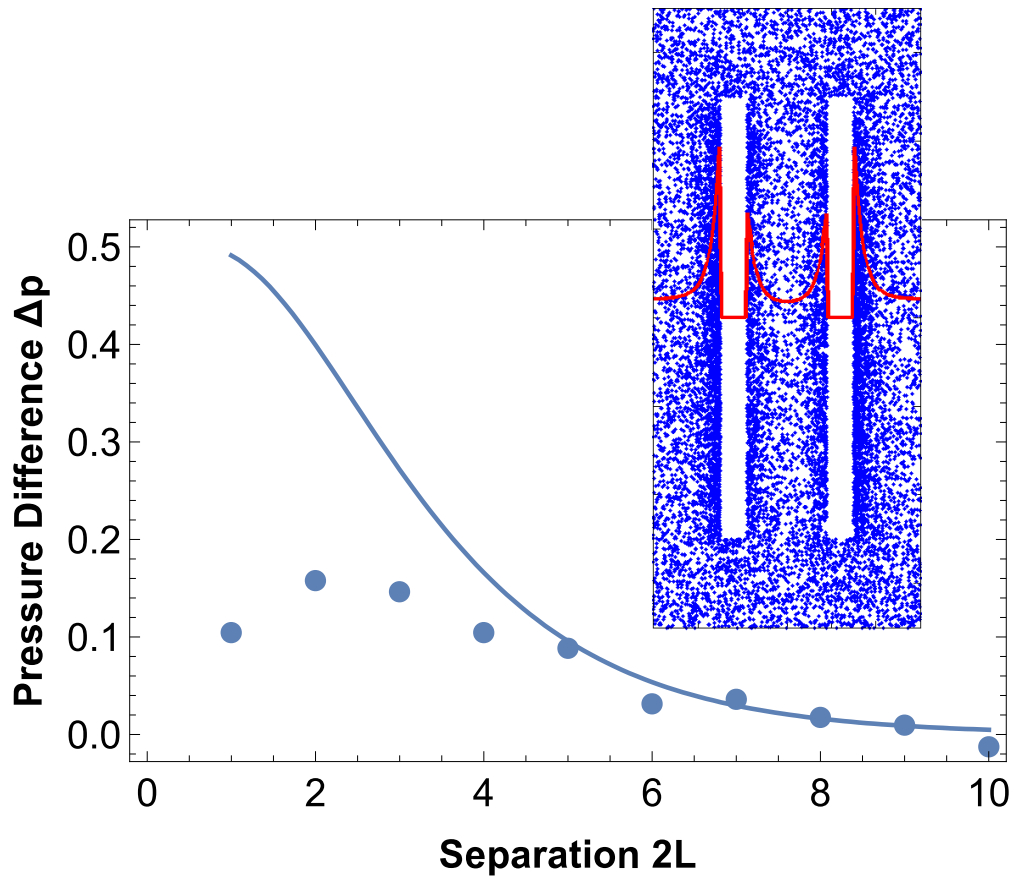
Figure 16: Theory and simulation of two parallel plates in a bath of active Brownian particles. The inset shows a snapshot of the simulation, and the red line represents the density as a function of x along the central axis $y = 0$. The main figure shows the theoretical prediction for the pressure difference as a function of the plate separation $2L$, in comparison with simulation results for the difference in densities at the inner and outer walls. Parameters are $D_r = 1$, $D_t = 1$, $v_0 = 1$, $k_B T = 1$, and plate thickness $s = 0.6$.

By comparison, the active pressure on the outside surface of each wall is

$$p_{\text{out}} = \rho_{\text{out}}^{\text{wall}} k_B T = \rho_{\text{bulk}} k_B T \left(1 + \frac{v_0^2}{2 D_r D_t} \right). \tag{64}$$

Thus, the inside pressure is less than the outside pressure by

$$\Delta p(L) = p_{\text{out}} - p_{\text{in}} = \frac{\rho_{\text{bulk}} k_B T \left(\frac{v_0^2}{2 D_r D_t} \right) \left(1 + \frac{v_0^2}{2 D_r D_t} \right)}{\cosh(L/\xi) + \frac{v_0^2}{2 D_r D_t}}. \tag{65}$$

This pressure difference pushes the plates together. It decays exponentially with L, with the characteristic length scale ξ. Physically, this force on the plates can be regarded as a depletion force, associated with the reduced boundary layer between the plates compared with outside the plates. It appears analogous to the Casimir force between conducting plates, but arises from a different mechanism.

We perform Langevin dynamics simulations of a bath of active Brownian particles around two parallel plates, illustrated in Fig. 16. These simulations show that boundary layers form on both sides of both plates, and the outer boundary layers have higher density than the inner boundary layers, as indicated by the red line in the inset. The relative density of these two boundary layers depends on the separation $2L$ between the plates. The main figure presents the density difference, which is proportional to the pressure difference, in comparison with the prediction of Eq. (65). We can see that the trends are consistent for large separation. For smaller separation, the prediction overestimates the density difference, perhaps because it is more difficult for the density midway between the plates to become equal with ρ_{bulk} when the openings between the plates are so small (comparable to the persistance length $v_0/D_r = 1$ and effective particle size $\sqrt{D_t/D_r} = 1$).
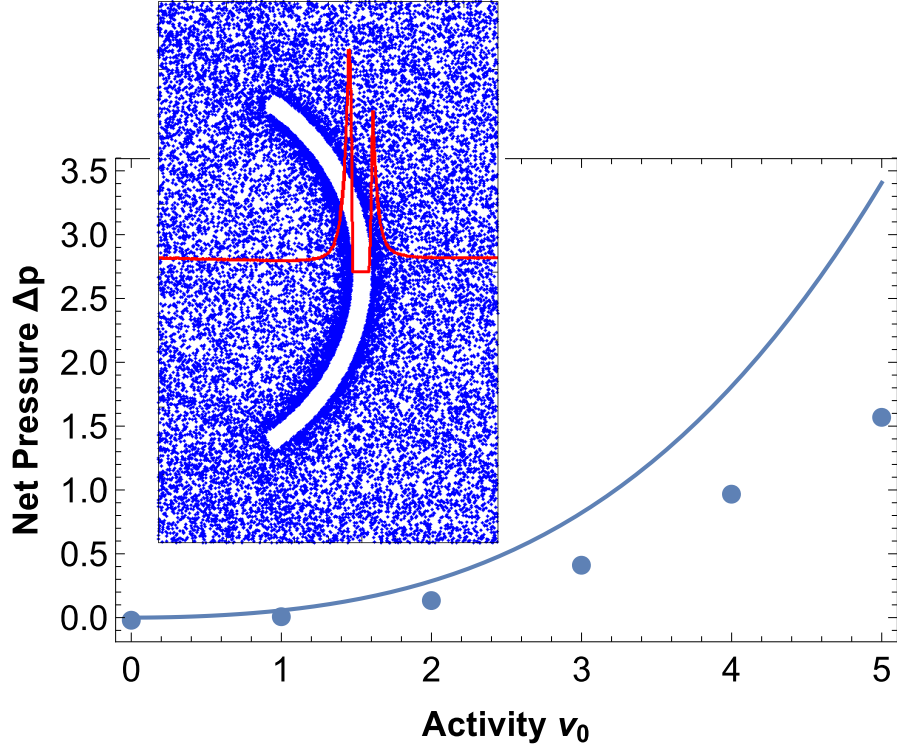
Figure 17: Theory and simulation of a curved tracer in a bath of active Brownian particles. The inset shows the simulation, with the red line representing the density as a function of x along the symmetry axis $y = 0$. The main figure shows the prediction for net pressure as a function of activity v_0, in comparison with the simulation results for the density difference between the two sides of the tracer. Parameters are $D_r = 2$, $D_t = 1$, $k_B T = 1$, tracer radius $R = 7$, and tracer thickness $s = 0.6$.

3.5.2 Force on a curved tracer particle

Consider a curved tracer surrounded by a bath of active particles, as shown in Fig. 17. This type of geometry has been studied through simulations in Refs. [7, 8]. A boundary layer forms on both sides of the tracer, and it experiences active pressure on both sides. Based on the argument in Sec. 3.4, the pressure in the inner side is greater than the pressure on the outer side. As a result, the bath of active particles exerts a net force on the tracer, causing it to move.

To estimate the net force, we use Eq. (60) for the pressure as a function of curvature. On the inner side, we have the curvature $\kappa = 1/(R - s/2)$, where R is the radius of the

midline and s is the thickness of the tracer. On the outer side, we have $\kappa = -1/(R-s/2)$. We assume that ρ_{bulk} is the same on both sides, because the bulk regions can easily exchange particles. Hence, for large R and small s, the net pressure becomes

$$\Delta p = \frac{\rho_{\mathsf{bulk}} k_B T v_0^2}{D_r^2 \xi R} \left(1 + \frac{s^2}{R^2} \right). \tag{66}$$

Through Langevin dynamics simulations, we visualize the distribution of active particles around the tracer and calculate the density along the symmetry axis, as indicated by the red line in the Fig. 17 inset. This simulation result shows the higher density on the inner side than on the outer side, and hence a higher pressure. In the main figure, we show the density difference in the simulation in comparison with the prediction from Eq. (66). This results show a consistent trend, although the prediction is higher by about a factor of 2. Hence, the approximate argument about a curvature-dependent pressure provides a simple way to understand the net pressure on the tracer.

Experiments have demonstrated that the active motion of swimming bacteria causes an asymmetric gear to rotate [3–5]. The structure of the asymmetric gear is equivalent to several curved tracer particles linked together, and hence we expect that the argument in this section would also apply to the gear.

3.5.3   Corral

As a variation on the curved tracer, consider the active particle corral shown in Fig. 18. Here, the wall is almost a full circle, with only a small opening connecting inside and outside. The density at the inner boundary is related the the density at the center of the circle by Eq. (46a), and the density at the outer boundary is related to the bulk density by Eq. (48a). The question is then: How are the inside and outside densities related to

each other? For this geometry with only a small opening, it seems reasonable that the density of the inside boundary layer should match the density of the outside boundary layer, $\rho_{\text{in}}(R) = \rho_{\text{out}}(R)$. This equation gives us a relationship between the density at the center of the circle and the bulk density. For $R \gg \xi$, that relationship becomes

$$\frac{\rho_{\text{center}}}{\rho_{\text{bulk}}} = 1 - \frac{v_0^2}{D_r D_t} \frac{\xi}{R}.$$

(67)

This equation shows that the corral has a reduced density at the center, compared with the bulk density. Intuitively, this behavior occurs because it is easier for active particles to escape from the corral than to enter it, as the curvature inside guides particles towards the opening. It would not occur for an equilibrium fluid, which would have equal density inside and outside the corral. Thus tunable rectification of active particles can be achieved through this mechanism similarly to methods reported earlier by various research groups [16].

We carry out Langevin dynamics simulations of a bath of active particles around the corral in Fig. 18. These simulations show that the average density around the center is reduced compared with the bulk exterior, as shown by the red line. The main figure presents the simulation results for the density ratio as a function of activity, in comparison with the prediction from Eq. (67), and these results are generally consistent. Hence, the approximate argument about boundary layers provides a way to understand the relative densities in this geometry.
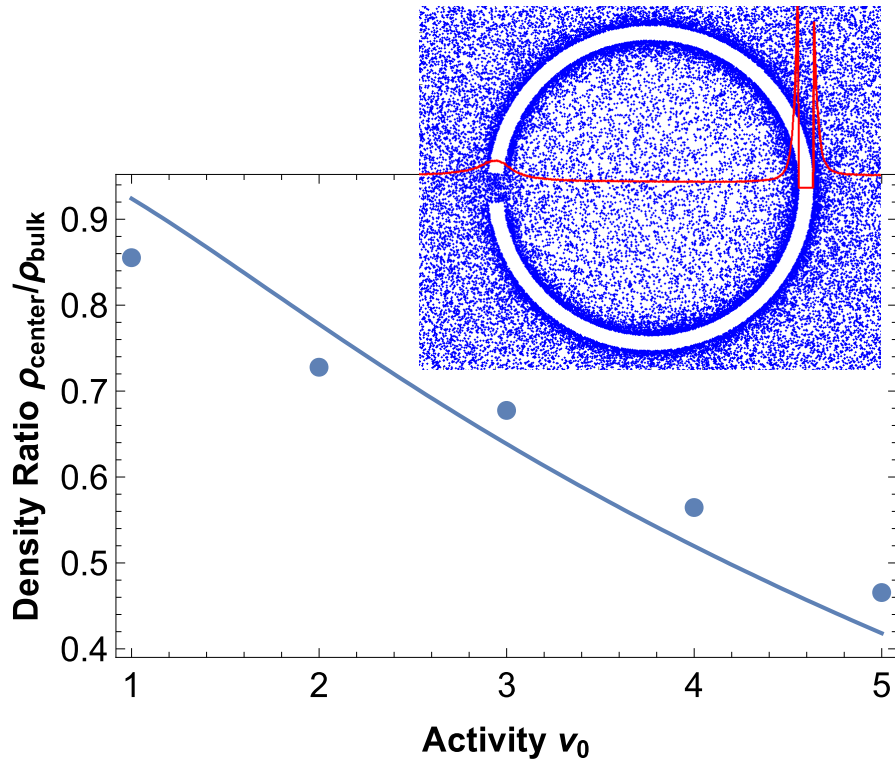
Figure 18: Theory and simulation of an active particle corral. A snapshot of the simulation is shown in the inset, with the red line representing the density as a function of x in a slice across the corral. The main figure shows the density ratio $\rho_{\text{center}}/\rho_{\text{bulk}}$ as a function of activity v_0, with the points representing simulation results and the line representing the theory of Eq. (67). Parameters are $D_r = 2$, $D_t = 1$, $k_B T = 1$, and corral radius $R = 4$.

BIBLIOGRAPHY

[1] M. C. Marchetti, J. F. Joanny, S. Ramaswamy, T. B. Liverpool, J. Prost, M. Rao, and R. A. Simha, "Hydrodynamics of soft active matter," *Rev. Mod. Phys.*, vol. 85, pp. 1143–1189, Jul 2013.

[2] C. Bechinger, R. Di Leonardo, H. Löwen, C. Reichhardt, G. Volpe, and G. Volpe, "Active Particles in Complex and Crowded Environments," *Rev. Mod. Phys.*, vol. 88, p. 045006, Nov 2016.

[3] L. Angelani, R. Di Leonardo, and G. Ruocco, "Self-Starting Micromotors in a Bacterial Bath," *Phys. Rev. Lett.*, vol. 102, p. 048104, Jan 2009.

[4] A. Sokolov, M. M. Apodaca, B. A. Grzybowski, and I. S. Aranson, "Swimming bacteria power microscopic gears," *Proc. Natl. Acad. Sci. U.S.A.*, vol. 107, no. 3, pp. 969–974, 2010.

[5] C. Maggi, F. Saglimbeni, M. Dipalo, F. De Angelis, and R. Di Leonardo, "Micromotors with asymmetric shape that efficiently convert light into work by thermocapillary effects," *Nat. Commun.*, vol. 6, p. 7855, Jul 2015.

[6] A. P. Berke, L. Turner, H. C. Berg, and E. Lauga, "Hydrodynamic attraction of swimming microorganisms by surfaces," *Phys. Rev. Lett.*, vol. 101, p. 038102, Jul 2008.

[7] S. A. Mallory, C. Valeriani, and A. Cacciuto, "Curvature-induced activation of a passive tracer in an active bath," *Phys. Rev. E*, vol. 90, p. 032309, Sep 2014.

[8] S. A. Mallory, C. Valeriani, and A. Cacciuto, "Anomalous dynamics of an elastic membrane in an active fluid," *Phys. Rev. E*, vol. 92, no. 1, p. 012314, 2015.

[9] D. Ray, C. Reichhardt, and C. J. O. Reichhardt, "Casimir effect in active matter systems," *Phys. Rev. E*, vol. 90, no. 1, p. 013019, 2014.

[10] A. P. Solon, Y. Fily, A. Baskaran, M. E. Cates, Y. Kafri, M. Kardar, and J. Tailleur, "Pressure is not a state function for generic active fluids," *Nat. Phys.*, vol. 11, pp. 673–678, Jun 2015.

[11] Y. Fily, A. Baskaran, and M. F. Hagan, "Dynamics of self-propelled particles under strong confinement," *Soft Matter*, vol. 10, no. 30, pp. 5609–5617, 2014.

[12] Y. Fily, A. Baskaran, and M. F. Hagan, "Dynamics and density distribution of strongly confined noninteracting nonaligning self-propelled particles in a nonconvex boundary," *Phys. Rev. E*, vol. 91, p. 012125, Jan 2015.

[13] F. Smallenburg and H. Löwen, "Swim pressure on walls with curves and corners," *Phys. Rev. E*, vol. 92, p. 032304, Sep 2015.

[14] W. Yan and J. F. Brady, "The force on a boundary in active matter," *Journal of Fluid Mechanics*, vol. 785, 2015.

[15] B. Ezhilan and D. Saintillan, "Transport of a dilute active suspension in pressure-driven channel flow," *Journal of Fluid Mechanics*, vol. 777, pp. 482–522, 2015.

[16] C. O. Reichhardt and C. Reichhardt, "Ratchet effects in active matter systems," *Annual Review of Condensed Matter Physics*, vol. 8, no. 1, pp. 51–75, 2017.

APPENDICES

3.A   Exact calculation of wall density

The purpose of this appendix is to show that the relationship between the wall density ρ_{wall} and the bulk density ρ_{bulk} is exact in one dimension, and does not depend on the truncation of moments.

We begin with the moment equations (36) in steady state,

$$0 = -\frac{\partial J_x^{(0)}}{\partial x}, \tag{68a}$$

$$0 = -\frac{\partial J_{xx}^{(1)}}{\partial x} - D_r M_x. \tag{68b}$$

Integrating Eq. (68a) gives $J_x^{(0)} = $ constant. Because no particles are entering or leaving the system at $x \to \pm\infty$, we must have $J_x^{(0)} = 0$. From the definition of $J_x^{(0)}$ in Eq. (36a), this equation implies

$$v_0 M_x - D_t \frac{\partial \rho}{\partial x} = 0. \tag{69}$$

Integrating once again, we obtain

$$v_0 \int_0^\infty M_x(x)dx = D_t[\rho(\infty) - \rho(0)]. \tag{70}$$

By comparison, integrating Eq. (68b) implies

$$D_r \int_0^\infty M_x(x)dx = J_{xx}^{(1)}(0) - J_{xx}^{(1)}(\infty). \tag{71}$$

At the wall $x = 0$, there is no current, so that $J_{xx}^{(1)}(0) = 0$. Away from the wall, the fluid becomes isotropic, and hence all the moments of the distribution function vanish, except

83

for $\rho(\infty) = \rho_{bulk}$. From the definition of $J_{xx}^{(1)}$ in Eq. (36b), we obtain $J_{xx}^{(1)}(\infty) = \frac{1}{2}v_0\rho_{bulk}$.

Combining Eqs. (70) and (71) then yields

$$
\begin{aligned}
\frac{D_t}{v_0} \left[\rho_{\mathsf{bulk}} - \rho(0)\right] &= -\frac{v_0}{2D_r}\rho_{\mathsf{bulk}}, \\
\rho_{\mathsf{wall}} = \rho(0) &= \rho_{\mathsf{bulk}} \left(1 + \frac{v_0^2}{2D_r D_t}\right).
\end{aligned}
\tag{72}
$$

Hence, the active pressure directly follows as

$$
p = \rho_{\mathsf{wall}} k_B T = \rho_{\mathsf{bulk}} k_B T \left(1 + \frac{v_0^2}{2D_r D_t}\right).
\tag{73}
$$

CHAPTER 4

Skyrmions in Liquid-Crystals and Chiral Magnets[1]

4.1   Introduction

In chiral systems, isolated or periodic arrays of topological defects can exist as stable minimum energy states. In some cases, the defects are skyrmions, which have $180°$ double twist going outward from the center, and hence can pack together without singularities in the orientational order. In other cases, the defects are merons, which have $90°$ double twist going outward from the center. See Fig. 19.

When chiral liquid crystals are confined in an anisotropic environment, they experience geometric frustration: The chirality favors a twist in the director field, but the anisotropy favors a director orientation that is incompatible with twist [1,2]. Because of this frustration, these liquid crystals form complex topological defect structures, with regions of twist

---

[1]Part of the work in this chapter was published in arXiv:1711.07823

(a) Skyrmion   (b) Meron (half skyrmion)
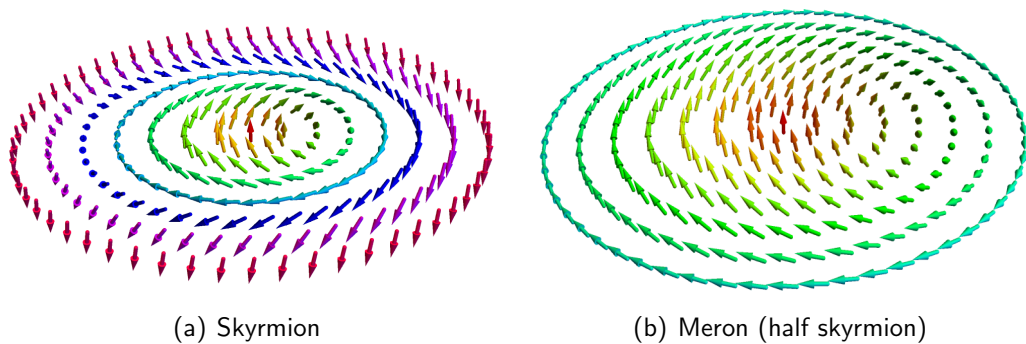
Figure 19: 2D skyrmion and meron with 3D directors.

separating regions of the favored orientation. In some cases, these defects are walls with a one-dimensional (1D) twist of the director field $n(x)$ [3]. In other cases the defects are skyrmions, which have a 2D variation of the director field $n(x, y)$ with double twist going outward from the center, covering all possible orientations on the unit sphere [4–11]. See Fig. 19. In even more complex cases, the defects are hopfions, with a 3D variation of the director field $n(x, y, z)$ in a knotted texture [12, 13].

An important feature of all three cases—walls, skyrmions, and hopfions—is that the orientation varies in a topological configuration that cannot anneal away, but the magnitude of the order parameter remains constant. Unlike typical topological vortices, there is no singularity where the magnitude goes to zero (or otherwise changes away from its bulk value [14]). These nonsingular defects were originally proposed in nuclear physics [15], and they are now studied extensively in condensed matter, especially in chiral magnets [16–21], where they have potential applications in magnetic memory and logic.

The nonsingular defect structure of skyrmions can be compared with blue phases in chiral liquid crystals [22–24]. A blue phase consists of a periodic array of double-twist tubes. Each tube has a 2D variation of the director field going outward from the center, similar to a skyrmion except that it covers only half of the unit sphere. In that sense, the double-twist tubes can be regarded as half-skyrmions, which are called merons [25]. There is one crucial difference between blue phases and skyrmions: In a blue phase, the double-twist tubes are separated by disclinations, which are singularities in the director field, where the magnitude of nematic order changes away from its bulk value. Hence, an important issue in chiral liquid crystals is how to understand the crossover between skyrmions and blue phases. Why would a chiral liquid crystal form singular or nonsingular

86

defect structures?

A further theoretical issue is how to compare skyrmions and blue phases in liquid crystals with analogous structures in chiral magnets. Both liquid crystals and magnets have orientational order parameters with magnitudes and directions. They can both exhibit nonsingular defects (with constant magnitude of the order parameter), as well as singular defects (with the magnitude vanishing or otherwise changing away from its bulk value). The main difference between these materials is the symmetry of the orientational order parameter: liquid crystals have a tensor order parameter, while magnets have a vector order parameter. How does this difference of symmetry affect the skyrmions or blue phases that form in the material?

The purpose of this work is to address these issues through theoretical studies of chiral liquid crystals and magnets. In Sec. 4.2, we consider a simple analytic model for chiral liquid crystals, and show that there are four characteristic energy scales: the energy associated with the magnitude of nematic order, the chiral interaction, the anisotropy, and the temperature. We derive a phase diagram in terms of three dimensionless ratios of these energies. This phase diagram includes classical results for blue phases with no anisotropy, and extends the analysis to include anisotropy. It shows that blue phases are stable when the energy associated with the magnitude of nematic order is relatively low. Skyrmions are not stable structures in this phase diagram, but they can be metastable when that energy scale is high.

In Sec. 4.3, we present Monte Carlo and relaxational dynamic simulations of the model for chiral liquid crystals. These numerical simulations confirm the phase diagram derived through simple analytic approximations. They also show the formation of skyrmions as

metastable defects, with length scales that can be understood analytically.

In Sec. 4.4, we extend the simple analytic model to describe chiral magnets, which have a Dzyaloshinskii-Moriya (DM) term in the free energy, arising from Dresselhaus spin-orbit coupling. In this case, there are four characteristic energies: the energy associated with the magnitude of magnetic order, the chiral DM interaction, the anisotropy, and the applied magnetic field, while the temperature scales out of the problem. We derive a phase diagram in terms of three dimensionless ratios of these energies, and show that this phase diagram is quite similar to previous results from more detailed numerical calculations. The results are generally similar to the liquid-crystal case, but with one important difference: In magnets, skyrmions can be stabilized by the competition between anisotropy and applied magnetic field. This competition is not available in liquid crystals because of the tensor nature of the order parameter.

In this work, we only consider the formation of skyrmions or blue phases driven by bulk chirality, known as Dresselhaus spin-orbit coupling in the magnetic case. We should note briefly that modulated structures can also be driven by another mechanism for broken inversion symmetry. In liquid crystals, that mechanism is called polarity. Polarity is often induced by surfaces, and the phenomenon of surface-induced modulations has been studied for many years [26, 27]. More recently, spontaneous bulk polarity has also been found in certain liquid crystals, and theoretical research has predicted that bulk polarity can induce blue phases [28, 29]. In magnets, the analogous mechanism for broken inversion symmetry at surfaces is called Rashba spin-orbit coupling, and it has also been shown to favor the formation of skyrmions [30]. Although we have only investigated the comparison between chiral (Dresselhaus) defects in liquid crystals and magnets, we expect that the

same considerations will apply to polar (Rashba) defect structures.

4.2 Theory of chiral liquid crystals

4.2.1 Model

We begin with the theory of chiral liquid crystals, as usually studied in the context of blue phases. A liquid crystal is described by a tensor order parameter $\boldsymbol{Q}(\boldsymbol{r})$, which is related to the scalar order $S(\boldsymbol{r})$ and the director field $\boldsymbol{n}(\boldsymbol{r})$ by $Q_{\alpha\beta} = S(\frac{3}{2}n_\alpha n_\beta - \frac{1}{2}\delta_{\alpha\beta})$. In Landau-de Gennes theory, the free energy density can be expressed in terms of $\boldsymbol{Q}$ as

$$
\begin{aligned}
F \;=\; & \frac{1}{2}a\,\mathrm{Tr}\,\boldsymbol{Q}^2 + \frac{1}{3}b\,\mathrm{Tr}\,\boldsymbol{Q}^3 + \frac{1}{4}c\left(\mathrm{Tr}\,\boldsymbol{Q}^2\right)^2 \\
& + \frac{1}{2}L(\partial_\gamma Q_{\alpha\beta})(\partial_\gamma Q_{\alpha\beta}) - 2Lq_0\epsilon_{\alpha\beta\gamma}Q_{\alpha\delta}\partial_\gamma Q_{\beta\delta}.
\end{aligned}
\tag{74}
$$

Here, the first three terms represent the free energy of a uniform system, expanded in powers of the tensor order parameter. These terms favor certain eigenvalues of $\boldsymbol{Q}$, which correspond to a certain magnitude of uniaxial nematic order. The quadratic coefficient a is assumed to vary linearly with temperature, while b and c are assumed constant with respect to temperature. The fourth and fifth terms represents the elastic free energy associated with variations of $\boldsymbol{Q}$ as a function of position. The fourth term penalizes splay, twist, and bend deformations equally, with an elastic coefficient L. The fifth term favors a chiral twist of the nematic order, with a characteristic inverse length q_0 arising from the molecular chirality. We neglect other possible elastic terms that give different energy costs for splay, twist, and bend, such as $\frac{1}{2}L_2(\partial_\alpha Q_{\alpha\gamma})(\partial_\beta Q_{\beta\gamma})$.

In the context of blue phases, following the work of Grebel et al. [22], researchers normally rescale parameters to simplify the theory. To motivate this rescaling, it is convenient to consider the specific temperature at which $a = 0$. This temperature is below

the first-order isotropic-nematic transition, which occurs at a positive value of a. At this temperature, the first four terms in the free energy favor a nematic phase with order parameter $S \sim |b|/c$, the free energy density of the nematic relative to isotropic phase is $F \sim b^4/c^3$, and the core radius of a disclination in nematic order is $\xi \sim (Lc/b^2)^{1/2}$. Hence, at general temperature, we rescale the Q tensor, the free energy density, and all lengths by those characteristic values. In particular, we define the scaled free energy density as $\tilde{F} = Fc^3/b^4$. The theory then depends only on two dimensionless ratios, which are normally written as

$$t = \frac{27ac}{b^2}, \qquad \kappa = \sqrt{\frac{108cLq_0^2}{b^2}}. \tag{75}$$

The parameter t is a dimensionless temperature, which represents the temperature-dependent quadratic coefficient a relative to b and c. The parameter κ is a dimensionless chirality, which represents the natural twist q_0 relative to the disclination core radius ξ. We can express the same comparison in terms of energies. The free energy density associated with the favored chiral twist is $LS^2q_0^2$, while the free energy density of a disclination core is $LS^2\xi^{-2}$. Hence, κ^2 can be interpreted as the energy scale of the favored chiral twist relative the energy scale associated with changing the eigenvalues of $\boldsymbol{Q}$ inside a disclination core. A liquid crystal material with low κ is usually called "low chirality," but it could equally well be called "stiff nematic order." Likewise, a material with high κ is usually called "high chirality," but it could be called "soft nematic order."

In many experiments, a liquid crystal is placed in an anisotropic environment, which favors some alignment of nematic order with respect to a certain axis, which we can call the z axis. If the anisotropy favors alignment along the axis, it is called "easy axis"; if

it favors alignment perpendicular to the axis, it is called "easy plane." There are two common mechanisms for anisotropy. First, an electric field can be applied along the z axis, leading to a dielectric anisotropy. This field alignment can be represented by an additional term in the free energy of

$$\Delta F = -\Delta\epsilon E^2 Q_{zz}, \tag{76}$$

with $F_{\text{total}} = F + \Delta F$. This term gives easy axis anisotropy if $\Delta\epsilon > 0$ and easy plane anisotropy if $\Delta\epsilon < 0$. Following the same argument as above, we can rescale this term as $\Delta\tilde{F} = \Delta F c^3/b^4$ to obtain the dimensionless anisotropy

$$\alpha = \frac{\Delta\epsilon E^2 c^2}{|b|^3}. \tag{77}$$

A second mechanism for anisotropy is to put a liquid crystal in a narrow cell, of thickness d, between two surfaces with strong anchoring. Homeotropic anchoring gives easy-axis anisotropy on the bulk liquid crystal, while planar anchoring gives easy-plane anisotropy. To see the analogy between field-induced and surface-induced anisotropy, suppose the nematic order at the midplane is tilted at a small angle θ with respect to the z axis. For field-induced anisotropy, the extra free energy density (relative to an untilted state) is $\Delta\epsilon E^2 S\theta^2$. For surface-induced anisotropy, the extra free energy density is $LS^2\theta^2/d^2$. Hence, the effect of surface-induced anisotropy is similar to field-induced anisotropy with an effective $\Delta\epsilon E^2 \sim LS/d^2$, and effective $\alpha \sim (Lc)/(d^2b^2)$. Of course, this analogy is an approximation for small tilt, and may break down when the tilt becomes larger.

Our goal is now to determine what modulated structures of the $\mathbf{Q}$ tensor minimize the free energy. In particular, does the system form nonsingular defects, such as walls,

skyrmions, and hopfions, with approximately constant eigenvalues of $\boldsymbol{Q}$? Or does it form blue phases, with double-twist tubes (or merons) separated by disclinations in which the eigenvalues change away from their bulk values? The results must be controlled by the three dimensionless parameters t, κ, and α.

As a minimal model to address this question, we consider a 3D nematic order tensor that depends only on two spatial coordinates, $\boldsymbol{Q}(x, y)$, with no dependence on the third spatial coordinate z, under field-induced anisotropy. This model can describe walls and skyrmions, although not hopfions. Furthermore, it can describe a simple version of blue phases as vertical double-twist tubes (merons) separated by vertical disclinations, although it cannot describe the cubic structure of real 3D blue phases.

4.2.2 Simple analytic calculations

As a first step in analyzing this model, we make assumptions about $\boldsymbol{Q}(x, y)$ in each of the possible structures and calculate the free energies. By comparing the free energies, we determine a phase diagram in terms of t, κ, and α. Of course, we recognize that these assumptions are very simple. For that reason, in the following section we verify the results through Monte Carlo simulations of the model.

Isotropic phase

In the isotropic phase, the system is disordered with $\boldsymbol{Q} = 0$ everywhere. The scaled free energy density is $\tilde{F}_\text{iso} = 0$, and the anisotropy contributes $\Delta \tilde{F}_\text{iso} = 0$. In this analysis, we neglect any slight paranematic order that might be induced by the anisotropy.

Vertical nematic phase

In the vertically aligned nematic phase, the director is $\hat{\boldsymbol{n}} = \hat{\boldsymbol{z}}$, and the order tensor is $Q_{\alpha\beta} = S(\frac{3}{2}n_\alpha n_\beta - \frac{1}{2}\delta_{\alpha\beta})$. From Eq. (74), the free energy becomes $F = \frac{3}{4}aS^2 + \frac{1}{4}bS^3 + \frac{9}{16}cS^4$. Minimizing with respect to the order parameter S gives $S_{\text{vnem}} = (-b + \sqrt{b^2 - 24ac})/(6c)$, and hence the scaled free energy density is

$$\tilde{F}_{\text{vnem}} = -\frac{\left(3 + \sqrt{9 - 8t}\right)^2 \left(3 + \sqrt{9 - 8t} - 4t\right)}{93312}. \tag{78}$$

The anisotropy makes an additional contribution of $\Delta\tilde{F} = -\alpha Q_{zz} = -\alpha S$, which implies

$$\Delta\tilde{F}_{\text{vnem}} = -\frac{\alpha\left(3 + \sqrt{9 - 8t}\right)}{18}. \tag{79}$$

Planar nematic phase

In the horizontally aligned nematic phase, the director is $\hat{\boldsymbol{n}} = \hat{\boldsymbol{x}}$. Most of the analysis is the same as for the vertically aligned nematic phase, with the same order parameter S_{pnem} and the same scaled free energy density $\tilde{F}_{\text{pnem}}$. However, the anisotropy now contributes $\Delta\tilde{F} = -\alpha Q_{zz} = +\frac{1}{2}\alpha S$, and hence

$$\Delta\tilde{F}_{\text{pnem}} = \frac{\alpha\left(3 + \sqrt{9 - 8t}\right)}{36}. \tag{80}$$

Cholesteric phase (lattice of walls)

A cholesteric phase has the twisted structure shown in Fig. 20 (middle column). It can be regarded as a periodic lattice of twist walls, separating regions in which the director field is aligned with the anisotropy. To a first approximation, we assume that the director field is unperturbed by the anisotropy, so that $\hat{\boldsymbol{n}}(x) = -\hat{\boldsymbol{y}}\sin(\pi x/d) + \hat{\boldsymbol{z}}\cos(\pi x/d)$, where d is the pitch. The free energy is then $F = \frac{3}{4}aS^2 + \frac{1}{4}bS^3 + \frac{9}{16}cS^4 + \frac{9}{4}\pi^2 LS^2 d^{-2} -$
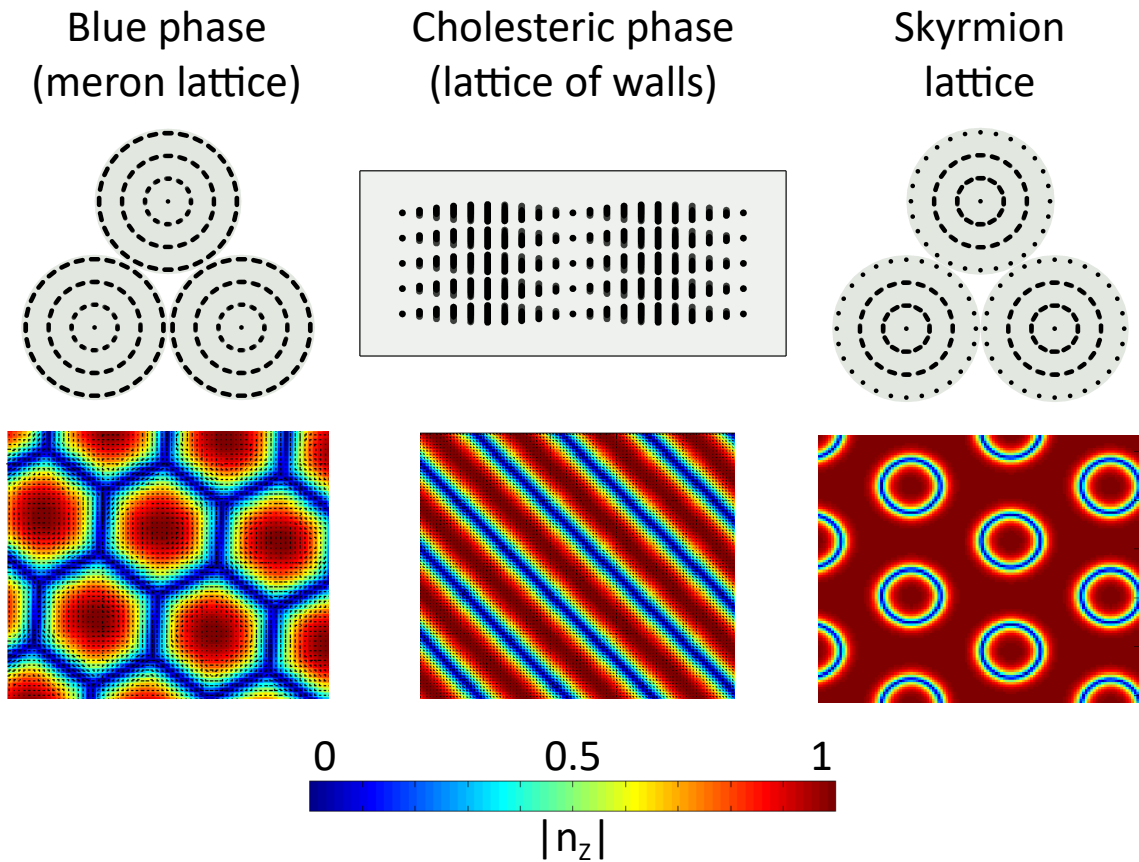
Figure 20: Structure of the modulated liquid-crystal phases studied: blue phase (meron lattice), cholesteric phase (lattice of walls), and skyrmion lattice. The top row shows schematic views of the director field, and the bottom row shows Monte Carlo simulation results (with the color scale indicating $|n_z|$.

$\frac{9}{2}\pi L q_0 S^2 d^{-1}$. By minimizing with respect to d and S, we obtain $d_{\text{chol}} = \pi/q_0$ and

$S_{\text{chol}} = (-b + \sqrt{b^2 - 24ac + 72cLq_0^2})/(6c)$, and the scaled free energy density becomes

$$\tilde{F}_{\text{chol}} = -\frac{1}{93312}\left(3 + \sqrt{9 - 8t + 6\kappa^2}\right)^2 \times \tag{81}$$
$$\times \left(3 - 4t + 3\kappa^2 + \sqrt{9 - 8t + 6\kappa^2}\right).$$

The scaled free energy density associated with the anisotropy now depends on x, and it

averages to $\Delta\tilde{F} = -\alpha\langle Q_{zz}\rangle = -\frac{1}{4}\alpha S$, giving

$$\Delta\tilde{F}_{\text{chol}} = -\frac{\alpha\left(3 + \sqrt{9 - 8t + 6\kappa^2}\right)}{72}. \tag{82}$$

Blue phase (meron lattice)

In 2D, a blue phase has the structure shown in Fig. 20 (left column). It consists of a hexagonal lattice of double-twist tubes, which can be regarded as merons or half-skyrmions. In each meron, the director twists through an angle of $\pi/2$, from a vertical orientation at the center to a horizontal orientation at the edge of the tube. A simple assumption for this variation can be expressed in cylindrical coordinates as $\hat{\boldsymbol{n}}(r) = -\hat{\boldsymbol{\phi}}\sin(\pi r/d) + \hat{\boldsymbol{z}}\cos(\pi r/d)$, for $0 \le r \le d/2$, where d is the diameter of the tube. In each region between three tubes, the director field is in the (x, y) plane, and it has a disclination with topological charge of $-1/2$. The argument of Ref. [14] shows that the $\boldsymbol{Q}$ tensor becomes biaxial in the disclination core, but to a first approximation we will simply consider the core as an isotropic region.

To estimate the average free energy density of the blue phase, we represent each unit cell of the lattice (with area $A = \sqrt{3}d^2/2$) as one meron (with $A = \pi d^2/4$) and two

disclinations (with the remaining area), and obtain

$$
\begin{aligned}
\langle F \rangle &= \frac{F_{\text{meron}} A_{\text{meron}} + 2 F_{\text{defect}} A_{\text{defect}}}{\sqrt{3} d^2 / 2} \\
&= \frac{\pi \sqrt{3} a S^2}{8} + \frac{\pi b S^3}{8\sqrt{3}} + \frac{3\pi \sqrt{3} c S^4}{32} \\
&\quad + \frac{33.5 L S^2}{d^2} - \frac{3\sqrt{3} L q_0 S^2 (4 + \pi^2)}{4d}
\end{aligned}
\tag{83}
$$

We then minimize over d to find $d_{\text{meron}} = 3.7/q_0$, and we use the same value of S as in

the cholesteric calculation. The average scaled free energy density then becomes

$$
\langle F_{\text{meron}} \rangle = - \left(9.7 \times 10^{-6} \right) \left(3 + \sqrt{9 - 8t + 6\kappa^2} \right)^2 \times
$$

$$
\times \left(3 - 4t + 4.1\kappa^2 + \sqrt{9 - 8t + 6\kappa^2} \right).
\tag{84}
$$

Similarly, the scaled free energy density associated with the anisotropy averages to

$$
\langle \Delta F_{\text{meron}} \rangle = 0.0027\alpha \left(3 + \sqrt{9 - 8t + 6\kappa^2} \right)
\tag{85}
$$

Skyrmion lattice

A hexagonal lattice of skyrmions is shown in Fig. 20 (right column). In each skyrmion,

the director twists through an angle of π, from vertical at the center to horizontal and

back to vertical at the edge. A simple assumption for this variation can be expressed as

$\hat{\boldsymbol{n}}(r) = -\hat{\boldsymbol{\phi}} \sin(2\pi r/d) + \hat{\boldsymbol{z}} \cos(2\pi r/d)$, for $0 \le r \le d/2$. In each region between three

tubes, the director field is vertical, and hence there are no disclinations.

As in the previous case, we represent each unit cell of the lattice (with $A = \sqrt{3} d^2 / 2$)

as one skyrmion (with $A = \pi d^2 / 4$) and two vertical nematic regions (with the remaining

96

area), so that the average free energy density becomes

$$\langle F \rangle = \frac{F_{\text{skyrmion}} A_{\text{skyrmion}} + 2F_{\text{vnem}} A_{\text{vnem}}}{\sqrt{3}d^2/2} \tag{86}$$

$$= \frac{3aS^2}{4} + \frac{bS^3}{4} + \frac{9cS^4}{16} + \frac{100.4LS^2}{d^2} - \frac{3\sqrt{3}\pi^2 Lq_0 S^2}{2d}$$

After the same minimization as in the previous case, we obtain $d_{\text{skyrmion}} = 7.8/q_0$ and

$$\tilde{F}_{\text{skyrmion}} = -\frac{1}{93312}\left(3 + \sqrt{9 - 8t + 6\kappa^2}\right)^2 \times \tag{87}$$

$$\times \left(3 - 4t + 1.37\kappa^2 + \sqrt{9 - 8t + 6\kappa^2}\right).$$

The anisotropy further contributes

$$\Delta\tilde{F}_{\text{skyrmion}} = -\frac{\alpha(8 - \pi\sqrt{3})\left(3 + \sqrt{9 - 8t + 6\kappa^2}\right)}{144}. \tag{88}$$

Phase diagram

We now have approximate algebraic expressions for the free energy $F_{\text{total}} = F + \Delta F$ for each of the six structures considered above, as functions of the three dimensionless variables: temperature t, chirality κ, and anisotropy α. For each set of (t, κ, α), we determine which structure has the lowest free energy, and hence construct a phase diagram for the system.

First, consider the case of no anisotropy, $\alpha = 0$. The phase diagram in the (t, κ) plane is shown in Fig. 21. At high temperature, the system is in the disordered isotropic phase. At lower temperature, for high chirality, the system forms a blue phase (meron lattice). In this structure, there are favorable contributions to the free energy from the optimal magnitude of nematic order and from the optimal double twist of the director field within the merons. There is an unfavorable contribution to the free energy from
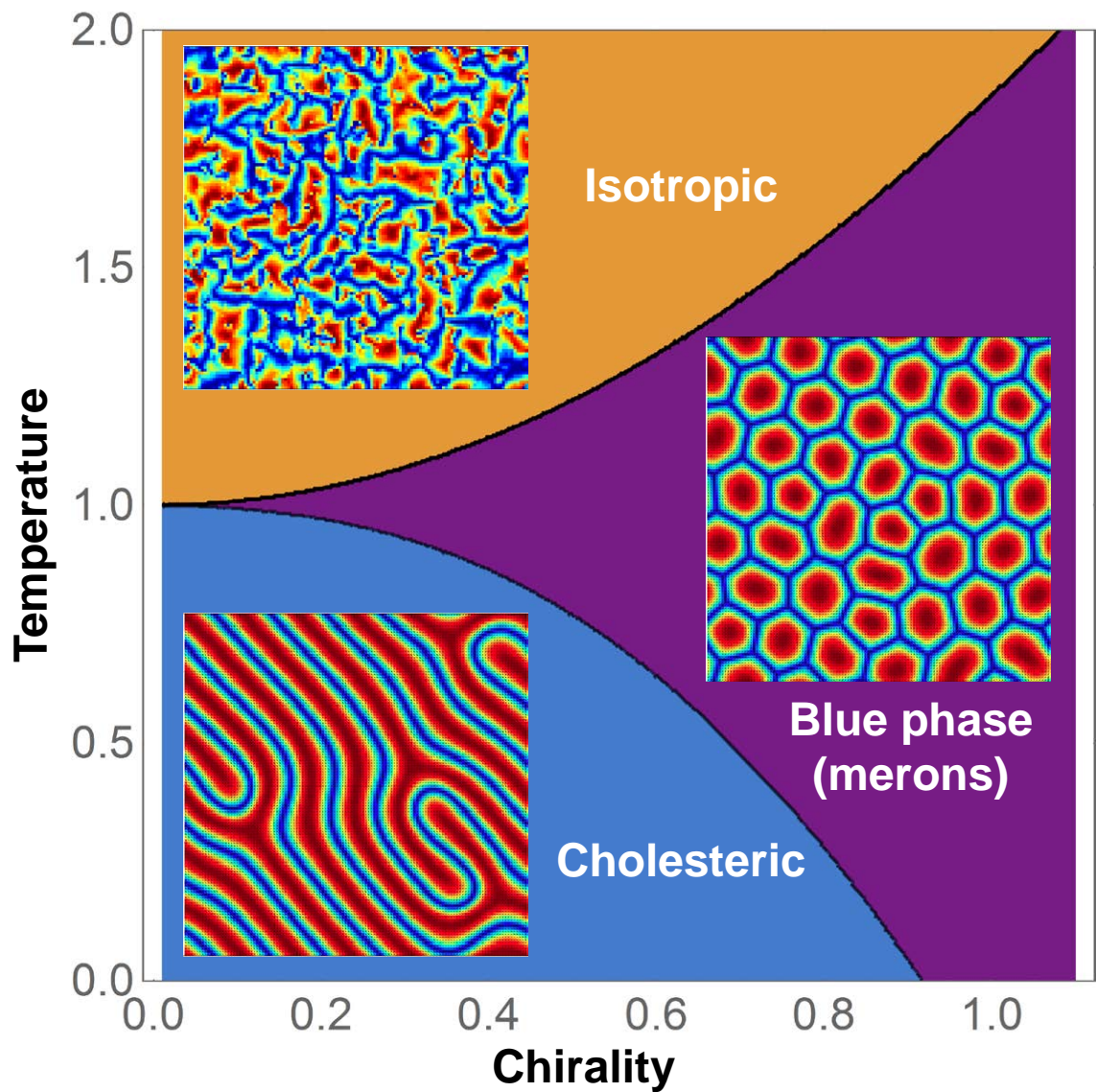
Figure 21: Phase diagram for chiral liquid crystals in the temperature-chirality plane, with no anisotropy. The insets show structures calculated by the simulations. In those structures, the colors represent $|n_z|$, with the same color scale as in Fig. 20.
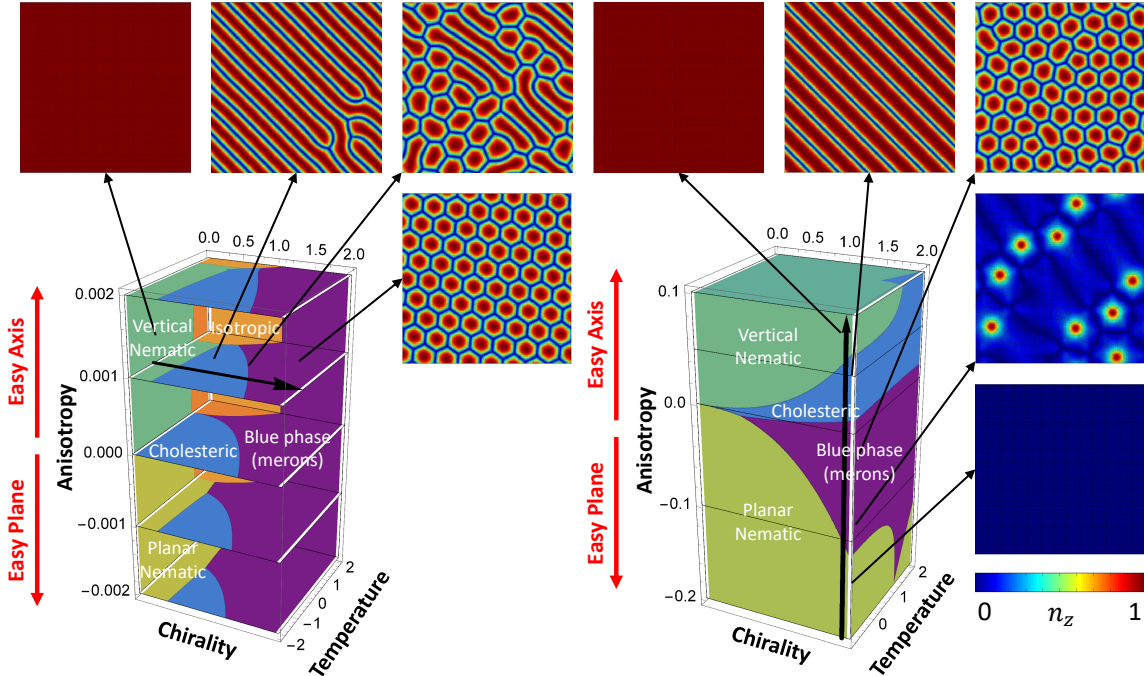
Figure 22: Two views of the phase diagram for chiral liquid crystals in the temperature-chirality-anisotropy space. (Note that the scales on the axes are different in these two visualizations.) The thick horizontal and vertical arrows show the Monte Carlo simulation paths discussed in Sec. 4.3, and the insets show structures calculated by the simulations.

the disclinations between the merons, but these disclinations do not cost too much free energy because the nematic order is fairly soft in this case of high chirality. By contrast, at low temperature and low chirality, the system forms a cholesteric phase. In this structure, there are favorable contributions to the free energy from the optimal magnitude of nematic order and from the single twist of the director field (which is not as favorable as double twist). There are no disclinations, which is reasonable because disclinations cost too much free energy when nematic order is stiff in this case of low chirality.

This phase diagram in the (t, κ) plane is equivalent to the classic phase diagram for blue phases, which has been studied for many years. In previous work, such as Ref. [22], it has been derived by methods that are much more rigorous than those in this section. Here, we see that it is so robust that it occurs even with our very rough approximations.

Now suppose that there is some anisotropy, which may be either easy-axis ($\alpha > 0$) or easy-plane ($\alpha < 0$). We then obtain a 3D phase diagram in the (t, κ, α) space, which is shown using two different 3D visualizations in Fig. 22. (Note that the scales on the axes are different in these two views.) This phase diagram still shows the isotropic, cholesteric, and blue phases. In addition, the vertical nematic phase is stable for large $\alpha > 0$, and the planar nematic phase is stable for large $\alpha < 0$. The transitions between uniform nematic phases and modulated phases (cholesteric or blue) depend mainly on the balance between anisotropy (which favors nematic) and chirality (which favors modulation).

The 3D phase diagram does not show any region in which the skyrmion lattice is stable. At least with this set of rough approximations, the skyrmion lattice never provides the optimum balance among the different contributions to the free energy. Even so, we can still ask: Where in the phase diagram is the skyrmion lattice close to the optimum state? That consideration will at least tell us when skyrmions are likely to be observed as metastable defects, and when they may even be stable if our approximations are not exactly correct (as with surface-induced anisotropy). The answer is that the skyrmion lattice is almost the optimum state for very low chirality κ, near the transition between vertical nematic and cholesteric, which occurs for easy-axis anisotropy $\alpha > 0$. Hence, we can see that the skyrmion lattice and the meron lattice are actually very different types of structures, in spite of the fact that they look somewhat similar. The meron lattice requires high κ, so that the necessary disclinations will not cost too much free energy. The skyrmion lattice requires low κ, so that the nematic order parameter will be stiff against variations.

This analysis can be compared with a recent paper from our group [10], which modeled

skyrmions using a very different theoretical formalism based on a director field (with constant order parameter S) in a 3D cell with strong homeotropic anchoring. That paper found a phase diagram with three structures: vertical nematic, cholesteric, and skyrmion lattice. Although that phase diagram was expressed in terms of different variables, it can be translated into our current variables. The nematic-cholesteric-skyrmion triple point in that phase diagram occurs at $(d/\xi)^2 \sim 10^3$ and $q_0 d \sim 10^{1/2}$, which implies $\alpha \sim (\xi/d)^2 \sim 10^{-3}$ and $\kappa \sim \xi q_0 \sim 10^{-1}$. This result confirms that skyrmions form at low κ, in contrast with merons which form at high κ.

4.3 Numerical Simulations

4.3.1 Equilibrium phases

As an alternative method to minimize the free energy $F_{\text{total}} = F + \Delta F$, we run Monte Carlo (MC) simulations using the Metropolis algorithm. In these simulations, the liquid crystal order is represented by a 3×3 traceless, symmetric tensor $\boldsymbol{Q}$ at each site of a 2D square lattice in the (x, y) plane. In the free energy, all derivatives are approximated by finite differences. We relax the five independent components of $\boldsymbol{Q}$ by simulated annealing from a disordered state for each set of temperature t, chirality κ, and anisotropy α. The states found through this numerical method can then be compared with the states found by the simple analytic assumptions of Sec. 4.2.2.

As a first study, we vary the parameters t and κ, for zero anisotropy $\alpha = 0$, to explore the phase diagram of Fig. 21. At high t, the system is in the isotropic phase, with a highly disordered $\boldsymbol{Q}$ tensor field. At low t and low κ, the simulations show a cholesteric phase, with a lattice of twist walls separating vertically aligned stripes. Because of fluctuations

in the Monte Carlo simulation, the cholesteric order is not perfect, but rather exhibits hairpin defects. At high κ, we find a blue phase, which consists of double-twist tubes or merons, separated by twist walls. At each point where three walls intersect, there is a disclination of topological charge $-1/2$ in the orientational order. These disclinations are points where the eigenvalue associated with the $\hat{z}$ axis becomes dominant and negative in sign, surrounded by biaxial cores, as predicted by Ref. [14]).

For a second comparison, we vary κ from 0.09 to 1.9, with the other two parameters fixed at $t = -0.9$ and $\alpha = 0.001$. This series of simulations moves along the thick arrow in Fig. 22 (left side). A series of simulated structures is shown by the insets around the phase diagram.

At low chirality, the system is in the vertically aligned nematic phase. The director is everywhere parallel to the anisotropy axis, $\hat{n} = \hat{z}$, as indicated by the uniform red color in the figure. When the chirality increases, there is a transition into the cholesteric phase. Because of fluctuations in the simulation, the cholesteric phase shows several dislocations in the stripe pattern, which correspond to disclinations in the orientational order. As the chirality increases further, the density of dislocations increases, and the long stripes of vertical alignment evolve into shorter segments. Eventually the segments shorten into hexagonal cells, which can be regarded as double-twist tubes or merons, separated by twist walls. The transitions among these structures occur quite close to the phase boundaries predicted by the simple analytic assumptions.

For a third comparison, we vary α from -0.2 (easy plane anisotropy) to +0.1 (easy axis anisotropy), with the other parameters fixed at $\kappa = 0.9$ and $t = -0.9$. This series moves along the thick arrow in Fig. 22 (right side), with simulated structures shown by

insets around the phase diagram.

For high easy plane anisotropy, the system is in a horizontally aligned nematic phase, with $\hat{\boldsymbol{n}}$ in the (x, y) plane. The orientation within the plane is random, and it is uniform across the system. When the anisotropy is reduced toward zero, the system begins to show isolated merons, with vertical alignment in the center and double twist of the director going outward. These merons are separated by large regions of $\hat{\boldsymbol{n}}$ in the (x, y) plane, which must include disclinations in the planar director field. As the anisotropy decreases further, the density of merons increases, and they eventually form a hexagonal lattice, which can be regarded as a blue phase. After the anisotropy changes sign, and becomes larger in the easy axis direction, there is a transition into a cholesteric phase, with walls separating vertically aligned stripes. For even larger easy axis anisotropy, the system forms a vertically aligned nematic phase, with a uniform director field. Again, the transitions are generally consistent with the phase boundaries derived from the approximations of Sec. 4.2.2.

4.3.2 Metastable skyrmions

We do not see *stable* skyrmions in the Monte Carlo simulations for any set of parameters in this model. In that respect, the Monte Carlo simulations are once again consistent with the simple analytic calculations of Sec. 4.2.2: One of the other phases is always lower in free energy than the skyrmion lattice.

Although skyrmions are not stable minimum energy states, they can still exist as *metastable* states. To investigate the possibility of metastable skyrmions, we run dynamic simulations of the same model with free energy $F_{\text{total}} = F + \Delta F$, with code

103

running on a graphical processing unit (GPU). In these dynamic simulations, we integrate the Q tensor forward in time, following the relaxational equation $\partial Q_{\alpha\beta}(\boldsymbol{r}, t)/\partial t = -\Gamma \delta F_{\text{total}}/\delta Q_{\alpha\beta}(\boldsymbol{r}, t)$. This equation is not required to conserve skyrmion charge, because the eigenvalues of Q can change in time. However, it normally conserves skyrmion charge, unless the system goes over a significant energy barrier to changing the eigenvalues.

We begin the dynamic simulations with an initial condition corresponding to a circular skyrmion, in which the director is vertical at the center, and it twists by $180°$ going outward to the perimeter. Depending on the energetic parameters, we see three types of shape evolution: (a) If the anisotropy is too large, the skyrmion skrinks and disappears; the final state is vertical nematic. (b) If the anisotropy is too small, the skyrmion expands and evolves into one of the variations of cholesteric stripe patterns that was seen in Monte Carlo simulations. (c) If the anisotropy is within the right range, the initial state relaxes into a metastable skyrmion.

The metastable skyrmion structure has the structure shown in Fig. 23. The director twists by $180°$ from the center to the perimeter, but this twist is not uniform. Rather, the director is almost vertical over some distance from the center and the twist occurs over a short range. Hence, the skyrmion can be regarded as a π-wall that is curved into a ring, with a vertically aligned nematic phase in the interior and the exterior.

The size and shape of a skyrmion are very robust and long-lived. For example, in Fig. 24, if the initial state is a distorted elliptical loop rather than a circle, the skyrmion quickly evolves into a final static circular shape which never breaks down. If two skyrmions are in close proximity, they repel each other until they reach a separation comparable to the skyrmion diameter. Because of this robustness and interaction, a system of many
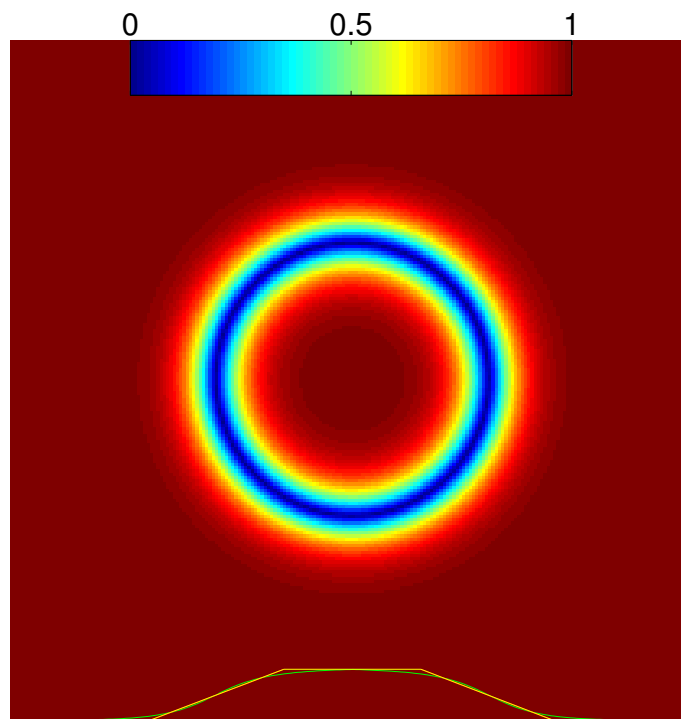
Figure 23: Simulation of a metastable skyrmion, with the color scale indicating $|n_z|$. The yellow line on the bottom shows n_z from -1 to 1, as a function of x, for fixed y in the center. This structure can be regarded as a π-wall that is curved into a ring, with vertical nematic in the interior and the exterior.
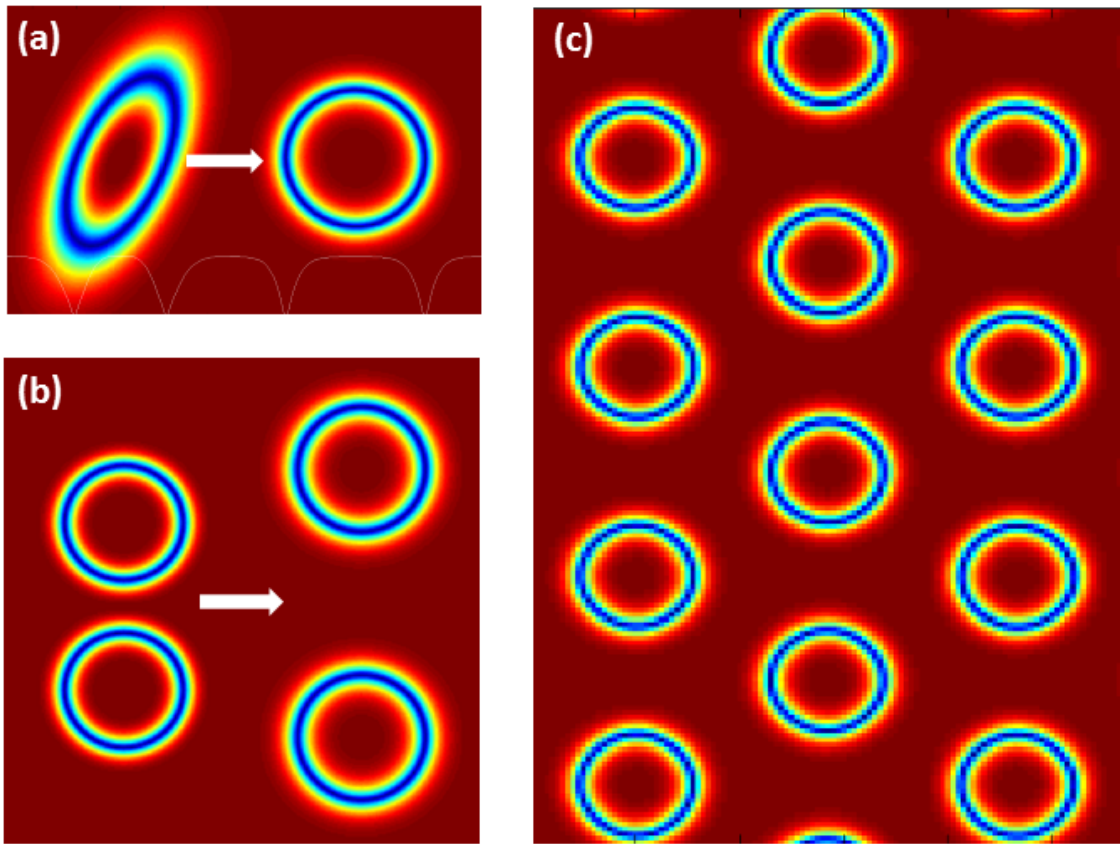
Figure 24: Static skyrmions as particles: (a) An initially distorted shape quickly evolves into a circular ring. (b) Skyrmions repel each other. (c) A system of many skyrmions forms a lattice.

skyrmions forms a lattice, analogously to the crystallization of particles with repulsive interactions.

To understand the metastable skyrmion structure, we represent the director field in cylindrical coordinates as $\hat{\boldsymbol{n}}(r) = -\hat{\boldsymbol{\phi}}\sin(\theta(r)) + \hat{\boldsymbol{z}}\cos(\theta(r))$, and make the linear ansatz for the polar angle

$$\theta(r) = \begin{cases} 0, & \text{for } r \leq r_{\text{in}}, \\[2mm] (r - r_{\text{in}})\pi/\delta r, & \text{for } r_{\text{in}} \leq r \leq r_{\text{out}}, \\[2mm] \pi, & \text{for } r \geq r_{\text{out}}, \end{cases} \tag{89}$$

where r_{in} is the inner radius of the ring, r_{out} is the outer radius, and $\delta r = r_{\text{out}} - r_{\text{in}}$ is the thickness of the wall. As in the calculations of Sec. 4.2.2, we calculate the free energy for this configuration using $Q_{ij} = S(\frac{3}{2}n_i n_j - \frac{1}{2}\delta_{ij})$, and we subtract the background energy of the vertical nematic phase. We then make the substitution $g = r_{\text{in}}/\delta r$, to obtain a skyrmion free energy as a function of g and δr. Minimization with respect to δr yields

$$\delta r = \frac{3\pi L q_0 S}{\Delta\epsilon E^2}, \tag{90}$$

showing that the wall thickness is determined by the competition between Frank elastic constant (which favors a thicker wall) and anisotropy (which favors a thinner wall). The skyrmion free energy, relative to vertical nematic, then becomes

$$F = \frac{9\pi L S^2}{4}\left[\pi^2\left(1 - \frac{3L q_0^2 S}{\Delta\epsilon E^2}\right)(1 + 2g) + \log\left(1 + \frac{1}{g}\right)\right.$$
$$+ \cos(2\pi g)\left[\text{Ci}(2\pi g) - \text{Ci}(2\pi(g+1))\right]$$
$$\left.+ \sin(2\pi g)\left[\text{Si}(2\pi g) - \text{Si}(2\pi(g+1))\right]\right], \tag{91}$$

107

where Ci and Si are the cosine integral and sine integral functions, respectively.

To minimize the skyrmion free energy over g, we rewrite the equation $\partial F/\partial g = 0$ as

$$
\begin{aligned}
\frac{3Lq_0^2 S}{\Delta\epsilon E^2} &= 1 - \frac{1}{\pi}\sin(2\pi g)\left[\mathsf{Ci}(2\pi g) - \mathsf{Ci}(2\pi(g+1))\right] \\
&\quad + \frac{1}{\pi}\cos(2\pi g)\left[\mathsf{Si}(2\pi g) - \mathsf{Si}(2\pi(g+1))\right].
\end{aligned}
\tag{92}
$$

This equation has a solution provided that the ratio on the left side is between the minimum value

$$
\lim_{g\to 0}\frac{3Lq_0^2 S}{\Delta\epsilon E^2} = 1 - \frac{\mathsf{Si}(2\pi)}{\pi} \approx 0.55
\tag{93}
$$

and the maximum value

$$
\lim_{g\to\infty}\frac{3Lq_0^2 S}{\Delta\epsilon E^2} = 1.
\tag{94}
$$

Equivalently, the range of anisotropy must be

$$
3Lq_0^2 S \leq \Delta\epsilon E^2 \leq 5.5 Lq_0^2 S.
\tag{95}
$$

Within that range, skyrmions are metastable with a characteristic radius given by $r_{\mathsf{in}} = g\delta r$. For anisotropy below the lower limit of that range, the skyrmion radius will grow to infinity. For anisotropy above the upper limit, a skyrmion will shrink and disappear.

This model for metastable skyrmions is qualitatively consistent with the simulations, which also find that metastable skyrmions can exist over a certain range of anisotropy. As a further quantitative comparison, we plot the model calculations compared with simulation results for skyrmion wall thickness δr and average radius $r_{\mathsf{av}} = \frac{1}{2}(r_{\mathsf{in}} + r_{\mathsf{out}})$ as functions of the anisotropy $\Delta\epsilon E^2$ in Fig. 25. The wall thickness calculations are in good agreement with simulation results over the full range of anisotropy that was simulated. The average radius calculations are close to the simulation results for high anisotropy

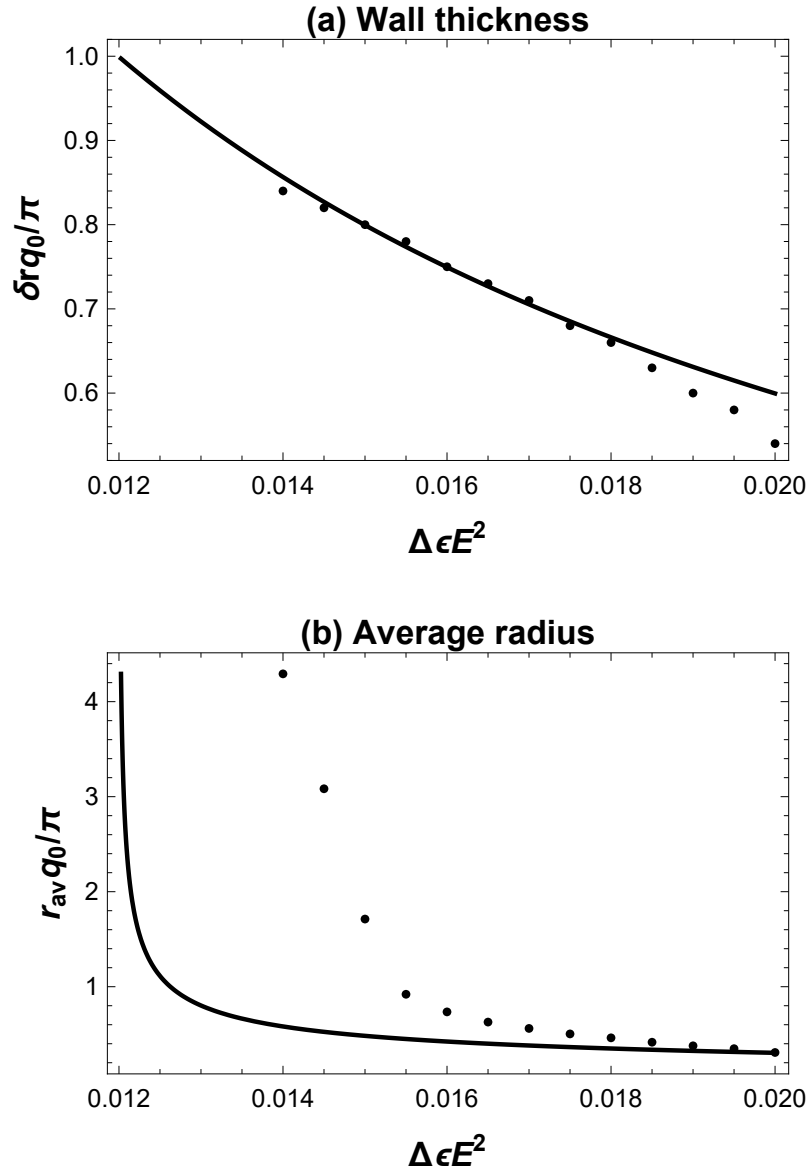**Figure 25:** Skyrmion wall thickness δr and average radius $r_{av} = \frac{1}{2}(r_{in} + r_{out})$, as functions of the anisotropy $\Delta \epsilon E^2$, in units of $\pi/q0$. The points represent simulation results, and the solid lines are the calculation in Sec. 4.3.2. Parameters are $L = 0.001$, $q_0 = \pi$, and $S = 0.405$.
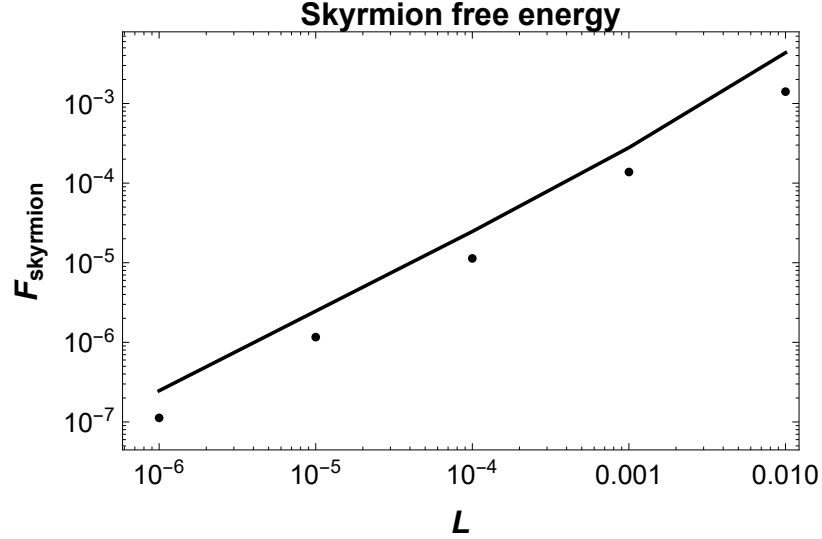
Figure 26: Skyrmion free energy relative to the vertical nematic state, in arbitrary units. The elastic constant L is varied for fixed $a = -0.1$, $b = -3$, and $c = 3$, with the anisotropy $\Delta\epsilon E^2$ adjusted to maintain the skyrmion size (g and δr). The points represent simulation results, and the the solid line is the calculation of Sec. 4.3.2 for the same L and $\Delta\epsilon E^2$.

and small radius, where the simulated skyrmion is circular in shape. However, for low anisotropy and large radius, there is a significant discrepancy; the model underestimates the minimum value of $\Delta\epsilon E^2$ for skyrmion stability. This discrepancy seems to be caused by the shape of the skyrmions; the simulated skyrmion develops a four-fold anisotropy in this limit, perhaps because of the underlying lattice model. Despite the latter discrepancy, the model generally provides a good estimate for the skyrmion size and the range of anisotropy needed for skyrmion stability.

For another comparison, we consider the free energy of a skyrmion, relative to the vertical nematic state. This free energy difference is positive, indicating that skyrmions are metastable in this model. To determine the magnitude of this difference in the simulation, we vary the elastic constant L along the border of the vertical nematic and cholesteric phases. For each L, we adjust the anisotropy $\Delta\epsilon E^2$ so that the size of the skyrmion is roughly the same. In other words, the g and δr values are the same across simulations of

different L values. The simulation results for free energy, relative to vertical nematic, are shown by the points in Fig. 26. By comparison, the calculation of Eq. (91) for the same L and $\Delta\epsilon E^2$ is shown by the solid line in the same figure. These results are consistent up to a factor of 2, which is reasonable for such an approximate model.

As noted in the Introduction, many experiments have studied skyrmions in confined cholesteric liquid crystals [4–11]. These experiments generally cannot determine whether skyrmions are metastable, as predicted by the calculations in this section, or whether they are actually stable structures. Indeed, that issue may depend on the exact form of the anisotropy, which can arise from an applied electric field or from homeotropic anchoring on surfaces. Regardless of whether skyrmions are metastable or stable, they are separated from the uniform vertical state by a large energy barrier, and hence require significant disturbances in order to form or decay. These skyrmions occur in liquid crystals with stiff nematic order, in contrast with blue phases (meron lattices), which occur in liquid crystals with soft nematic order or high chirality.

4.4 Theory of chiral magnets

In recent years, many investigators have done substantial theoretical research on modulated structures in chiral magnets, as in Refs. [16–21]. In this section, we briefly review that work in a notation similar to the notation for chiral liquid crystals. We then use this theory to compare magnetic skyrmions and merons with the analogous structures in liquid crystals.

A fundamental difference between liquid crystals and magnets is that liquid crystals are described by the tensor order parameter $Q_{\alpha\beta}(\boldsymbol{r})$, while magnets are described by the

vector order parameter $M_\alpha(\boldsymbol{r})$. In Landau theory, the bulk free energy density of a chiral magnet can be written as

$$\begin{aligned} F \quad = \quad & \frac{1}{2}a|\boldsymbol{M}|^2 + \frac{1}{4}c|\boldsymbol{M}|^4 + \frac{1}{2}k(\partial_i M_j)(\partial_i M_j) \\ & + kq_0\epsilon_{lik}M_l\partial_i M_k - HM_z - AM_z^2. \end{aligned} \tag{96}$$

Here, the first two terms represent the free energy of a uniform system, expanded in powers of the vector order parameter. These terms favor a certain magnitude $|\boldsymbol{M}|$ of the magnetic order. The quadratic coefficient a is assumed to vary linearly with temperature, while c is assumed constant with respect to temperature. The third and fourth terms represent the elastic free energy associated with variations of $\boldsymbol{M}$ as a function of position. The third term penalizes all variations in $\boldsymbol{M}$, while the fourth is a Dzyaloshinskii-Moriya term that favors certain twist deformations because of the Dresselhaus spin-orbit coupling. The last two terms involve two distinct types of symmetry-breaking fields acting on the magnetic order. The H term is a standard magnetic field in the z direction, which couples linearly to $\boldsymbol{M}$, while the A term is a crystalline anisotropy, which couples quadratically to $\boldsymbol{M}$. The anisotropy may be easy-axis with $A > 0$, or easy-plane with $A < 0$.

Equation (96) for the magnetic free energy is quite analogous to Eq. (74) for the liquid crystal free energy, but there are two important distinctions. First, the bulk free energy for the liquid crystal has quadratic, cubic, and quartic terms, while the bulk free energy of the magnet has only quadratic and quartic terms. Second, the liquid crystal has only a quadratic anisotropy acting on the order parameter, while the magnet has both a linear field and a quadratic anisotropy. Both of these distinctions arise from the tensor vs. vector nature of the order parameter.

By analogy with the liquid crystal theory, we can simplify the magnetic theory by rescaling parameters. Here, the characteristic value of the magnetic order parameter is $M \sim (|a|/c)^{1/2}$, the free energy density of the ferromagnetic relative to disordered phase is $F \sim a^2/c$, and the core radius of a vortex in magnetic order is $\xi \sim (k/|a|)^{1/2}$. Hence, we rescale $\boldsymbol{M}$, F, and all lengths by those characteristic values. The theory then depends on three dimensionless ratios, which we write as

$$\kappa = q_0 \sqrt{\frac{k}{|a|}}, \qquad h = H\sqrt{\frac{c}{a^3}}, \qquad \alpha = \frac{A}{|a|}. \tag{97}$$

As in the liquid crystal case, the parameter κ is a dimensionless chirality, which represents the natural twist q_0 relative to the disclination core radius ξ. Equivalently, κ^2 can be interpreted as the energy scale of the favored chiral twist relative to the energy scale associated with changing the magnitude of $\boldsymbol{M}$ inside a defect core. Low κ can be called "low chirality" or "stiff magnetic order," while high κ can be called "high chirality" or "soft magnetic order." The parameters h and α are dimensionless versions of the field and anisotropy. The anisotropy α is analogous to the anisotropy in the liquid crystal case, while the field h does not exist in the liquid crystal.

The magnetic system does not have a temperature parameter t analogous to the liquid crystal case. Because the magnetic free energy density includes quadratic and quartic but not cubic terms in $\boldsymbol{M}$, the temperature scales out of the magnetic case, leaving a problem with no explicit dependence on the temperature-dependent coefficient a (assuming that $a < 0$ so that the system is in an ordered phase).

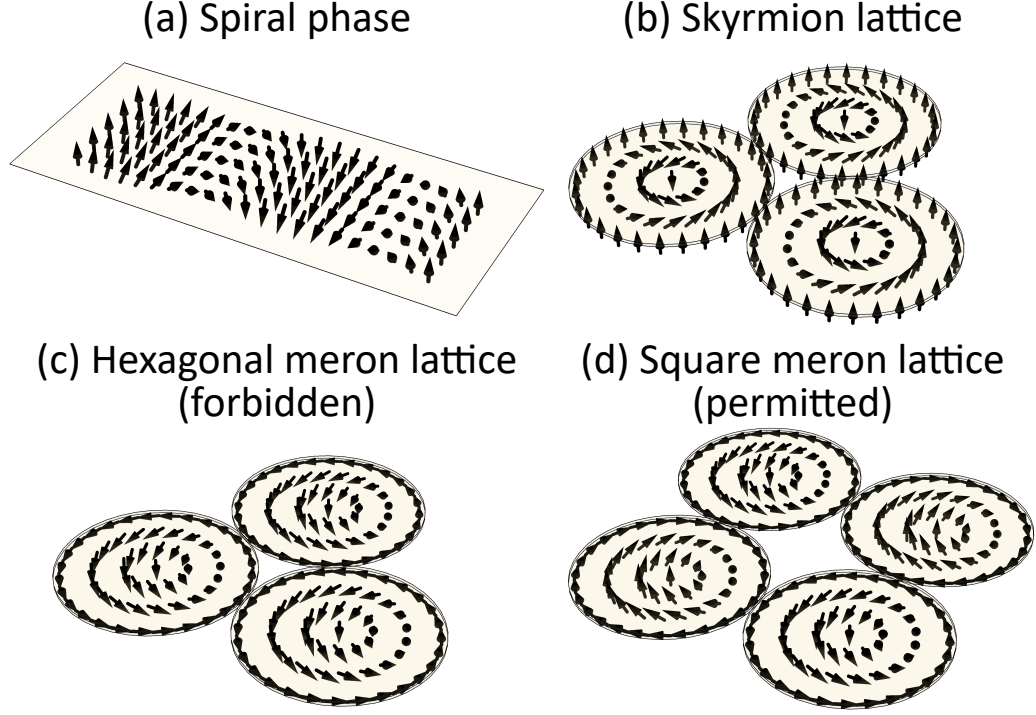Many investigators have already studied the phases of this model through detailed

(a) Spiral phase

(b) Skyrmion lattice

(c) Hexagonal meron lattice (forbidden)

(d) Square meron lattice (permitted)

Figure 27: Structure of the modulated magnetic phases studied in this work.

numerical simulations. We suggest that key features of the phase diagram can be understood through simple analytic calculations, analogous to the liquid crystal calculations in Sec. 4.2.2. Hence, we repeat those calculations for the magnetic case, and compare the results with simulations from the literature.

For these simple analytic calculations, we consider the following phases:

a. Vertical ferromagnetic phase The system has uniform magnetic order in the z direction, with $\mathbf{M} = M\hat{\mathbf{z}}$. After minimizing over M, the scaled free energy density is $\tilde{F}_{\text{vert}} = -\frac{1}{4} - h - \alpha$.

b. Tilted ferromagnetic phase The magnetic order is given by $\mathbf{M} = M[\hat{\mathbf{x}}\sin\theta + \hat{\mathbf{z}}\cos\theta]$, and the scaled free energy density is $\tilde{F}_{\text{tilt}} = -\frac{1}{4} - h\cos\theta - \alpha\cos^2\theta$. The tilt θ is determined by the competition between h and α.

114

c. *Spiral phase*   The spiral phase of magnetic systems has the structure shown in Fig. 27(a), analogous to the cholesteric phase of liquid crystals. If h and α are zero, the modulated structure is $\boldsymbol{M}(x) = M[-\hat{\boldsymbol{x}}\sin(\pi x/d) + \hat{\boldsymbol{z}}\cos(\pi x/d)]$. If h and α are small but nonzero, the structure is only slightly distorted, so that expression can still be used as a first approximation. After minimizing over M and d, the average scaled free energy density is $\tilde{F}_{\text{spiral}} = -\frac{1}{4}(1+\kappa^2)^2 - \frac{1}{2}\alpha(1+\kappa^2)$.

d. *Skyrmion lattice*   Skyrmions are modeled by disks arranged in a hexagonal lattice, as in Fig. 27(b). Within each disk, the magnetic order twists through an angle of π, from downward at the center to upward at the edge. Our linear assumption for this variation is $\boldsymbol{M}(r) = M[-\hat{\boldsymbol{\phi}}\sin(2\pi r/d) + \hat{\boldsymbol{z}}\cos(2\pi r/d)]$, for $0 \leq r \leq d/2$. Between the disks, the magnetic order is uniform and upward. After minimizing over M and d, the average scaled free energy density is $\tilde{F}_{\text{skyrm}} = -\frac{1}{4} - 0.36\kappa^2 - 0.15\kappa^4 - 0.093h - 0.37h(1+0.80\kappa^2)^{1/2} - 0.55\alpha - 0.36\alpha\kappa^2$.

e. *Meron lattice*   Merons are modeled by disks with a twist of $\pi/2$ from the center to the edge. These disks *cannot* be arranged in a hexagonal lattice, as shown in Fig. 27(c), because the magnetic order parameter would be incompatible at each point where two disks meet. In that respect, the vector order parameter for a magnet is quite different from the tensor order parameter for a liquid crystal. As an alternative, merons *can* be arranged in a square lattice, shown in Fig. 27(d). In this structure, there is a regular alternation of merons with the central $\boldsymbol{M}$ pointing upward or downward. Our linear assumption for the variation within each disk is $\boldsymbol{M}(r) = M[-\hat{\boldsymbol{\phi}}\sin(\pi r/d) + \hat{\boldsymbol{z}}\cos(\pi r/d)]$, for $0 \leq r \leq d/2$. In each region between four disks, the magnetic order has a vortex of topological charge
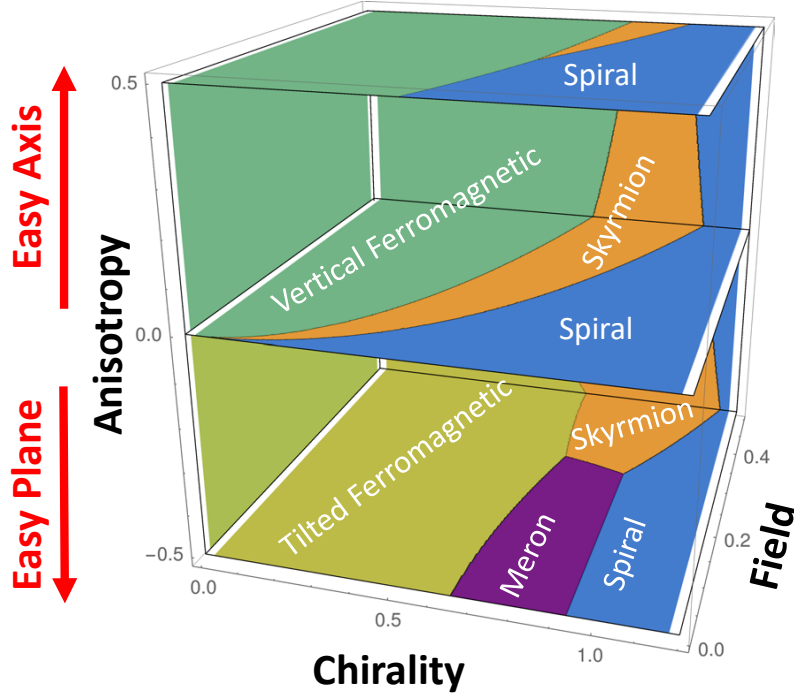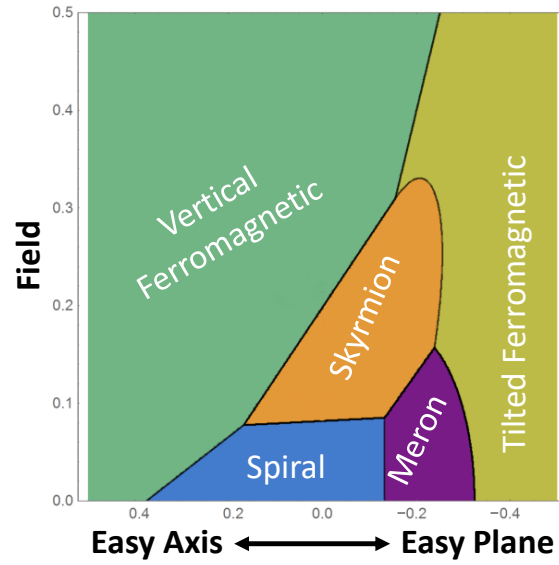
Figure 28: Visualization of the phase diagram for chiral magnets in the chirality-field-anisotropy space.

-1, which we model as a disordered, isotropic region. After minimizing over M and d, the average scaled free energy density is $\tilde{F}_{\text{meron}} = -\frac{1}{4} - 0.36\kappa^2 - 0.11\kappa^4 - 0.23\alpha - 0.28\alpha\kappa^2$.

By comparing the free energies of these structures, we construct a 3D phase diagram in the chirality-field-anisotropy space, as shown in Fig. 28. In the limit of low chirality, the system forms a ferromagnetic phase, which is vertical for large easy-axis anisotropy and tilted for large easy-plane anisotropy. In the limit of high chirality, the system forms a spiral phase. The more complex skyrmion and meron lattices occur for intermediate chirality. In this intermediate regime, easy-plane anisotropy favors the meron lattice, because this lattice has large planar regions. A field favors the skyrmion lattice, because it has a predominant vector orientation which can align with the field.

Instead of performing our own simulations, we can compare the results of these rough
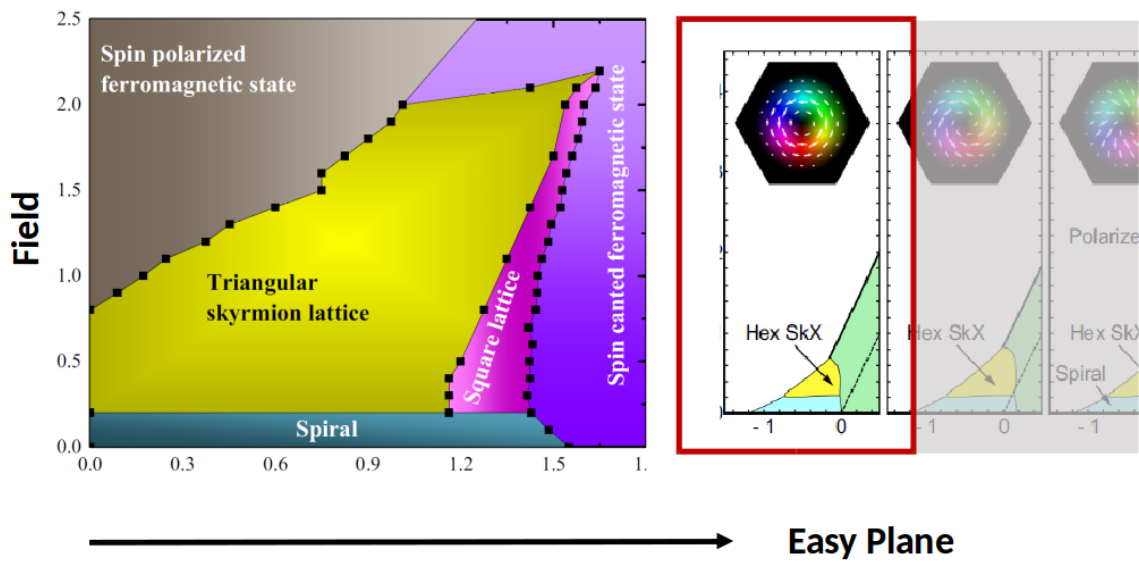
Figure 29: (a) Cross section of the phase diagram for chiral magnets in the field-anisotropy plane for fixed chirality $\kappa = 0.5$. (b) Phase diagrams obtained through simulations by Ref. [25](left), and Ref. [30](right)

analytic arguments with previously published simulations by other investigators. As examples, Refs. [25] and [30] both present phase diagrams for magnetic structures in the field-anisotropy plane, which can be compared with a cross section of our phase diagram for fixed chirality $\kappa = 0.5$, as shown in Fig. 29. We can see the same general arrangement of the phases in Fig. 7 of Ref. [25], and in Fig. 1 (left) of Ref. [30], which are reproduced in Fig. 29. (As a matter of terminology, the polarized ferromagnetic phase is equivalent to what we have called vertical ferromagnetic, and canted ferromagnetic is equivalent to what we have called tilted.) Hence, we can see that the rough analytic arguments of this section capture key features of the free energy balance among the phases, even without the need to do detailed numerical simulations.

4.5 Discussion

The work presented in this article enables us to compare skyrmions with merons, and also to compare chiral liquid crystals with chiral magnets.

To compare skyrmions with merons, we see that these structures are similar from the perspective of local geometry near the defect core: They both have the same double-twist structure in the orientational order. However, they are quite different from the perspective of global topology: Around a skyrmion, the orientational order goes to the same vertical orientation everywhere. Hence, it is possible to pack many skyrmions together with uniform regions in between. The whole lattice of skyrmions is nonsingular, with approximately uniform magnitude of orientational order (uniform eigenvalues of Q for a liquid crystal, uniform $|M|$ for a magnet). By contrast, around a meron, the orientational order goes to a horizontal orientation, and it covers the full range of all possible horizontal

orientations. Hence, it is not possible to pack many merons together with uniform regions in between. Rather, there must be singularities in the orientational order between the merons. Hence, a lattice of merons can only form if the energetic cost of forming these singularities is not too great.

Because skyrmions are surrounded by uniform vertical orientational order, they can be regarded as local excitations. Hence, skyrmions move and interact as effective particles, with only a short-range potential between them. Conversely, because merons are surrounded by the full range of nonuniform horizontal orientational order, they are more complex nonlocal excitations, which have long-range logarithmic interactions, and which must be accompanied by other defects, This distinction in locality has been pointed out in the magnetic context [20], and it applies also in the liquid crystal context.

To compare chiral liquid crystals with chiral magnets, we see that these materials are similar from the perspective of topology: They both can form skyrmions and merons. However, chiral liquid crystals and chiral magnets are quite different from the perspective of energetics: In chiral magnets, it is straightforward to stabilize skyrmions by applying a magnetic field, which couples linearly to M and stabilizes the orientation outside the skyrmions, in contrast with the orientation inside the skyrmions. Hence, a lattice of skyrmions becomes the ground state for an appropriate choice of field and anisotropy. By contrast, in chiral liquid crystals have a tensor order parameter Q, so there is no field that can distinguish between orientational order upward or downward; there is only a quadratic easy-axis or easy-plane anisotropy. As a result, the specific model studied here does not have skyrmions as a ground state; it only has skyrmions as metastable defects. To be sure, variations on this liquid-crystal model (perhaps with anisotropy arising from surface

anchoring) might have skyrmions as a ground state, as in Ref. [10]. Even so, they are stabilized by a fairly delicate balance of free energies, not by the simple field as in the magnetic case. Thus, we would say that the vector order parameter of magnets tends to favor skyrmions, while the tensor order parameter of liquid crystals tends to disfavor skyrmions.

In chiral liquid crystals, the formation of merons in a hexagonal lattice requires singularities of topological charge $-1/2$ between the merons. In "high-chirality" liquid crystal materials, the energetic cost of these singularities is not too large compared with the energetic benefit of the double-twist regions. Hence, it is straightforward to stabilize meron lattices in liquid crystals. Such lattices are called blue phases, and they have been studied extensively for many years. In 3D liquid crystals, blue phases normally have a more complex cubic structure rather than the 2D lattice considered here, but still the same principles apply. By contrast, in chiral magnets, the formation of merons in a square lattice requires singularities of the larger topological charge -1 between the merons. It is theoretically possible for this structure to be the ground state, but it is difficult to find parameters where the energetic cost of the singularities is less than the energetic benefit of the double-twist regions. Thus, we would say that the tensor order parameter of liquid crystals tends to favor merons, while the vector order parameter of magnets tends to disfavor merons.

BIBLIOGRAPHY

[1] R. D. Kamien and J. V. Selinger, "Order and frustration in chiral liquid crystals," *J. Phys. Condens. Matter*, vol. 13, no. 3, pp. R1–R22, 2001.

[2] P. Oswald and P. Pieranski, *Nematic and Cholesteric Liquid Crystals: Concepts and Physical Properties Illustrated by Experiments*. CRC Press, 2005.

[3] I. I. Smalyukh, B. I. Senyuk, P. Palffy-Muhoray, O. D. Lavrentovich, H. Huang, E. C. Gartland, V. H. Bodnar, T. Kosa, and B. Taheri, "Electric-field-induced nematic-cholesteric transition and three-dimensional director structures in homeotropic cells," *Phys. Rev. E*, vol. 72, p. 061707, Dec 2005.

[4] A. N. Bogdanov and A. A. Shestakov, "Inhomogeneous two-dimensional structures in liquid crystals," *J. Exp. Theor. Phys.*, vol. 86, no. 5, pp. 911–923, 1998.

[5] A. N. Bogdanov, U. K. Rößler, and A. A. Shestakov, "Skyrmions in nematic liquid crystals," *Phys. Rev. E*, vol. 67, p. 016602, Jan 2003.

[6] J.-i. Fukuda and S. Žumer, "Quasi-two-dimensional Skyrmion lattices in a chiral nematic liquid crystal," *Nat. Commun.*, vol. 2, p. 246, 2011.

[7] P. J. Ackerman, R. P. Trivedi, B. Senyuk, J. van de Lagemaat, and I. I. Smalyukh, "Two-dimensional skyrmions and other solitonic structures in confinement-frustrated chiral nematics," *Phys. Rev. E*, vol. 90, p. 012505, Jul 2014.

[8] A. O. Leonov, I. E. Dragunov, U. K. Rößler, and A. N. Bogdanov, "Theory of skyrmion states in liquid crystals," *Phys. Rev. E*, vol. 90, p. 042502, Oct 2014.

[9] Y. Guo, S. Afghah, J. Xiang, O. D. Lavrentovich, R. L. B. Selinger, and Q.-H. Wei, "Cholesteric liquid crystals in rectangular microchannels: skyrmions and stripes," *Soft Matter*, vol. 12, pp. 6312–6320, 2016.

[10] S. Afghah and J. V. Selinger, "Theory of helicoids and skyrmions in confined cholesteric liquid crystals," *Phys. Rev. E*, vol. 96, p. 012708, Jul 2017.

[11] P. J. Ackerman, T. Boyle, and I. I. Smalyukh, "Liquid crystal skyrmions can swim," Jun 2017.

[12] B. G.-g. Chen, P. J. Ackerman, G. P. Alexander, R. D. Kamien, and I. I. Smalyukh, "Generating the hopf fibration experimentally in nematic liquid crystals," *Phys. Rev. Lett.*, vol. 110, p. 237801, Jun 2013.

[13] P. J. Ackerman and I. I. Smalyukh, "Diversity of knot solitons in liquid crystals manifested by linking of preimages in torons and hopfions," *Phys. Rev. X*, vol. 7, p. 011006, Jan 2017.

[14] N. Schopohl and T. J. Sluckin, "Defect core structure in nematic liquid crystals," *Phys. Rev. Lett.*, vol. 59, pp. 2582–2584, Nov 1987.

[15] T. H. R. Skyrme, "A Unifield Field Theory of Mesons and Baryons," *Nucl. Phys.*, vol. 31, no. 4, pp. 556–569, 1962.

[16] U. K. Rößler, A. N. Bogdanov, and C. Pfleiderer, "Spontaneous skyrmion ground states in magnetic metals," *Nature*, vol. 442, pp. 797–801, 2006.

[17] S. Mühlbauer, B. Binz, F. Jonietz, C. Pfleiderer, A. Rosch, A. Neubauer, R. Georgii, and P. Böni, "Skyrmion lattice in a chiral magnet," *Science*, vol. 323, no. 5916, pp. 915–919, 2009.

[18] X. Z. Yu, Y. Onose, N. Kanazawa, J. H. Park, J. H. Han, Y. Matsui, N. Nagaosa, and Y. Tokura, "Real-space observation of a two-dimensional skyrmion crystal," *Nature*, vol. 465, pp. 901–904, 2010.

[19] S.-Z. Lin, C. Reichhardt, C. D. Batista, and A. Saxena, "Particle model for skyrmions in metallic chiral magnets: Dynamics, pinning, and creep," *Phys. Rev. B*, vol. 87, p. 214419, Jun 2013.

[20] N. Nagaosa and Y. Tokura, "Topological properties and dynamics of magnetic skyrmions," *Nat. Nanotechnol.*, vol. 8, pp. 899–911, 2013.

[21] S. Banerjee, J. Rowland, O. Erten, and M. Randeria, "Enhanced stability of skyrmions in two-dimensional chiral magnets with rashba spin-orbit coupling," *Phys. Rev. X*, vol. 4, p. 031045, Sep 2014.

[22] H. Grebel, R. M. Hornreich, and S. Shtrikman, "Landau theory of cholesteric blue phases," *Phys. Rev. A*, vol. 28, pp. 1114–1138, Aug 1983.

[23] R. M. Hornreich and S. Shtrikman, "Field-induced hexagonal blue phases in positive and negative dielectric anisotropy systems: Phase diagrams and topological properties," *Phys. Rev. A*, vol. 41, pp. 1978–1989, Feb 1990.

[24] J.-i. Fukuda, M. Yoneya, and H. Yokoyama, "Simulation of cholesteric blue phases using a landauˇde gennes theory: Effect of an applied electric field," *Phys. Rev. E*, vol. 80, p. 031706, Sep 2009.

[25] S.-Z. Lin, A. Saxena, and C. D. Batista, "Skyrmion fractionalization and merons in chiral magnets with easy-plane anisotropy," *Phys. Rev. B*, vol. 91, p. 224407, Jun 2015.

[26] R. B. Meyer and P. S. Pershan, "Surface polarity induced domains in liquid crystals," *Solid State Commun.*, vol. 13, no. 7, pp. 989 – 992, 1973.

[27] O. D. Lavrentovich and V. M. Pergamenshchik, "Patterns in thin liquid crystal films and the divergence ("surfacelike") elasticity," *Int. J. Mod. Phys. B*, vol. 9, no. 18n19, pp. 2389–2437, 1995.

[28] G. P. Alexander and J. M. Yeomans, "Flexoelectric blue phases," *Phys. Rev. Lett.*, vol. 99, p. 067801, Aug 2007.

[29] S. M. Shamid, D. W. Allender, and J. V. Selinger, "Predicting a polar analog of chiral blue phases in liquid crystals," *Phys. Rev. Lett.*, vol. 113, p. 237801, Dec 2014.

[30] J. Rowland, S. Banerjee, and M. Randeria, "Skyrmions in chiral magnets with rashba and dresselhaus spin-orbit coupling," *Phys. Rev. B*, vol. 93, p. 020404, Jan 2016.

CHAPTER 5

Moving Skyrmions

5.1 Introduction

In magnetic systems, extensive research has investigated skyrmion motion, which is achieved by small electric currents [1,2]. Similarly, in liquid crystals, recent experiments [3–5] demonstrate that skyrmions can be moved by fluid flow, light, and electric fields. In the previous chapter, we developed analytic and numerical methods, including Monte Carlo and relaxational dynamics simulations, to model the particle-like motion and interaction of liquid crystal skyrmions. A natural question that follows is how can we numerically study the actuation of skyrmions.

In this chapter we investigate various mechanisms of actuation for 2D and 3D skyrmions. First, we determine the effect of electric field changes on skyrmion shape, and demonstrate that field gradients can induce skyrmion motion. Next, we consider the exposure of certain liquid crystals to light which changes the helical pitch. To model the effect of such pitch changes, we apply gradients in the natural twist and find that these gradients also induce skyrmion motion. These results regarding electric fields and light are in qualitative agreement with experiments. Finally, we show that nonuniform surface anchoring can also be used to manipulate skyrmion motion.

5.2 Skyrmion Shape and Electric Field

The skyrmions in our model are stabilized by a background electric field in the direction perpendicular to the plane of the material, i.e. the z axis. There is a range of electric field, depending on chirality, over which the skyrmions are static and the size of the skyrmion depends on the strength of the field and the dielectric anisotropy of the material. For skyrmions we realize in 2D, easy-axis alignment is needed to stabilize the skyrmions, so the anisotropy has a positive sign. The size and shape is very sensitive to the field, thus there is no wide range that the field can change over without breaking the skyrmions. However, we can first get the static skyrmions by tuning the parameters, and then small additional fields can be used to fine tune the size and shape.

The most straightforward way of controlling the size is by varying the field in the z direction. Figure 30 shows simulation results for skyrmions in different types of fields. The first image labeled *normal* shows a static skyrmion in a background field. As we showed in the previous chapter a stronger background field in the z direction yields a smaller skyrmion radius. Thus, a small extra field in the direction of the background field, assuming $+z$ direction, increases the magnitude of E and makes the skyrmion shrink. On the contrary, if we add a small field in $-z$ direction the skyrmion will expand.

Adding a small in-plane field distorts the circular shape into an oval one. The distortion is along the axis of the extra field. For instance if we add a small field in the x direction the skyrmions is alongated along the x axis and the overall size grows slightly. Similar behavior is also observed for a field in the y direction.

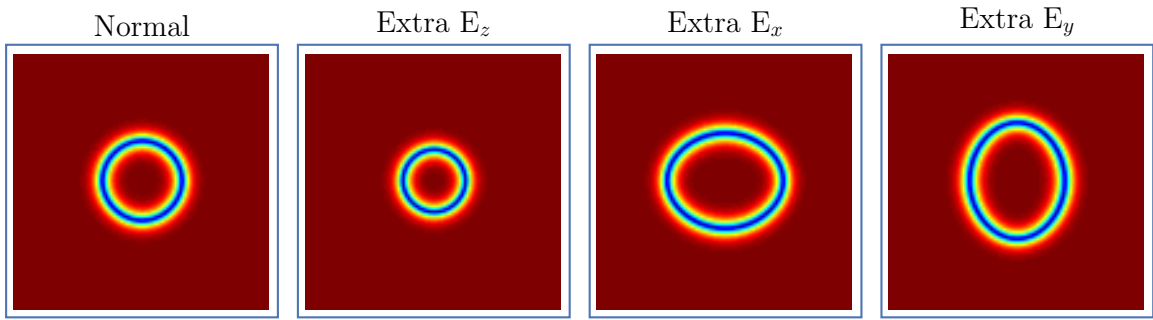We note that in all of these cases, too big of a field (any extra field comparable

125

Figure 30: Skyrmions' shape depending on extra electric field.

to the background field) will destroy the skyrmion because the shape is sensitive to the field (see Fig. 25 of the previous chapter). Such a change of the field in any of the directions mentioned will move the parameters to a different phase in the phase diagram. The evolution of the skyrmion shape in the process will depend on the type of alignment favored by the extra field. If it favors easy-axis alignment then the skyrmion will shrink and disappear. If it favors easy-plane alignment then the skyrmion will expand and form either cholesteric stripes or merons depending on how big the field is (see the phase diagram in Fig. 22 of the previous chapter). The expansion will be radially symmetrical for extra E_z and in the direction of the field for extra $E_\perp$.

5.3   Actuation by Electric Field

5.3.1   Extra E_z

Now consider the same 2D skyrmion in the background field where the dielecric anisotropy has to be positive. We apply a strong field in the z direction within a spot near the skyrmion (green spot in Fig. 31). Within the spot, the tendency of molecules to align vertically will be much greater. When the spot in part (a) is moved towards the skyrmion border, it will cause the center of the π-wall (blue belt) to shift away because
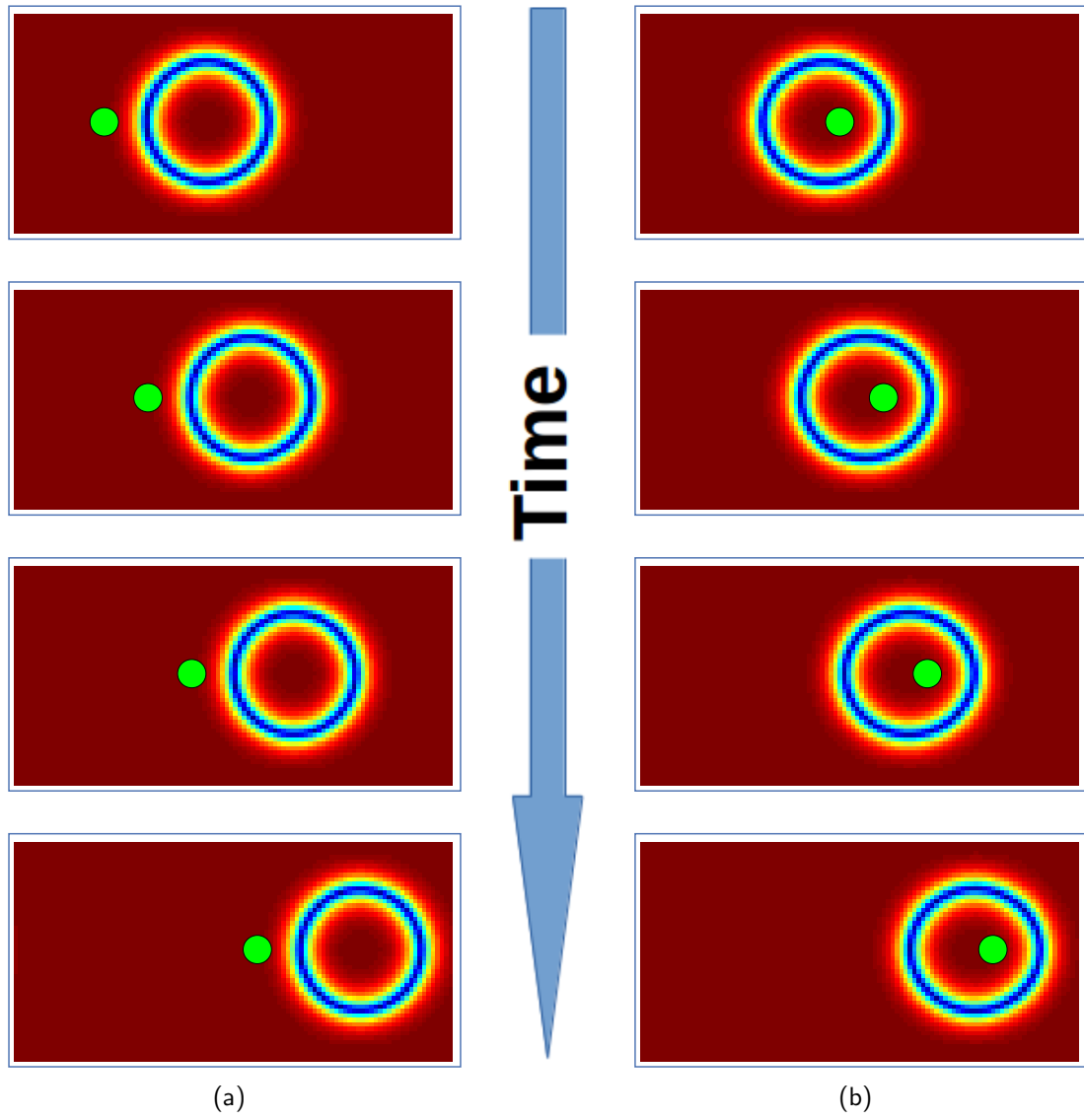
Figure 31: Skyrmions moved by extra E_z

the extra field, as it penetrates the skyrmion, will align the inner layers more vertically. To maintain the gradients needed to minimize the free energy, the inner layers will follow the outer layers' rotation towards the vertical axis. This effect will be translated towards the inner regions of the wall resulting in a shift of all the director orientations.

Figure 31 shows two different ways extra E_z can drive translation of the skyrmion. If the green spot with extra E_z is placed inside the skyrmion and moved it will push away the more horizontal part (blue ring) of the skyrmion away. The skyrmion, in this case also, quickly adapts to the change and is dragged via the spot. Experimentally, it might be easier to achieve a spot with field outside the skyrmion. In both cases the skyrmion can be moved in a controlled fashion but the motion of the green spot must be slow enough for the skyrmion shape to adapt as moving the spot too fast will *break* the skyrmion and cause it to *pop.* We will speak more about the popping of the skyrmion in the upcoming sections.

This feature of the extra vertical field can be employed in different ways. For example fixed or movable walls made of strong E_z can be built to confine skyrmions or guide their motion. We can put many skyrmions between confining walls and see the effect of compression. If we would like to destroy a skyrmion for some functional reason we can cut through it with quick motion of the spot which is not possible with real particles.

5.3.2   Extra $E_\perp$

Now we consider a spot in which we apply a field in the x-y plane. This type of field also can move the skyrmions (Fig. 32-a). The field in this spot aligns the local director parallel to the extra field in contrast with vertical alignment by extra E_z. Favoring horizontal

alignment in the spot results in two features. First we see that it attracts the blue circle and pulls it rather than push. The skyrmion shape is again robust and it follows the motion of the spot.

Another feature of extra $E_\perp$ is that the rotation of the field in the spot is followed by the rotation of the skyrmion (Fig. 32-b). This indeed is very useful because due to the symmetry of the shape it is hard to rotate the skyrmions by external forces or by means of other skyrmions but a horizontal field can easily catch and rotate them. A design possibly easier to achieve experimantally is a line field rather than a spot which will serve the same purpose.

5.3.3 Smooth Gradient of Electric Field

Variable electric field can also be used for actuation. To demonstrate this effect we place a skyrmion in a background field and add a small field with spatial variation. For example Fig. 33-a shows a skyrmion in a vertical field which varies in the x direction. In addition to the background electric field a small extra E_z which linearly increases in x direction is added. This extra field makes the skyrmion move towards the area with smaller vertical field. Parts (b) and (c) show a skyrmion and a small field in x or y directions that increases linearly in x. In this case the skyrmion moves towards the area with bigger E_x or E_y.

The effects of nonuniform vertical and in-plane fields are different in terms of the way the skyrmions move. We can understand the difference by the following argument. The interaction energy between the horizontal region of the director, namely the blue part of the π-wall, and the external field is minimized when the director and the external field
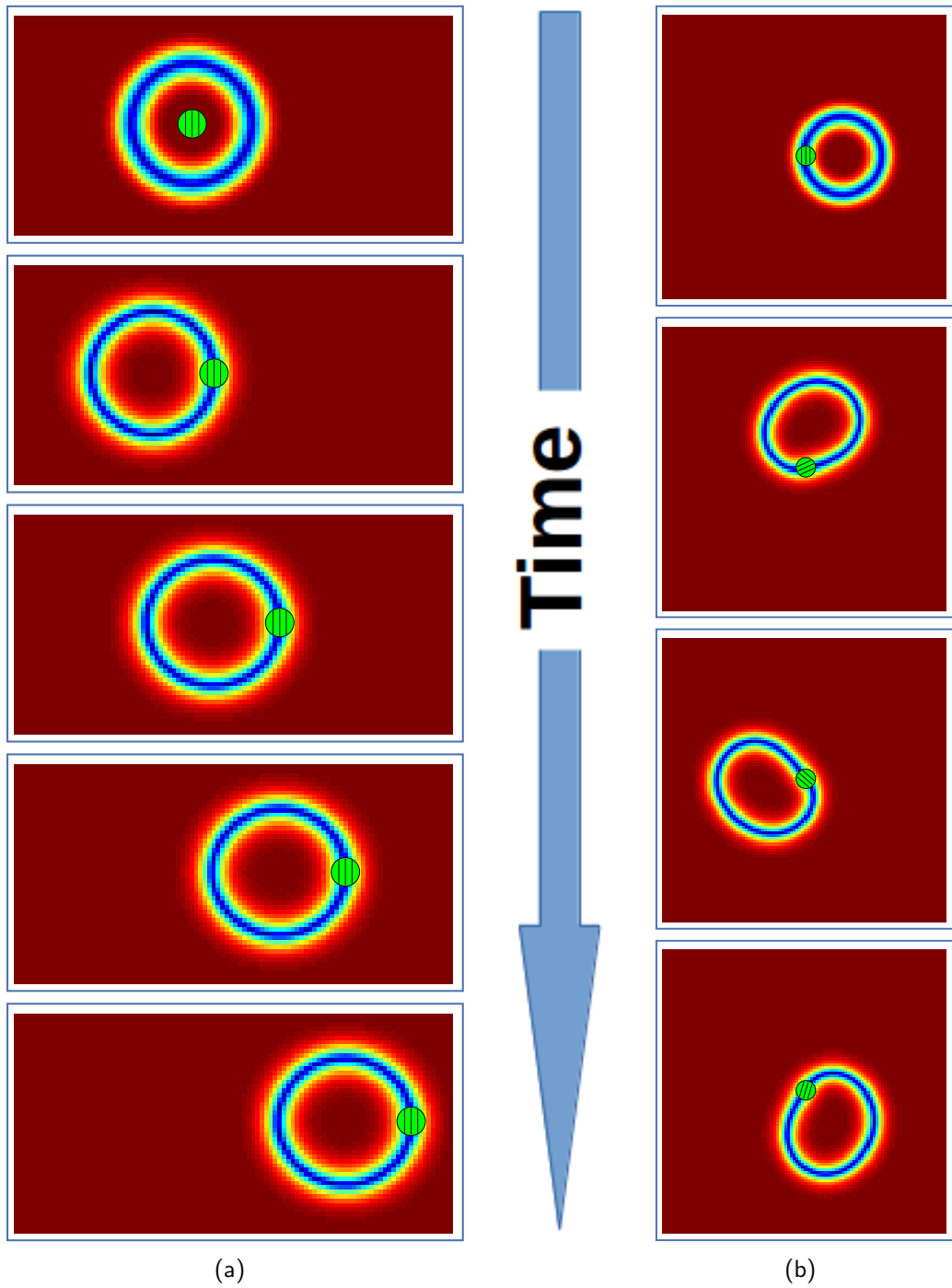
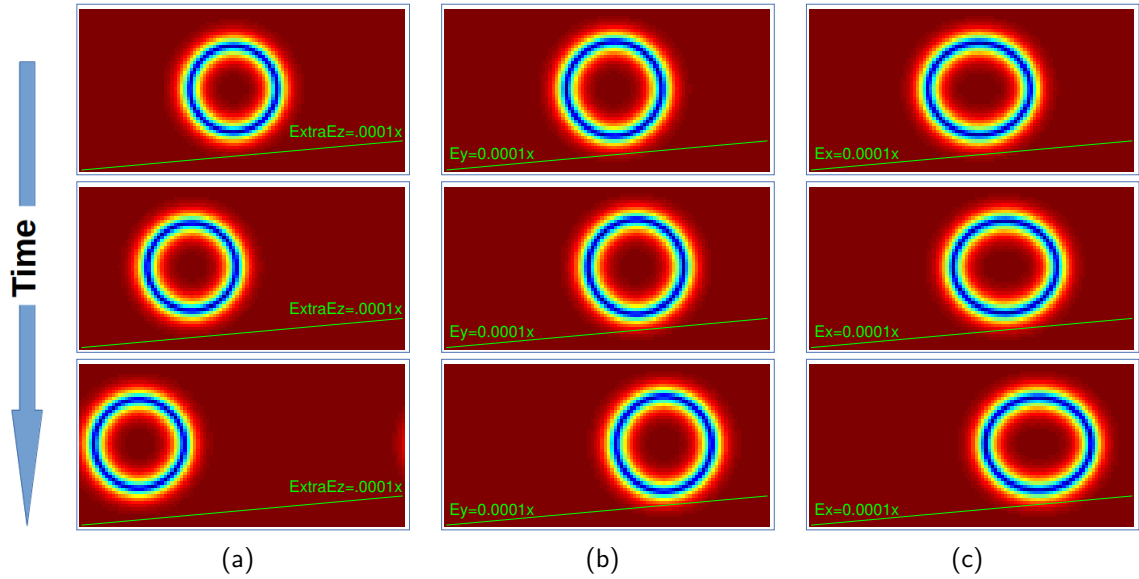**Figure 32:** Skyrmions (a) moved and (b) rotated by extra $E_\perp$

Figure 33: Skyrmions move towards (a) smaller E_z and (b,c) bigger $E_\perp$

are aligned. Thus, just like in the previous sections, the blue region attracted towards horizontal fields is repelled by vertical fields. In this case when there are field gradients, skyrmions move towards the area with smaller vertical field and bigger in-plane field.

We also note that addition of extra fields have different effects on skyrmion shape depending on the direction. Skyrmions moved into bigger in-plane field are slightly elongated in the field direction. On the contrary, being dragged into smaller E_z will cause the size of the skyrmion to grow *almost* isotropically in the $x - y$ plane. However note that this isotropy is not perfect due to the gradients of E_z in the horizontal plane.

5.4 3D Skyrmions

5.4.1 Electric field and negative anisotropy

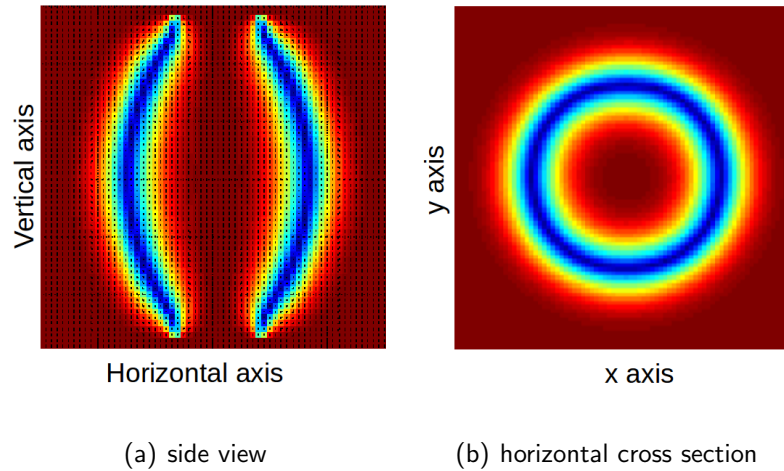(a) side view   (b) horizontal cross section

Figure 34: 3D skyrmion with negative anisotropy. Color shows z component of the director. (a) side view, (b) cross section of mid-plane.

We can realize 3D skyrmions in a cell with homeotropic surface anchoring. Figure 34 shows the side view and mid-plane cross-section of such a static skyrmion between two surfaces. The shape can be cylindrical with straight side walls (not shown here) or in the shape of a *barrel* where the radius narrows down at the top and bottom. In 3D, the dielectric anisotropy can also be negative when the vertical alignment is sustained by the homeotropic surface anchoring. With negative anisotropy, we show by simulations that the interaction and the driving effect of electric fields is of opposite nature. This effect is due to the same mechanisms explained in the previous sections so we don't repeat them here. While extra vertical fields push the skyrmions with positive anisotropy, they pull the ones with negative anisotropy. The same applies for in-plane fields. In-plane fields pull the skyrmions with positive anisotropy and push the ones with negative anisotropy (see
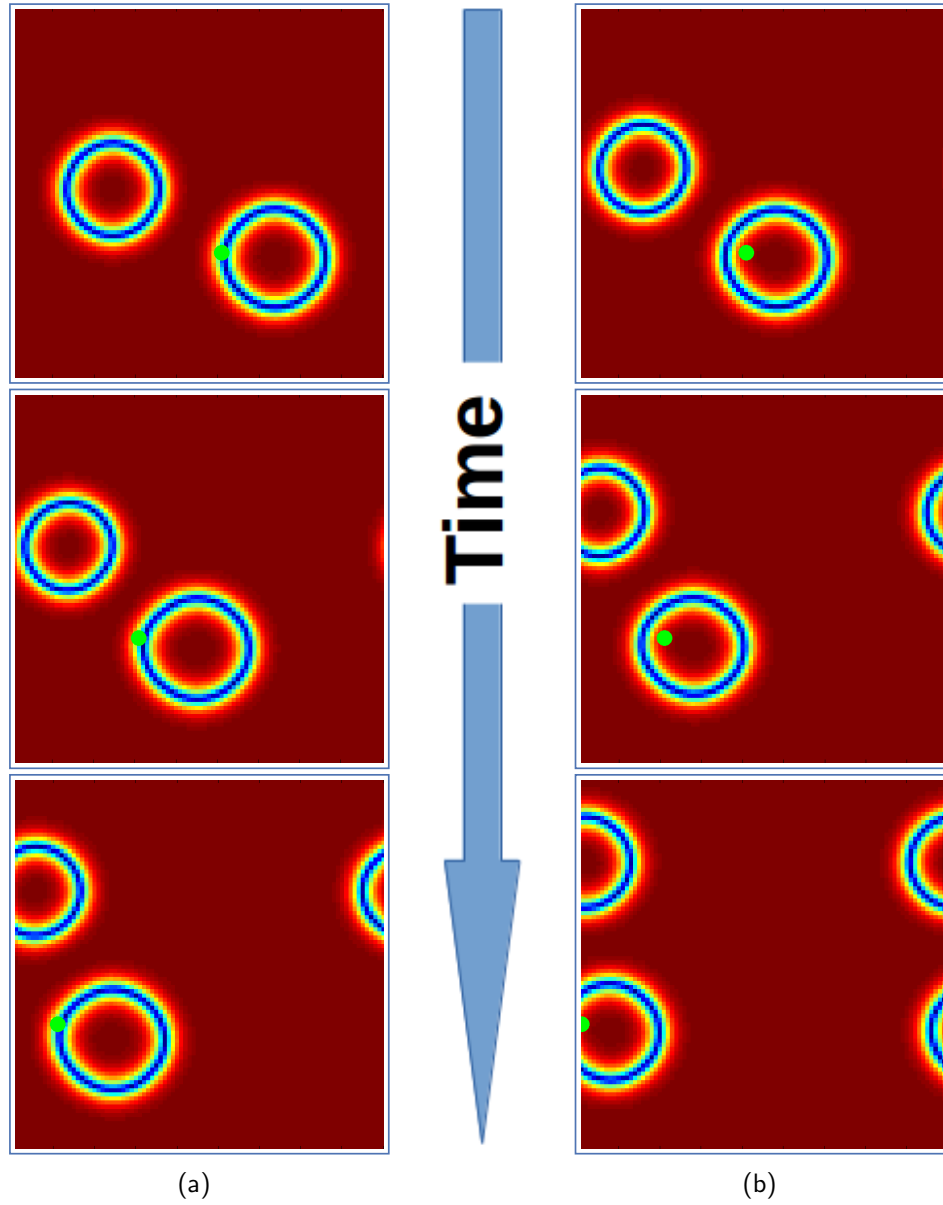
Figure 35: Horizontal mid-plane of a 3D skyrmion with negative anisotropy. As opposed to 2D skyrmions with positive anisotropy, blue region is (a) pulled by extra E_z, (b) pushed by extra $E_\perp$.
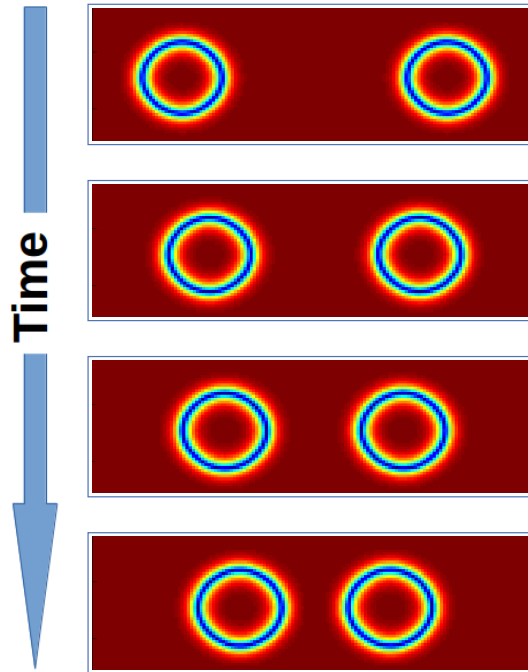
Figure 36: 3D Skyrmions move towards region with weaker surface anchoring

Fig. 35).

5.4.2 Effect of Nonuniform Surface Anchoring

Figure 36 shows two skyrmions that are stabilized by surface anchoring. The dielectric anisotropy is negative which favors easy-plane alignment. The strength of the nonuniform surface anchoring varies sligthly as a parabolic function whose minimum is at the center. The effect of this arrangement is similar to a nonuniform vertical field. We see here also that the π-wall is pushed away from regons with stronger vertical alignment. The skyrmions move towards the region with smaller surface anchoring and stop at a separation due to repulsion between the skyrmions.

Surface anchoring can be designed in custom ways thus it can allow various possibilities for applications together with nonuniform fields.
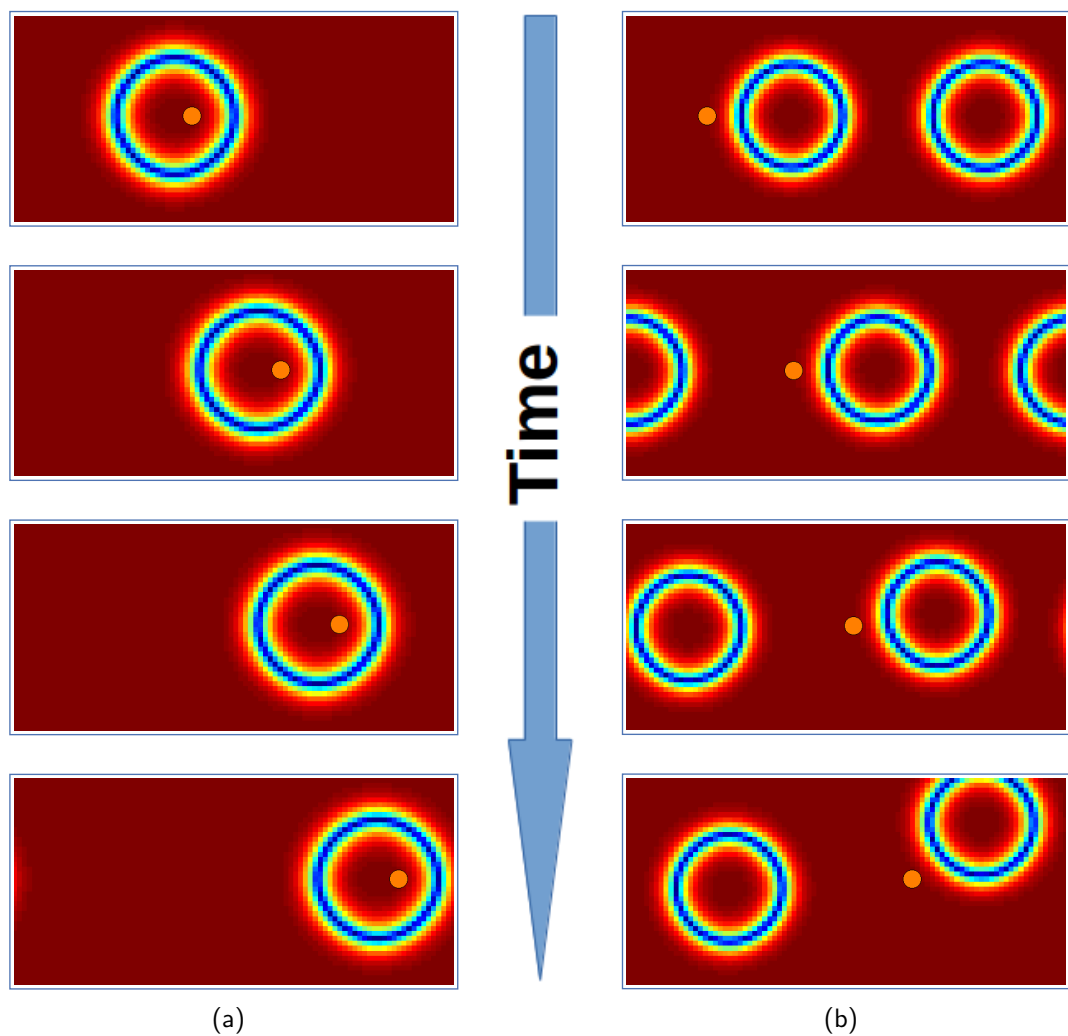
Figure 37: Light repels skyrmions with (a) negative(3D) or (b) positive(2D) anisotropy.

5.5 Actuation by Light

5.5.1 Skyrmions are repelled by light

It's shown experimentally that when exposed to light, skyrmions move toward the darker regions [3]. This might be attributed to the flow of heat generated by light and the resulting bias in the Brownian motion of the molecules. However we also know that light changes the cholesteric pitch in some liquid crystals. To model this efefct we reduce

the chirality, q_0 in the free energy by 20% where the light falls.

Figure 37 shows a skyrmion and a spot with light. Similarly to the electric field, the orange spot pushes away the π-wall. One difference from electric fields is that light pushes skyrmions regardles of the sign of the anisotropy. In part (a) of the figure we see the cross-section of a 3D skyrmion with negative anisotropy while in part (b) a 2D skyrmion and another skyrmion pushed by the skyrmion is shown.

To understand this behavior we consider the balance between intermolecular interactions which favor a twist and the vertical field (plus surface anchoring in 3D) which favors vertical alignment. As the orange spot enters the skymrmion, it will cause the molecular interaction favoring twist to be weaker and change the balance in favor of vertically aligninment. A shift towards more vertical alignment will cause the skyrmion to translate away from the light.

The effect of light turns out to be the same as extra E_z for positive anisotropy thus it can be employed in the same way as electric fields to confine or guide skyrmions. Depending on the exprimental setup one method can be advantageous over the other.

5.6   Skyrmions under Pressure

5.6.1   Between Walls: Trash Compactor

We have seen that skyrmions repel other nearby skyrmions in a fashion very similar to particles. What if we push skyrmions together under pressure? Would they merge and form one skyrmion, keep their shapes, or deform? To answer this question we put two skyrmions in a box whose walls are blocks of light. Inside the walls the natural twist q_0 is reduced by 20%. It was shown in the previous section that the region with reduced

chirality acts like a wall that repels skyrmions.

In Fig. 38, we show snapshots from such a simulation where one of the walls moves and squeezes the skyrmions like a *trash compactor*. First the skyrmions get smaller and also closer to each other. As we increase the pressure we first see that one skyrmion slips due to the repulsion between skyrmions and the skyrmions fill the box diagonally. Then the skyrmion near the moving wall gets smaller but stays in circular shape. As we press further that skyrmion *pops*. Due to the extra space generated, the remaining skyrmions expands. Later on it also shrinks under pressure and finally disappears. This simulation demonstrates several aspects of the particle like behavior of a system of skyrmions. Skymrions:

- interact with other skyrmions

- go through elastic deformations change size when under pressure

- stay in robust circular shape for the simulated parameters

- pop and disappear under high pressure

- do not merge but pop when pushed together

5.6.2 Popping a skyrmion

In order to view what happens as a skyrmion under pressure pops, we save snapshots with smaller time intervals. The slow motion movie reveals the nature of the *crack propagation* when a hole is poked in the π-wall. Snapshots of such an event is shown in Fig. 39. When two walls move towards each other the skyrmions first contract and get smaller in size. Then a hole emerges on one of the skyrmions and grows around the blue
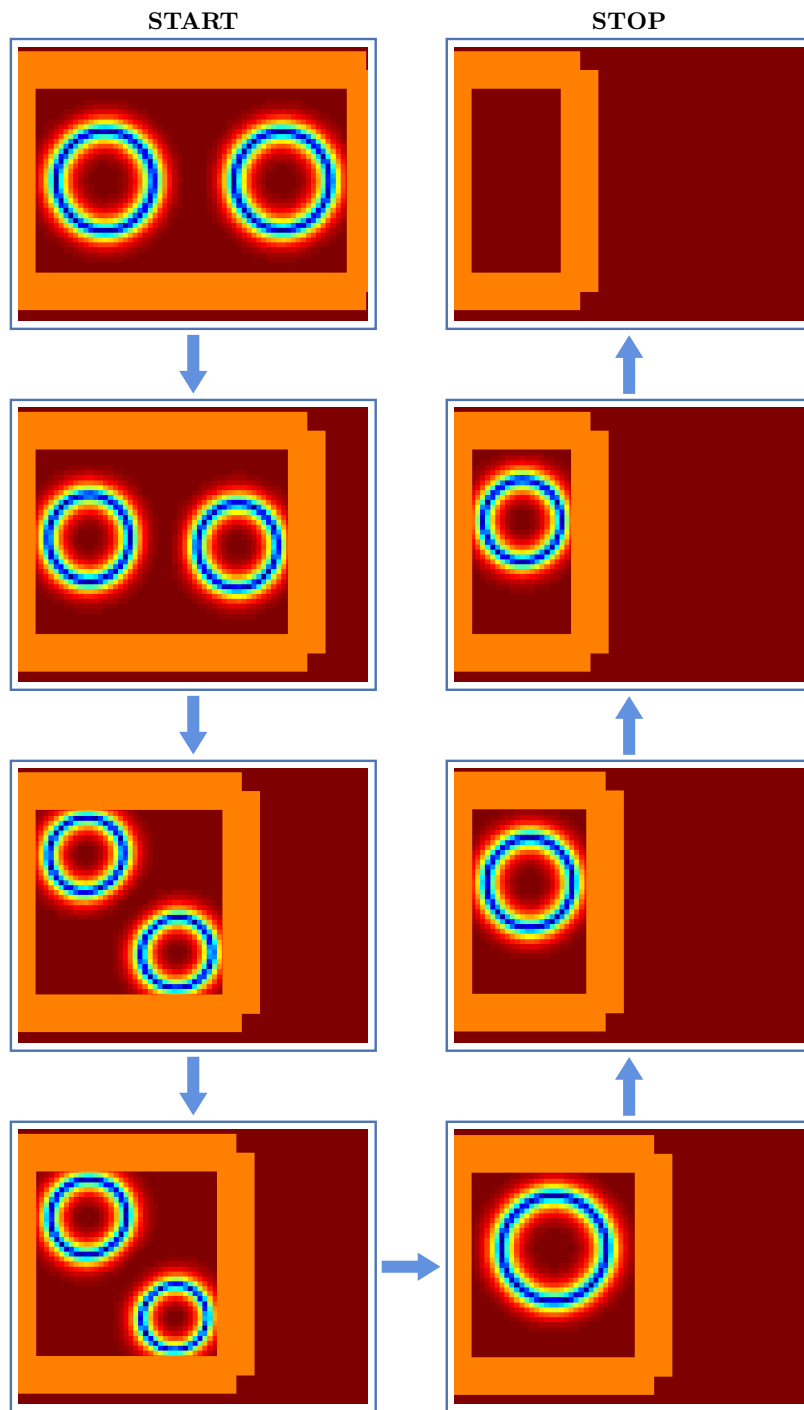
Figure 38: Skyrmions between compacting walls.

circle. Soon, it is followed by the popping of the other skyrmion. Eventually they both disappear and all we have left is the vertical nematic background.

This simulation illustrates interesting features of the motion of disclination lines. The hole is equivalent to a pair of half-charge disclinations, one at each end of the π-wall. The process of the hole growing is equivalent to the disclinations moving around the π-wall and then annihilating each other. Further research, both analytical and computational, can potentially lead to better understanding of related phenomena.
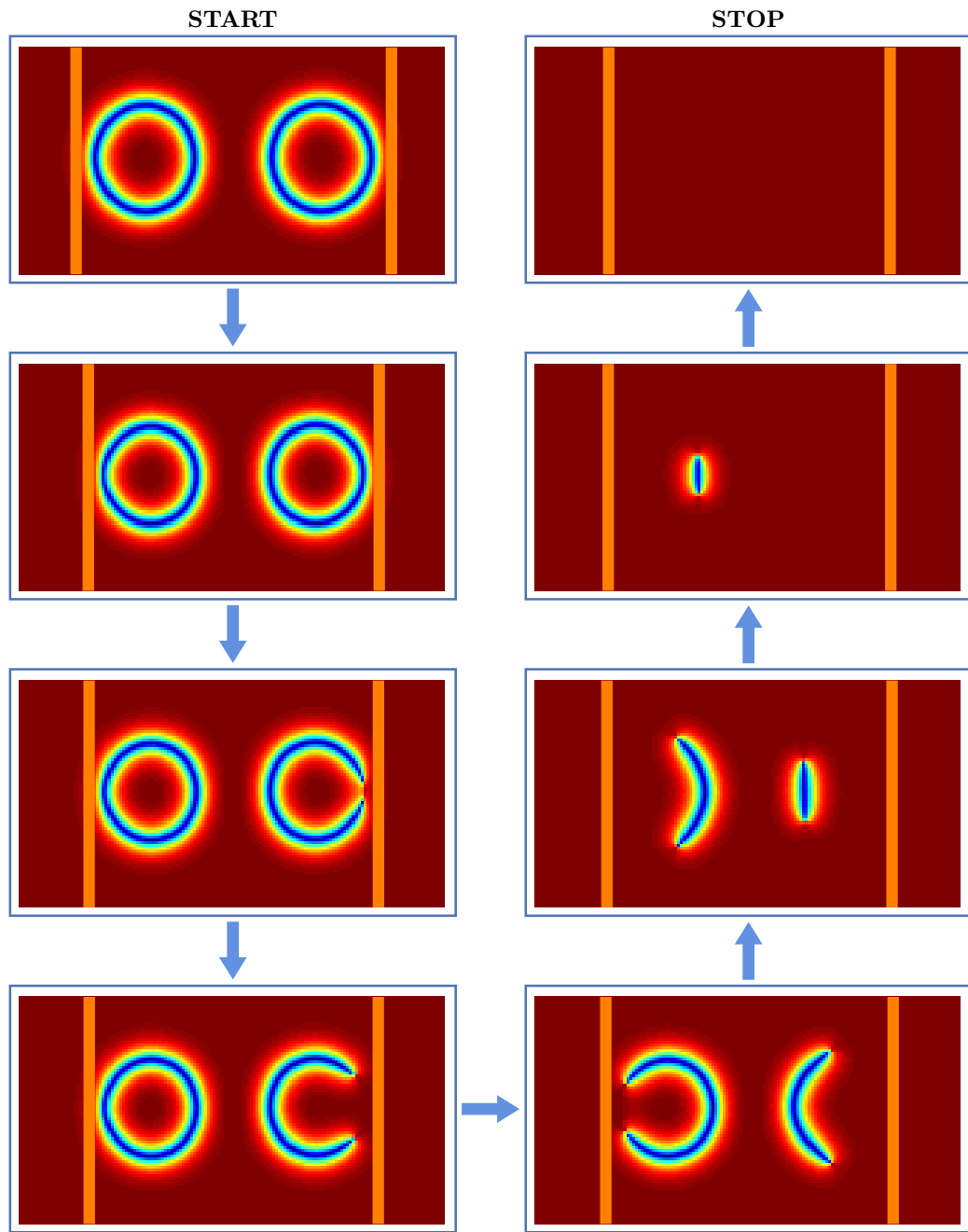
Figure 39: Slow motion view of popping skyrmions squeezed between walls

BIBLIOGRAPHY

[1] S.-Z. Lin, C. Reichhardt, C. D. Batista, and A. Saxena, "Particle model for skyrmions in metallic chiral magnets: Dynamics, pinning, and creep," *Phys. Rev. B*, vol. 87, p. 214419, Jun 2013.

[2] N. Nagaosa and Y. Tokura, "Topological properties and dynamics of magnetic skyrmions," *Nat. Nanotechnol.*, vol. 8, pp. 899–911, 2013.

[3] H. Sohn, P. Ackerman, and I. I. Smalyukh, "Optical patterning and dynamics of torons and hopfions in a chiral nematic with photo-tunable equilibrium pitch," *Aps March Meeting*, vol. 62, Mar 2017.

[4] P. J. Ackerman, T. Boyle, and I. I. Smalyukh, "Squirming motion of baby skyrmions in nematic fluids," *Nature Communications*, vol. 8, p. 673, Sep 2017.

[5] H. R. O. Sohn, P. J. Ackerman, T. J. Boyle, G. H. Sheetah, B. Fornberg, and I. I. Smalyukh, "Collective behavior of active topological solitons, knotted streamlines, and transport of cargo in liquid crystals," Nov 2017.

CHAPTER 6

Conclusions

6.1   Summary

We studied orientational order and how nonuniform configurations are formed by the interplay of molecular interactions, geometry, external fields, and dynamics.

In the first project, we investigated polydomain formation during the manufacturing of liquid crystal elastomers which are often attributed to quenched disorder. As an alternative explanation, we developed a theory for the dynamics of the isotropic-nematic transition, and showed that the dynamics can induce a polydomain structure with a characteristic length scale. This polydomain state may eventually become uniform, or it may be locked in by impurities.

In the second project, we performed approximate analytical calculations regarding orientational order and density profiles near flat or curved walls. We then, ran Langevin dynamics simulations to compare the results. Even when the particles do not interact, the walls can still induce (nonuniform) order. We employed these properties for rectification of active particles, and actuation of passive particles such as curved tracers or filaments in an active bath.

In the third project, we investigated topological defects such as skyrmions in liquid crystals in which the order is controlled by chiral molecular interactions, external fields, and surface anchoring. We obtained phase diagrams for chiral nematic liquid crystals and

contrasted them with magnetic counterparts. Our work indicates that while skyrmions are favored by polar interactions and easy-axis alingment, merons are favored by nematic interactions and easy-plane alignment. In addition, we realized dynamically stabilized liquid crystal skyrmions in simulations and performed analytical calculations to predict the suitable range of parameters. We also demonstrated that light, field gradients, and surface anchoring can be used to move skyrmions.

6.2 Future work

The work presented in this dissertation can be moved forward in various directions. Liquid crytal elastomer model can be modified by inclusion of time dependent coupling strength and built-in reference states (again time dependent) for the nematic order tensor as the cross-linking process continues. Effects of strain and fields can also be added to the picture.

Our results from the active matter part can be used to study flexible membranes and filaments in interaction with active particles. This could include static passive particles as well as moving ones where one would need to solve the equations with moving boundaries. Collective behavior of interacting particles could have interesting results different from non-interactiong systems we studied here.

Study of chiral nematic liquid crystals in the context of skyrmions are relatively new and have great potential to become a major field of research. We have demonstared numerical tools to simulate large systems of liquid crystals which behave like particles. The detailed study of dynamics and flexibility of skyrmions and merons can be an immediate extension of our work. Also, the model can be improved by adding elasticity and flow.